Three-dimensional Statistical Shape Models for Multimodal Cardiac Image Analysis

Currently, the field of cardiovascular imaging is constituted by different modalities. Each modality exploits distinct physical phenomena, which allows us to observe the cardiac organ from different angles. Clinicians collect all these pieces of information to form an integrated mental model. The mental model includes anatomical and functional information to display a full picture of the patient's heart. It is highly desirable to transform this mental model into a computational model able to integrate the information in a comprehensive manner. Generating such a model is not simply a visualization challenge. It requires having a methodology able to extract relevant quantitative parameters by applying the same principle. This assures that the measurements are directly comparable. Such a methodology should be able to: 1) accurately segment the cardiac cavities from multimodal datasets, 2) provide a unified frame of reference to integrate multiple information sources, and 3) aid the classification of a patient's cardiac condition. This thesis builds upon the idea that statistical shape models are a robust and accurate approach with the potential to incorporate all these requirements.
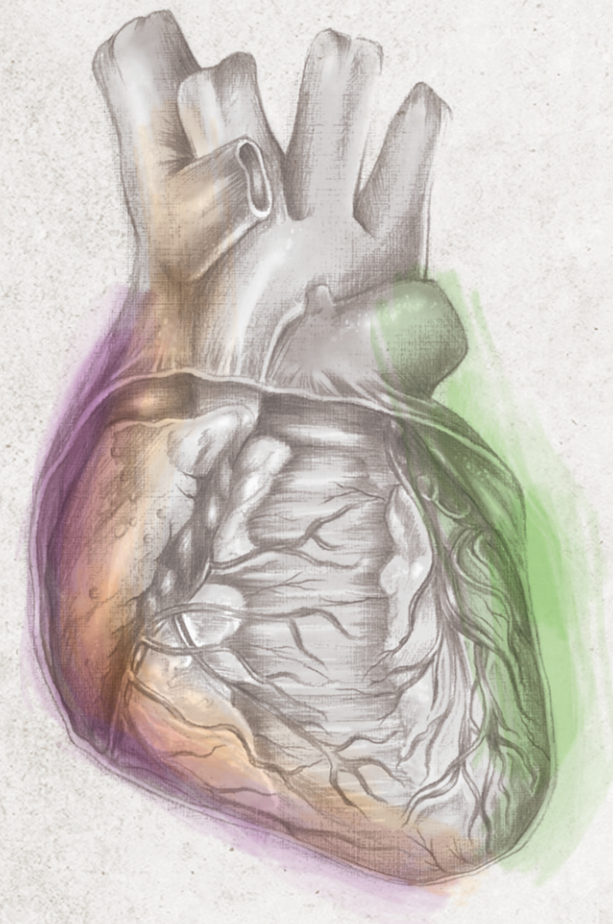
Catalina Tobón Gómez

Three-dimensional Statistical Shape Models for Multimodal Cardiac Image Analysis Catalina Tobón Gómez

Three-dimensional Statistical Shape Models for Multimodal Cardiac Image Analysis

Catalina Tobón Gómez

Tesi Doctoral UPF / 2011

UNIVERSITAT
POMPEU FABRA

Supervised by

Dr. Alejandro F. Frangi

Department of Information and Communication Technologies

Universitat Pompeu Fabra

About the cover

The pencil drawing of the heart shows the complexity of the organ. Clinicians view this complex organ through different imaging modalities. Each modality highlights different aspects of the heart. The art of their profession is to form a mental image that combines these aspects. In the drawing, the different modalities are expressed by differently colored brush strokes.
Cover design: d-mension studio s.a / Illustration: Julian Román / Medellín - Colombia.

To Arjan and his many questions

Contents

List of Figures

List of Tables

Nomenclature

χ^2	Chi-square dissimilarity metric
3DUS	Three dimensional Ultrasound
A	Peak atrial flow velocity
AHA	American Heart association
Ao	Aorta
ASM	Active Shape Model
ASPIRE	A sparse precomputed iterative reconstruction library
B&A	Bland-Altman plots
CABG	Coronary artery bypass grafting
CAD	Coronary arterial disease
CK-MB	Creatine kinase-MB
CO	Cardiac output
CRT	Cardiac Resynchronization Therapy
CT	Computed Tomography
CVD	Cardiovascular disease
DCM	Dilated cardiomyopathy
DT	Deceleration time early flow velocity
E	Peak early flow velocity
ECG	Electrocardiogram
ED	End of diastole
EDV	End diastolic volume
EF	Ejection fraction
ES	End of systole
ESV	End systolic volume
FBP	Filtered back-projection
FWHM	Full-Width-at-Half-Maximum
GR	Maximum gradient boundary model
gSPECT	Gated Single Photon Emission Computed Tomography
HCM	Hypertrophic cardiomyopathy
HF	Heart failure
HR	Heart rate
Hyp	Hypertrophy
Isch	Ischemic

IV	Inter-observer variability
IVC	Inferior Vena Cava
IVRT	Isovolumic relaxation time
KL	Kullback-Leibler divergence
LA	Long-axis
LAt	Left atrium
LBBB	Left Bundle Branch Block
LGE	Late gadolinium enhancement
LV	Left ventricle/left ventricular
MCAT	Mathematical cardiac-torso phantom
MRI	Magnetic Resonance Imaging
MRISIM	Simulator for Magnetic Resonance Imaging
MSD	Mean signed difference
NCAT	4-D NURBS-based cardiac-torso phantom
NRL	No reliability
NSTEMI	Non-ST elevation myocardial infarction
OSEM	Ordered-subset expectation maximization
P2S	Unsigned point-to-surface errors
PA	Pulmonary artery
PCA	Principal Component Analysis
PCI	Percutaneous catheterization
PDM	Point Distribution Model
PFR	Peak filling rate
PVs	Pulmonary veins
QGS	Quantitative gSPECT algorithm
RAt	Right atrium
RF	Regurgitation fraction
RL	With reliability
ROI	Region of interest
RV	Right ventricle/right ventricular
SA	Short-axis
SD	Standard deviation
SIMIND	Monte Carlo simulation code
SPASM	Segmentation of sparse and arbitrarily oriented cardiac MRI data
SPECT	Single Photon Emission Computed Tomography
SSFP	Steady State Free Precession
ST	Step function boundary model
STEMI	ST elevation myocardial infarction
SV	Stroke volume
SVC	Superior Vena Cava
TIR	Triple inversion recovery
TOF	Tetralogy of Fallot
TTPF	Time to peak filling
US	Ultrasound
VM	Ventricular mass
VTC	Volume time curve
WH	Whole heart
XCAT	4-D extended cardiac-torso phantom

Abstract

Cardiovascular diseases (CVDs) are the major cause of death in the Western world. The desire to prevent and treat CVDs has triggered a rapid development of medical imaging systems. As a consequence, the amount of imaging data collected in health care institutions has increased considerably. This fact has raised the need for automated analysis tools to support diagnosis with reliable and reproducible image interpretation. The interpretation task requires to translate raw imaging data into quantitative parameters, which are considered relevant to classify the patient's cardiac condition. To achieve this task, statistical shape model approaches have found favoritism given the 3D (or 3D+t) nature of cardiovascular imaging datasets. By deforming the statistical shape model to image data from a patient, the heart can be analyzed in a more holistic way.

Currently, the field of cardiovascular imaging is constituted by different modalities. Each modality exploits distinct physical phenomena, which allows us to observe the cardiac organ from different angles. Clinicians collect all these pieces of information to form an integrated mental model. The mental model includes anatomical and functional information to display a full picture of the patient's heart. It is highly desirable to transform this mental model into a computational model able to integrate the information in a comprehensive manner. Generating such a model is not simply a visualization challenge. It requires having a methodology able to extract relevant quantitative parameters by applying the same principle. This assures that the measurements are directly comparable. Such a methodology should be able to: *1)* accurately segment the cardiac cavities from multimodal datasets, *2)* provide a unified frame of reference to integrate multiple information sources, and *3)* aid the classification of a patient's cardiac condition.

This thesis builds upon the idea that statistical shape models, in particular Active Shape Models, are a robust and accurate approach with the potential to incorporate all these requirements. In order to handle multiple image modalities, we separate the statistical shape information from the appearance information. We obtain the statistical shape information from a high resolution modality and include the appearance information by simulating the physics of acquisition of other modalities.

The contributions of this thesis can be summarized as: *1)* a generic method to automatically construct intensity models for Active Shape Models based on simulating the physics of acquisition of the given imaging modality, *2)* the first extension of a Magnetic Resonance Imaging (MRI) simulator tailored to produce realistic cardiac images, and *3)* a novel automatic intensity model and reliability training strategy applied to cardiac MRI studies. Each of these contributions represents an article published or submitted to a peer-review archival journal.

Resumen

Las enfermedades cardiovasculares (ECVs) son la principal causa de mortalidad en el mundo Occidental. El interés de prevenir y tratar las ECVs ha desencadenado un rápido desarrollo de los sistemas de adquisición de imágenes médicas. Por este motivo, la cantidad de datos de imagen recolectados en las instituciones de salud se ha incrementado considerablemente. Este hecho ha aumentado la necesidad de herramientas automatizadas para dar soporte al diagnóstico, mediante una interpretación de imagen confiable y reproducible. La tarea de interpretación requiere traducir los datos crudos de imagen en parámetros cuantitativos, los cuales son considerados relevantes para clasificar la condición cardiaca de un paciente. Para realizar tal tarea, los métodos basados en modelos estadísticos de forma han recibido favoritismo dada la naturaleza tridimensional (o 3D+t) de las imágenes cardiovasculares. Deformando el modelo estadístico de forma a la imagen de un paciente, el corazón puede analizarse de manera integral.

Actualmente, el campo de las imágenes cardiovasculares esta constituido por diferentes modalidades. Cada modalidad explota diferentes fenómenos físicos, lo cual nos permite observar el órgano cardiaco desde diferentes ángulos. El personal clínico recopila todas estas piezas de información y las ensambla mentalmente en un modelo integral. Este modelo integral incluye información anatómica y funcional que muestra un cuadro completo del corazón del paciente. Es de alto interés transformar este modelo mental en un modelo computacional capaz de integrar la información de manera global. La generación de un modelo como tal no es simplemente un reto de visualización. Requiere una metodología capaz de extraer los parámetros cuantitativos relevantes basados en los mismos principios técnicos. Esto nos asegura que las mediciones se pueden comparar directamente. Tal metodología debe ser capaz de: *1)* segmentar con precisión las cavidades cardiacas a partir de datos multimodales, *2)* proporcionar un marco de referencia único para integrar múltiples fuentes de información, y *3)* asistir la clasificación de la condición cardiaca del paciente.

Esta tesis se basa en que los modelos estadísticos de forma, y en particular los Modelos Activos de Forma, son un método robusto y preciso con el potencial de incluir todos estos requerimientos. Para procesar múltiples modalidades de imagen, separamos la información estadística de forma de la información de apariencia. Obtenemos la información estadística de forma a partir de una modalidad de alta resolución y aprendemos la apariencia simulando la física de adquisición de otras modalidades.

Las contribuciones de esta tesis pueden ser resumidas así: *1)* un método genérico para construir automáticamente modelos de intensidad para los Modelos Activos de Forma simulando la física de adquisición de la modalidad en cuestión, *2)* la primera extensión de un simulador de Resonancia Magnética Nuclear diseñado para producir estudios cardiacos realistas, y *3)* un método novedoso para el entrenamiento automático

de modelos de intensidad y de fiabilidad aplicado a estudios cardiacos de Resonancia Magnética Nuclear. Cada una de estas contribuciones representa un artículo publicado o enviado a una revista técnica internacional.

Chest pain, shortness of breath. The patient may have a cardiac condition. And so the imaging journey begins. The first Ultrasound study makes its appearance, giving a general evaluation of heart performance. If abnormalities are found, a cardiac Magnetic Resonance Imaging study can provide a more complete picture. If ischemia is suspected, a Nuclear Medicine study would be the right choice, or perhaps a Computed Tomography scan to search for coronary stenosis.

As the patient dances from acquisition to acquisition, the amount of data collected increases enormously. Ultimately, raw imaging data has to be translated into interpretable parameters. Each pathology can be described as a combination of those parameters. The clinician in charge will mentally combine all the information to diagnose the patient and finally decide the appropriate treatment.

1

General Introduction

1.1   Context

1.1.1   Cardiac Function

The pumping action of the cardiac organ is caused by a fascinating chain of events. A healthy heart will unfold each of these events at specific moments to obtain a choreographed ejecting contraction and filling relaxation. As the heart deteriorates, due to aging or disease, its performance becomes inefficient.

Heart performance, i.e. *cardiac function*, is usually divided into two groups: systolic and diastolic. Systolic function refers to events occurring during contraction and ejection. Diastolic function refers to events occurring during relaxation and filling. Different quantitative parameters have been suggested to evaluate each of them at global and regional level.

Global systolic function can be measured for both ventricles and is based on ventricular volumes at end diastole (EDV) and end systole (ESV). From these volumes other parameters are calculated, as summarized in Table 1.1. Ventricular mass (VM) is also a global indicator of cardiac function. VM is calculated based on the volume contained within the epicardial borders, mi-
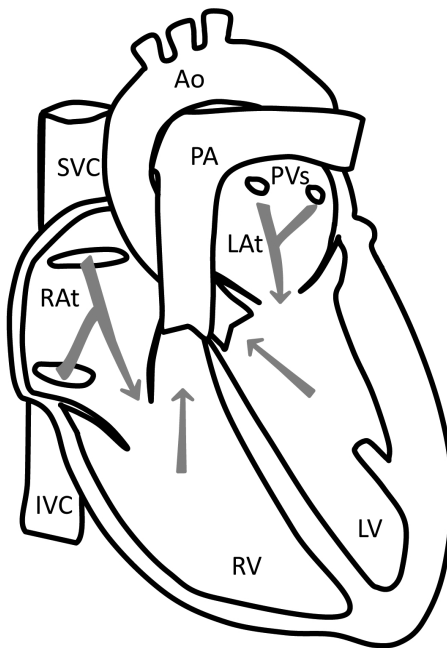
Figure 1.1: *Schematic diagram of cardiac function. Venous blood arrives from the Superior Vena Cava (SVC) and Inferior Vena Cava (IVC) to the Right Atrium (RAt). From the RA, blood passes to the Right Ventricle (RV). The RV sends the blood via the Pulmonary Artery (PA) to be oxygenated in the lungs. Oxygenated blood comes back to the Left Atrium (LAt) via Pulmonary Veins (PVs) and passes to the Left Ventricle (LV). Finally, the LV ejects the blood through the Aorta (Ao) to the peripheral circulatory system.*

TABLE 1.1: Systolic function parameters derived from volume measurements

Parameter	Acronym	Calculation	Units
Stroke Volume	SV	$EDV - ESV$	ml
Ejection Fraction	EF	$\frac{EDV-ESV}{EDV} \times 100$	%
Cardiac Output	CO	$HR \times SV$	ml/min
Mass	VM	$(EDV_{epi} - EDV) \times 1.05$	g

EDV= End diastolic volume; ESV= End systolic volume;

HR= Heart rate; EDV_{epi}= Epicardial EDV.

nus the chamber volume, multiplied by the density of the muscle tissue (see Table 1.1). A better evaluation of systolic performance can be achieved by evaluating regional function. Main regional parameters include wall thickness and wall thickening [1]. More recently, myocardial strain[1] can be evaluated along the radial, circumferential and longitudinal directions [2].

Diastolic function is currently evaluated based on flow and tissue velocity curves. These curves show the filling dynamics of the LV and yield the following parameters: isovolumic relaxation time (IVRT), peak early (E) and peak atrial (A) flow velocity, and, deceleration time (DT) of early flow velocity [3]. Some studies have indirectly measured diastolic function parameters from volume time curves (VTC) [4,5]. The diastolic behavior of the LV is evaluated from the filling rate curve, calculated as the first derivative of the VTC. The two most exploited parameters obtained from this curve are: peak filling rate (PFR) and time to peak filling (TTPF). PFR is estimated as the maximum value of this curve, divided by EDV as a normalizing factor. TTPF corresponds to the time elapsed between end systole and PFR (see Fig. 1.2) [4].

Valvular function can have an impact on both systole and diastole. If the valves fail to open or close properly, the ejection and filling processes, and hence cardiac function, will be impaired. Valvular function is evaluated as the degree of valvular stenosis and/or regurgitation fraction (RF)[2] [6].

1.1.2   Cardiovascular Imaging

This section briefly reviews the imaging techniques most frequently used for cardiac function analysis. Some functional parameters can be evaluated with multiple modalities (see Fig. 1.3). In this case, the decision to use one modality or another is given by a combination of cost-effectiveness and non-ionization requirements.

---

[1]Relative deformation of tissue from an applied force.
[2]Percentage of blood that backflows to the previous cavity.
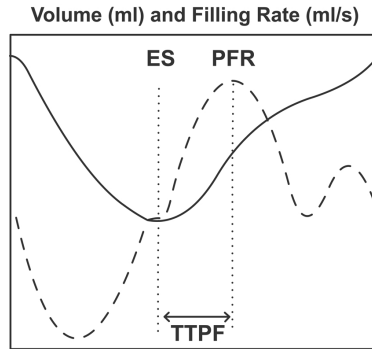
Figure 1.2: *Methodological outline of the volume (−) and filling rate (− −) curves: definition of time to peak filling (TTPF) as the time elapsed between time of end systole (ES) and time of peak filling rate (PFR).*

Angiography

Angiography is an imaging technique based on X-ray principles. A 2D projection of the heart is obtained after injecting a radio-opaque contrast. The strength of this modality is the visualization of coronary stenosis, while its weakness is poor soft tissue contrast. Angiography is the modality used for interventional procedures and it involves catheterization of the patient. The catheter allows the interventional radiologist to reach the coronaries in a minimally invasive way. Catheterization can be used for stent deployment, myocardial ablation or electrophysiological studies[3], among others (see 1.2.2) [7].

Ultrasound (US)

Cardiac ultrasound or echocardiography is the fastest, least expensive, and least invasive screening modality to image the heart. The strength of this modality is its high temporal resolution, ideal for wall motion assessment. Using color Doppler and tissue Doppler imaging, intracavitary flow and wall tissue velocities can be measured as well. The acquisition can be performed in 2D, for high temporal resolution, or in 3D, for volumetric information. As a down side, the acoustic window of some patients may not alow for high quality image acquisition. In such cases, a transesophageal echocardiography study can be performed [8].

Single Photon Emission Computed Tomography (SPECT)

Nuclear medicine is the classical modality to evaluate myocardial perfusion to determine infarcted and/or underperfused areas. In order to obtain a SPECT dataset, a radiopharmaceutical is administered to the patient. This radiopharmaceutical emits gamma rays, which are detected by the imaging device. SPECT images can be gated with the patient's electrocardiogram such that perfusion

---

[3]Measuring the action potentials of the myocardium.

3DUS	*CT*	*SPECT*	*MRI*
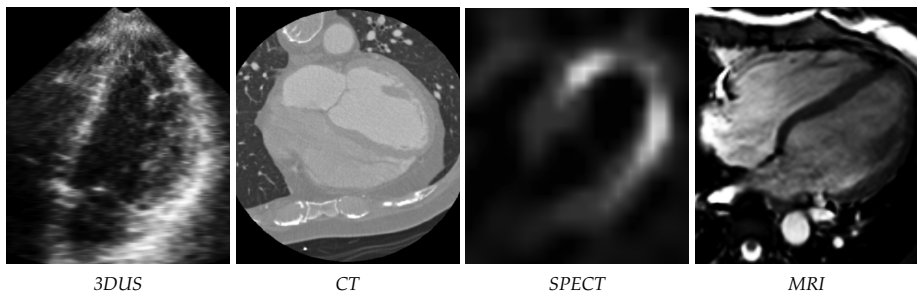
Figure 1.3: *Images from different modalities: 3DUS= Three-dimensional ultrasound; CT= Computed Tomography; MRI= Magnetic Resonance Imaging; SPECT= Single Photon Emission Computed Tomography.*

and left ventricular function can be evaluated simultaneously. The strength of this modality is that it directly assesses viability, while its weakness is the low spatial and temporal resolution of the datasets. The recent commercial availability of SPECT/CT hybrid systems provide attenuation correction for reconstruction techniques improving considerably the quality of the images [9].

Computed Tomography (CT)

This modality presents high resolution of over-all anatomical information providing excellent imaging of the heart and coronary arteries. Also, it is relatively inexpensive and provides fast acquisitions. However, it is based on physical principles (X-ray) that expose patients to high doses of radiation. Recent studies have employed delayed enhancement CT imaging to quantify myocardial infarct size and transmurality [9, 10].

Magnetic Resonance Imaging (MRI)

MRI has become the gold standard of accuracy and reproducibility for assessment of volumes, mass, and wall motion [8]. It allows easy differentiation of soft tissues and blood without any contrast agent. The limitations of this modality include: long acquisition time, claustrophobic sensations, and contraindications for patients with implanted pacemakers. Different sequences, perhaps in combination with contrast media, result on different types of images: an anatomical image highlights the soft tissues, a late gadolinium enhancement image highlights the necrotic/fibrotic tissue, an oedema image highlights accumulation of water (see Fig. 1.4). Recent developments allow to acquire 3D isotropic datasets for anatomical evaluation [11], 3D tagging datasets for strain analysis [12], 4D phase contrast imaging for flow measurements [13, 14], tissue phase mapping for myocardial motion analysis [15] and *in-vivo*[4] diffusion tensor imaging for cardiac fiber orientation visualization [16].

---

[4]Measurements performed in a living organism, as opposed to in a dead organism (*in-vitro*).

bSSFP   LGE   TIR
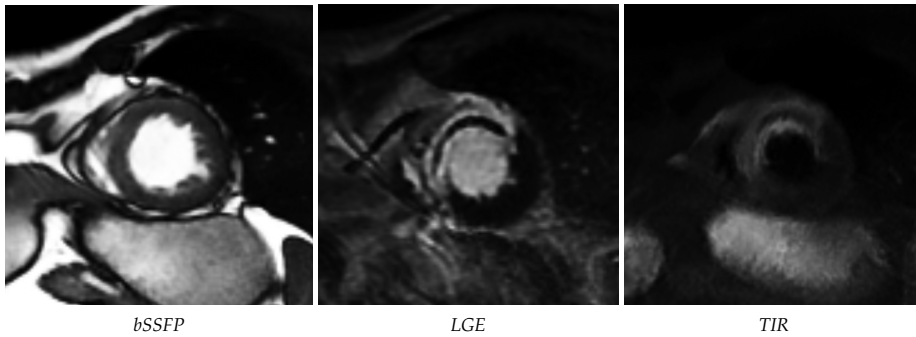
Figure 1.4: *MRI images for the same patient with three different sequences: balanced Steady State Free Precession (SSFP) sequence for anatomical evaluation, late gadolinium enhancement (LGE) sequence for necrotic/fibrotic tissue evaluation and triple inversion recovery sequence (TIR) for oedema evaluation.*

1.2   Clinical Motivation

1.2.1   Cardiovascular Diseases

Heart performance can easily be affected by dysfunctions. Dysfunctions initiate a cascade that latter on develops into a cardiovascular disease (CVD). CVDs are the major cause of death in the Western world claiming more lives each year than cancer and accidents combined [17, 18]. It is estimated that 36% of the adult population in the USA has a CVD [17]. In Europe, the older population has a 50% prevalence of CVDs causing about 40% of deaths. Let us briefly review the main ones:

Ischemic Cardiomyopathy

The cardiac muscle cell, like any other cell, depends on oxygen supply to function. Oxygen is provided by the blood. The blood is channeled through the coronary arteries. A reduction of blood supply to the cardiac muscle causes ischemia. An ischemic event is frequently caused by atherosclerosis[5] in the coronary arteries. This is known as coronary arterial disease (CAD). Atherosclerosis can cause occlusion of the coronary vessels, disrupting the blood supply to the myocardium. A prolonged ischemia can cause irreversible damage to the myocardial tissue [19]. This is known as myocardial infarction.

A myocardial infarction can cause abnormal loading conditions in the myocardium. In time, these abnormalities can induce shape alterations of the heart, such as localized thinning of the wall, and in extreme cases might generate a ventricular aneurysm. Other main shape alteration is ventricular dilation, and it is known as ischemic dilated cardiomyopathy. Ultimately, these abnormalities will impair the ejection capabilities of the heart.

---

[5]Accumulation of plaque on the wall of the vessels, which decreases the diameter of the vessel.

Non-ischemic Cardiomyopathies

A relatively recent classification of cardiomyopathies divides them into: *genetic*, *mixed* and *acquired* [20]. The most frequent genetic cardiomyopathy is hypertrophic cardiomyopathy (HCM). HCM is mainly characterized by thickening of the myocardial wall (hypertrophy). Although hypertrophy may appear as a physiological response to hypertension or aortic stenosis, the genetic alterations causing HCM increase the size of the myocardial cells severely. HCM is the most common cause of sudden cardiac death in young people, including athletes. In some cases of HCM, the myocardium can obstruct the out-flow of blood, disrupting the normal functionally of the heart [21].

The most frequent mixed cardiomyopathy is dilated cardiomyopathy (DCM). It may be caused by infectious agents, toxins, autoimmune and systemic disorders, as well as genetic alterations [20]. DCM is mainly characterized by dilation of the left ventricle, or even both ventricles, and impaired contractility. Contractility impairment translates into severe systolic dysfunction[6] [22].

The main acquired cardiomyopathy is myocarditis. Myocarditis is an inflammatory process affecting the myocardium. It can be caused by toxins, drugs or infectious agents [20]. The inflammation can cause ventricular tachyarrhythmia due to electrical instability. It can also start an autoimmune reaction causing myocardial damage. This disease presents a clinical frame similar to the one of myocardial infarction, including wall motion abnormalities and ST-T changes on the electrocardiogram [20].

Congenital Heart Disease

A variety of conditions can be caused by abnormalities during embryonic development. These conditions are usually treated very early in life via surgical intervention. Over the patient's life time, mainly due to growth, a new surgery might be necessary. In this case, imaging is used to carefully follow-up the patients and discern whether a new surgery is necessary. Some examples of congenital heart diseases are: cardiac shunts[7], Tetralogy of Fallot, valve abnormalities, aortic coarctation, transposition of the great vessels [23].

Arrhythmias

Abnormalities in the heart rhythm are caused by problems with the electrical conducting system of the heart. Any electrical alteration ultimately affects its mechanical function. This mainly means that the timing of the contractile events are not synchronized and therefore the overall performance of the heart is impaired. A clear example is Left Bundle Branch Block (LBBB). Some patients with this type of electrical disorder present a mechanical reaction known as *septal flash* [24]. Septal flash is an early inward and outward motion of the ventricular septum. The contraction of the lateral wall is relatively delayed loosing the synchronicity of the contraction. Other examples of electrical disorders include: atrial fibrillation, ventricular tachycardia, ventricular fibrillation, atrioventricular block, sinus node disease, bundle branch blocks [7].

---

[6]Impaired ventricular contraction, which reduces the pumping capabilities of the heart.
[7]Holes that communicate the cardiac chambers.

1.2.2   Cardiovascular Care Cycle

To reduce the burden of CVDs, cardiological societies, such as the American Heart Association and the European Society of Cardiology, have taken the responsibility to develop guidelines for prevention, diagnosis and treatment of CVDs [25–30]. These guidelines are constantly updated to include new scientific evidence into the clinical cardiovascular care cycle [31].

Prevention

In 1966, the Framinghan study defined hypertension, smoking, diabetes, and hyperlipidemia as the major *coronary risk factors* [32]. These risk factors were then combined into *risk scores* for the evaluation of cardiovascular risk [33–36]. Using risk scores, these studies developed algorithms which allowed clinicians to predict whether a patient was in low, intermediate or high risk of developing a CVD. Usually, risk assessment is performed once the disease has manifested clinical symptoms, for instance an acute coronary syndrome. However, there are high risk asymptomatic patients who would greatly benefit from preventive cardiology [18, 30]. These patients can be identified in routine check-ups where some coronary risk factors can be found. To further evaluate CAD, pharmacological stress can be induced to evaluate ischemia in combination with echocardiography, radionuclide imaging (like SPECT) and MRI [28, 29]. Coronary calcifications are a clear sign of coronary atherosclerosis and they can be visualized in a CT scan. However, CT exposes the patient with x-ray radiation and therefore should be used carefully. Patients in high risk of developing a CVD will receive preventive treatment including pharmacological therapy and life-style changes, such as stoping smoking, dieting and exercising [30].

Diagnosis

Despite preventive measures, approximately 15 million patients are treated in the emergency room for suspected myocardial infarction every year in the USA and in Europe [37]. In an emergency setting, the priority is to decide whether the patient requires an urgent reperfusion procedure. This is decided considering case history, physical examination, electrocardiogram (ECG) analysis, blood sampling and imaging evidence [25,29]. The case history takes into account current symptoms and risk factors for coronary disease. The physical examination, such as blood pressure measurement and ausculation[8], can evaluate hemodynamic and respiratory alterations. The blood sampling can reveal the presence of enzymes, such as cardiac troponin and CK-MB[9], which indicate recent myocardial damage. The ECG can show abnormal patterns, specifically ST and T changes, which suggest myocardial infarction.

In the acute setting, imaging is commonly used with two purposes: *1)* ruling out or confirming the presence of infarction or ischemia, and *2)* identifying non-ischemic conditions causing chest pain [25]. The first purpose can be achieved with echocardiography by evaluating local motion abnormalities

---

[8]Listening to the internal sounds of the body with a stethoscope.
[9]The MB fraction of creatine kinase.

or with SPECT by directly measuring myocardial perfusion [29]. MRI, capable of evaluating wall motion and ischemia, is less used in the acute setting due to longer examination times. However, it is recommended if myocarditis is suspected since the inflammation displays a very distinct late gadolinium enhancement pattern [25]. The second purpose is known as *differential diagnosis*. It can reveal non-ischemic causes for the chest pain, such as valve defects, cardiomyopathies, pericarditis, myocarditis, hypertensive heart disease, pulmonary embolism and aortic dissection [26, 37].

Treatment

Once the reason for the chest pain is detected, patients will undergo treatment targeted to their specific condition. Patients with strong evidence of myocardial infarction will be urgently treated with pharmacological or mechanical reperfusion. Pharmacological reperfusion is achieved with fibrinolytic treatment and mechanical reperfusion is achieved by percutaneous catheterization (PCI) [29]. PCI often includes inflating an angioplastic balloon to reopen the vessel and placing a stent[10] to reinforce vessel structure.

Both ischemic and non-ischemic patients will receive pharmacological therapy and close monitoring to prevent the development of heart failure (HF). The symptoms of HF include shortness of breath at rest, fatigue, signs of fluid retention, and evidence of cardiac structure or function abnormalities at rest [8]. Depending on the underlying cause and the severity of HF, different treatments are recommended:

- *Pharmacological therapy:* this treatment aims to control heart rate, blood pressure, plasma lipids and diabetes [30]. A combined control of these processes can help balance hemodynamic conditions of cardiac function. For instance, hypertension can be managed by reducing circulating volume, inhibiting vasoconstriction and promoting vasodilation [30, 31].

- *Surgeries:* revascularization procedures aim to restore perfusion to the myocardium using PCI and/or coronary artery bypass grafting (CABG). Valvular surgery is used to repair or replace cardiac valves. It is recommended for patients with severe aortic stenosis, severe aortic, mitral or tricuspid regurgitation, or congenital valve defects [8]. Another type of surgery aims to remove portions of the myocardium. For instance, a ventricular aneurysmectomy for patients with large LV aneurysms or a septal myectomy for patients with obstructive HCM [8, 38]. Patients with congenital cardiac shunts may require surgery to close the septal communication [39].

- *Pacing:* if the natural pacing of the heart is impaired, the use of a pacemaker is recommended. Such is the case for patients with atrioventricular block or sinus node disease [7]. In patients with high risk of sudden cardiac death, such as HCM or DCM, implanting a cardioverter defibrillator is recommended [40]. The defibrillator will perform a rescue shock if the

---

[10]Small mesh tube.

patient goes into cardiac arrest. Another type of procedure, called Cardiac Resynchronization Therapy (CRT), uses a biventricular pacemaker to create a delay in electrical stimulation. CRT has been recommended in patients with severe HF and electrical dyssynchrony, although recent studies have suggested new criteria to select CRT candidates [41]. The delay is optimized for each patient to restore synchronicity [7].

- *Ablation:* ablation is performed with a catheter that applies a specific radiofrequency and causes a localized infarction. It is usually performed in patients with atrial fibrillation or ventricular arrhythmias to interrupt electrical pathways [7]. Alcohol ablation can be recommended in patients with severe HCM to reduce myocardial mass [38].

- *Heart transplantation:* heart transplantation is only recommended when no alternative treatment is available. This is due to the shortage of donor hearts and the possibility of rejection. To qualify for a heart transplant, the candidate should have no history of alcohol or drug abuse [8].

During treatment, imaging has two main roles: *1)* monitoring the progression of the a CVD, and *2)* guiding interventions. For cost-effectiveness reasons, the main monitoring modality is echocardiography, although in some patients transthoracic[11] and transesophageal[12] echocardiography may fail to provide enough diagnostic details. In such case, additional non-invasive imaging examinations, such as MRI, CT or SPECT, should be employed. For patients undergoing heart transplantation, both echocardiography and MRI can be used to monitor the long term adaptation effects of the transplanted heart [42].

Imaging guidance of interventions is a fast growing field. Typically, a preoperative imaging dataset is acquired. The preoperative image can be used to plan the intervention, aiding the selection of the type of device and implantation site. Revascularization procedures can be endorsed if evidence of viable myocardium is found. Myocardium viability is evaluated with SPECT, contrast enhanced MRI and, recently, contrast enhanced CT [9]. Other procedures that can be improved with image guidance include: aortic dissection/aneurysm, and congenital heart disease repairs [39].

A step further is to use preoperative information to guide the procedure itself. From preoperative imaging (MRI, CT), patient specific anatomical information is extracted. The anatomical information can be complemented with the localization of scar. The intraoperative overlay requires a special system that aligns the position of the patient with the preoperative image, and keeps it updated during the whole intervention. Two procedures that already benefit from image-guided interventions include ablation and CRT [43, 44].

---

[11]Suboptimal acoustic windows are usually due to obesity or small rib separation.
[12]Failure may be due to unsuccessful esophageal intubation and respiratory complications.
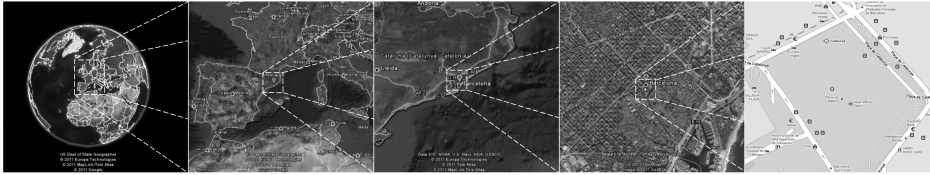
Figure 1.5: *Google Earth© a computational model of the Earth. Similarly, a computational model of the heart would include different sources of information. The information can be displayed as it becomes relevant to the level of detail and the point of view.*

1.3 Technical Motivation

1.3.1 From Mental to Computational

The imaging journey taken by the patients through the care cycle generates massive amounts of information. Clinicians collect bits and pieces of information to form a mental model. This integrative mental model displays a full picture of the condition of the patient. It is highly desirable to transform this mental model into a computational model. The computational model should be able to integrate the information in a comprehensive manner. The model should be built such that only relevant data is stored. Ideally, we should be able to display multiple levels, from organ to cell level. Each level of the model will then display the information relevant for that scale.

A good analogy to illustrate this idea is found in the tool Google Earth©. The tool gathers information from different sources and at different levels of detail. It allows to navigate from the globe, through different scales, to street level. The street level display also provides relevant localized information: restaurants, hotels, bus stops, etc (see Fig. 1.5). To be able to create such a model, we can recognize three main challenges:

Multimodal Integration

The concept of a *multimodal* scheme refers to the evaluation of the same patient with different image modalities. In the end, this allows to have information of the heart from several points of view. Inside the clinical environment the multimodal scheme is observed quite naturally (see Fig. 1.6).

This brings us to our first main challenge: multimodal integration. Data from different modalities is processed independently. Usually it is translated into a parameter which is considered relevant to classify the patient's pathology. Given that the parameters are calculated by different tools, they are not directly comparable. Ideally, information should be extracted from the various modalities by the same methodology or, better yet, by the same tool. Again, we find suitability for a statistical model-based approach. Once the statistical model is able to handle multimodal data, it can process the multiple datasets and calculate the desired parameters. Since the statistical model is the same for each dataset, we have a unified frame of reference with all the relevant information.
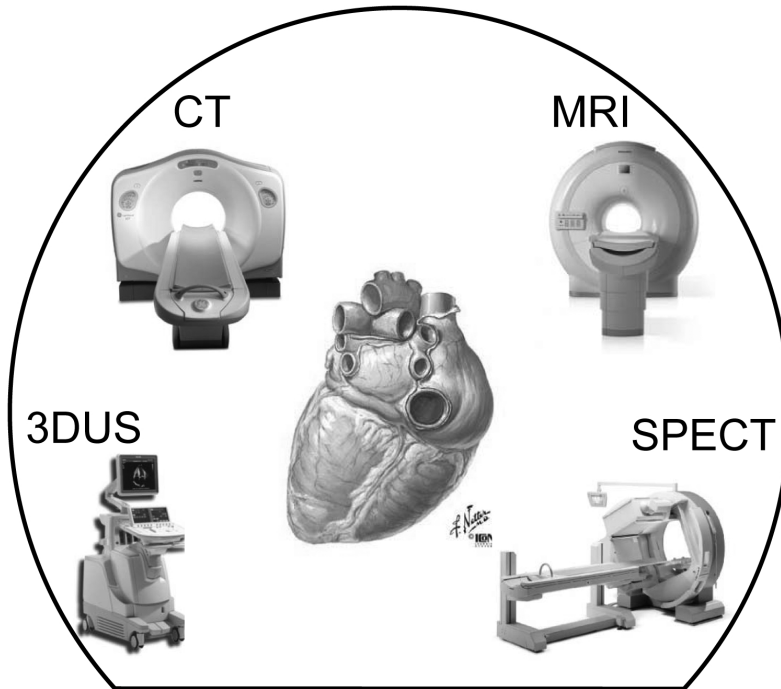
Figure 1.6: *In a clinical environment the multimodal scheme is observed naturally. The clinician in charge will mentally combine all the information to diagnose the patient. 3DUS= Three-dimensional ultrasound; CT= Computed Tomography; MRI= Magnetic Resonance Imaging; SPECT= Single Photon Emission Computed Tomography. (See color insert)*

Dimensionality Reduction

Our second challenge is the reduction of dimensionality: the amount of data collected during the clinical diagnostic pipeline needs to be reduced to simple, yet relevant, measurements. Currently it is mainly achieved by combining 2D measurements, such as wall thickness and ventricular diameters, with volumetric measurements. In this context, an approach based on a statistical model becomes very interesting. By deforming the statistical model to image data from a patient, the heart can be analyzed in a more holistic way. The analysis can be targeted to shape analysis: are there local/global thickness alterations? are the cavities proportional to each other? It can also be targeted to a dynamic analysis: is the contractility function uniform or unbalanced? is it normal or impaired? A statistical model-based approach allows to place the heart of a specific patient into a common frame of reference. This common frame of reference is known as *atlas*.
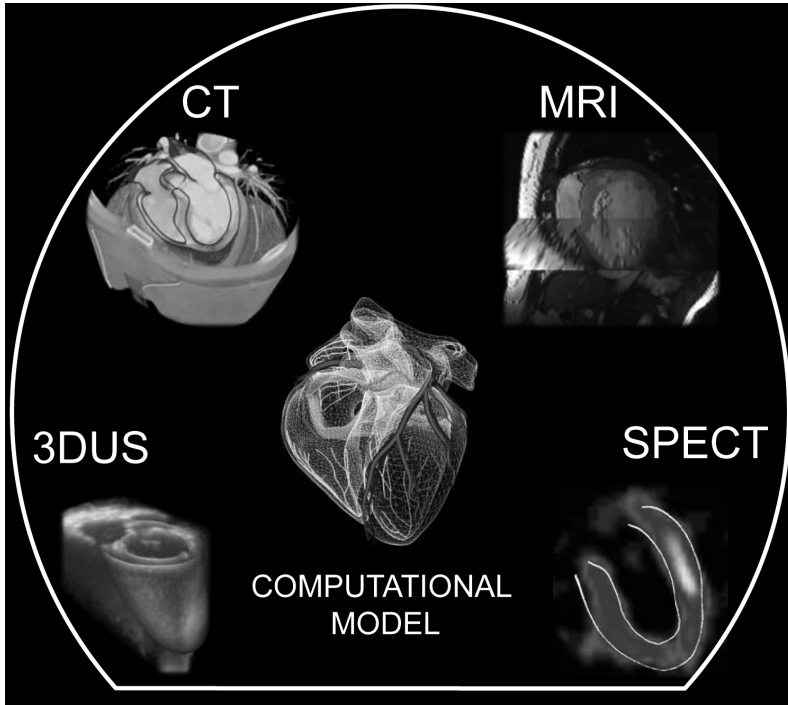
Figure 1.7: *Active Shape Models are a robust and accurate approach to quantify cardiac parameters from multimodal image data. They can evaluate the spatio-temporal variability of the heart. 3DUS= Three-dimensional ultrasound; CT= Computed Tomography; MRI= Magnetic Resonance Imaging; SPECT= Single Photon Emission Computed Tomography. (See color insert)*

Pathology Classification

Clinicians, thanks to previous knowledge and experience, hold a pattern of normality in their mind, which allows them to compare the condition of one patient to a pattern of normality. Statistical atlases allow us to mimic this behavior. Although initially atlases were employed as a simple template, they have evolved to encode shape variability within a population. This variability information allows to compute the distance between a patient-specific geometry and the mean atlas [45]. This distance can be related to a CVD and, therefore, it can be used to aid the diagnosis.

1.3.2   Approach

Keeping in mind all the requirements and challenges presented above, we desire an approach that:

- is able to accurately segment the cardiac cavities from multimodal datasets: this implies flexibility in the type of structure (i.e. one or two ventricles) and the image appearance information (i.e. SPECT or MRI).

- provides a unified frame of reference to integrate multiple information sources: this targets the idea of displaying the clinicians mental model of the patient's heart in a computational manner.

- aids the classification of a patient's cardiac condition: this requires a priori statistical knowledge of normality and pathological conditions.

Our idea is that statistical shape models, in particular Active Shape Models (ASM), are a robust and accurate approach with the potential to incorporate the aforementioned requirements (see Fig. 1.7). We evaluate this idea in the context of left ventricular segmentation from SPECT datasets and bi-ventricular segmentation from MRI datasets [46–48]. Within our research group, an extension to 3DUS has been carried out [49]. In the next chapter we will elaborate on the implementation issues tackled in this thesis.

2

Towards an Automatic Construction of Active Shape Models

2.1   Context

Model-based object recovery from images is a problem that has motivated over 30 years of research in computer vision. Early applications employed rigid models to recognize man-made parts in industrial systems [50]. The models incorporated a priori shape information into the recognition task. These models evolved from rigid to flexible and doing so brought *deformable models* into the picture [51]. Deformable models allowed to constrain and regulate a problem that is, in general, ill-posed. Hence, they were quickly adopted by the research community. Among them, statistical shape models have been particularly relevant since they allow to encode population variability, a very desirable characteristic in medical image analysis. In particular, Active Shape Models (ASMs) have been widely employed to segment organs from medical images. Before unleashing their great potential, ASMs must be properly trained. The training process, however, has a few non-trivial requirements. Automatizing this process has motivated over two decades of research, which has brought us a long way towards an automatic construction of ASMs.

2.1.1   Active Shape Models

ASMs constitute a statistical deformable model approach which includes a priori information about the shape of the object of interest [51]. The shape information is encoded into a template known as a Point Distribution Model (PDM). The template is deformed to outline an unseen object within an unseen image. The PDM, as its name indicates, is based on a collection of points. These points are known as *landmarks* [52]. Fig 2.1 shows examples of landmark positions representing familiar objects. All training shapes are required to have equal amount of landmarks. The landmarks are labeled such that landmarks with the same label represent the same location of the physical object in every training shape. This is known as *point correspondence*. Once a full set of training shapes with point correspondences is available, the PDM can be constructed by applying Principal Component Analysis (PCA). PCA will include statistical information regarding shape variability into the PDM. That is, the principal

(a)   (b)   (c)   (d)
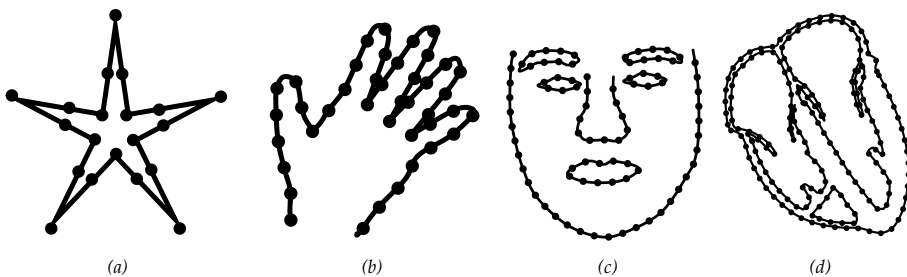
Figure 2.1: *Examples of landmark positions representing the boundary of familiar objects: (a) a star, (b) a hand, (c) a face, and (d) a heart. As the shape becomes more complex, more landmarks are necessary to described it.*

modes of variation of the training samples are used to compute valid instances of the object.

   Still, a fully trained PDM is not enough to recognize the object in the image. The model needs to learn the typical image appearance around the object. This is usually achieved by sampling profiles perpendicular to the object's contour (see Fig. 2.2). Similarly, profiles are collected for every landmark of every sample in the training set. From them, an *intensity model* is computed for each landmark. The intensity model will include: a mean profile (to account for average image intensity values) and a covariance matrix (to account for image variability). In the end, a *matching algorithm* will use this intensity information to look for possible edges and yield the shape instance that best fits to the unseen data being processed.

2.1.2   Training Steps

Going over the training steps necessary for ASM construction, can help us identify possible bottle necks:

1. *Manual outlining:* as a starting point the target object needs to be identified in the training images. This means delineating the object in every image of the training set. Given that shape information will come from these delineations, it is common practice to obtain them manually. In 3D applications, the outlining needs to be performed in every slice of every sample volume. This constitutes a major bottle neck, and often limits the sample size from which ASMs are built.
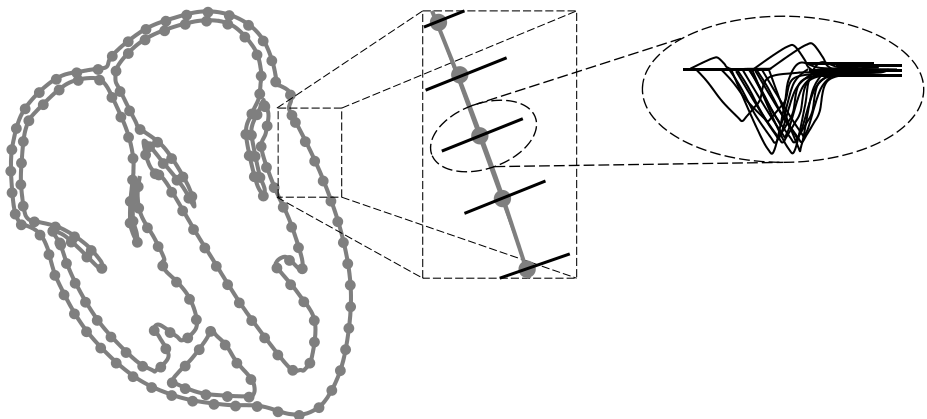
Figure 2.2: *Explanatory diagram of intensity model construction. Profiles are sampled perpendicularly to the contour of the object. At the location of each landmark, profiles are collected for every training set. The intensity model will include: a mean profile (to account for average image intensity values) and a covariance matrix (to account for image variability).*

2. *Point correspondence:* the manually outlined objects need to be landmarked. As stated above, the landmarks should be consistent in number and position. Assuring point correspondences over a large database is a labor-intensive task. For early 2D applications, this step was achieved manually. For 3D applications, the amount of landmarks needed to describe the object increases considerably. This makes it nearly unfeasible to assure point correspondences with manual interaction alone.

3. *Point Distribution Model:* once step 1 and 2 are achieved successfully, we are ready for PDM construction. First, shapes are aligned to remove variations due to position, scale and rotation [52]. Second, PCA is carried out from the aligned shapes. In this manner, the principal modes of variation account for elastic deformations among shapes, not for pose or size differences.

4. *Intensity model:* intensity model training can be obtained from the same set that is used for PDM construction. For an application targeted to a unique image modality, this training set is sufficient. For a multimodal application, on the other hand, the information obtained from the PDM training set is not enough. Given that image appearance changes from one modality to another, the ASMs require retraining. This brings us back to step 1.

2.1.3   Automatic Construction of Active Shape Models

Due to the complications mentioned above, several techniques for automatic training of ASMs have been developed. The first training step, manual outlining, is hard to avoid. In fact, initially all automatic techniques for PDM construction started from a database of segmented objects [53–57]. These studies aimed to automatically obtain point correspondences. We can recognize different types of approaches. A first type of approach in which segmented objects are landmarked and later point correspondences are optimized [53–55]. They differ from one another on the optimization technique. The second type of approach, proposed by Frangi *et al.* [56], in which all the shapes in the training set inherit the landmarks from an atlas. The atlas is computed from labeled volumes obtained from the manual segmentations. The labeled volumes are registered to a normalized coordinate system. In this normalized coordinate system, an average shape (atlas) is computed and landmarked. Landmark positions are propagated back to the original segmented volumes using the inverse of the registration transforms. Kaus *et al.* [57] proposed a technique which creates a triangulated surface from one labeled volume. The resulting mesh is adapted to the other labeled volumes, preserving point correspondences. Rueckert *et al.* [58] proposed a technique which bypasses the manual outlining step. An average volume (atlas) is obtained directly from the original intensity images (raw data) by using non-rigid registration. The manual annotation is performed only once over the average volume. The landmarks are mapped back to every training shape, similarly to Frangi *et al.* [56]. This approach was evaluated on MRI datasets to construct a PDM of the brain with positive results [58]. Whether this approach would be able to catch the inter-subject and temporal variability

of the heart, was studied by Ordas *et al.* [59]. In this study, a whole heart model was successfully constructed from 100 high resolution CT datasets. Lorenz and von Berg [60] proposed a technique to avoid manual outlining of every sample. The approach uses a boot-strap method which works directly on the original intensity images.

Table 2.1 summarizes these techniques for automatic construction of ASMs within the medical imaging field. We can observe some interesting aspects. First, most of the efforts made on the automatization of ASM construction were targeted to PDM construction. Second, given that early techniques depended on manual segmentations as initial data, the ASMs were often built from relatively few samples. Third, the final step of intensity model training had been overlooked until very recently. The need for automatizing this step became more evident thanks to the proliferation of multimodal datasets in the patient care cycle (see Chapter 1.2.2). The proposed approaches all coincide in the idea of reusing a PDM trained from a high resolution imaging modality and collecting appearance information from a different source [46, 61, 62]. Van Assen *et al.* [62] proposed to use a fuzzy inference system based on relative intensity differences, bypassing the need for an intensity model. This technique was tested in CT and MRI. Peters *et al.* [61] proposed to use a few manual delineations for each modality. The delineations were then propagated and refined with a simulated search method. This approach was applied to CT, MRI and Rotational Angiography.

2.2   Contributions

This is the context in which this thesis was developed. Working towards our desired approach (see Chapter 1.3.2) the first step was to generate a PDM able to capture a wide range of spatio-temporal variability of the heart. This step was tackled within our research group by Ordas *et al.* [59] and, more recently, by Hoogendoorn *et al.* [64]. In this work a statistical shape model representing the whole heart was constructed from CT datasets. The model includes 20 subpart labels. The combination of these labels results on different model configurations. Possible configurations include: a left ventricular model for SPECT and US datasets, a bi-ventricular model for MRI datasets, and a full heart model for CT datasets. The PDM was built from 100 patients in 15 cardiac phases, totalling 1500 training volumes. Taking into account typical sample sizes for PDM construction (Table 2.1), we can consider this a to be large sample. In this sense, we can expect this shape model to meet our requirements of accuracy and robustness, with the added value of a multi-configuration scheme.

Aiming to preserve this shape information, we were challenged to find an alternative way to include appearance information from other modalities into the model. The answer to this challenge came from the field of image acquisition modeling. Hereby, the physics of the imaging technique is simulated to generate virtual images of computer models of, in our case, the heart. For brevity, we will refer to these images as simulated datasets. Over the last decade, a number of simulators have been developed. They are capable of modeling the physics and acquisition process of medical imaging with great detail.

TABLE 2.1: Automatic techniques for ASM construction in medical imaging

Author	Year	Object	n	Modality	Initial Data	Approach
PDM construction						
Subsol et al. [53]	1998	Skull	6	CT	Semi-automatic segmentations	ICP registration of labeled volumes
Brett et al. [54]	2000	Brain ventricle	8	MRI	Manual segmentations	ICP registration of surfaces
Davies et al. [55]	2002	Left Ventricle	38	US	Manual segmentations	MDL optimization of point correspondence
Frangi et al. [56]	2002	Left/Right Ventricles	14	MRI	Manual segmentations	Non-rigid registration of labeled volumes
Kaus et al. [57]	2003	Bones	21	CT	Manual segmentations	Adaptation of deformable model to labeled volumes
Rueckert et al. [58]	2003	Whole Brain	25	MRI	Raw images	Non-rigid registration of raw images
Lorenz and von Berg [60]	2006	Whole Heart	27	CT	Raw images	Boot-strap method on raw images
Ordas et al. [59]	2007	Whole Heart	100	CT	Raw images	Non-rigid registration of raw images
Intensity model						
van Assen et al. [62]	2008	Left Ventricle	53	MRI/CT	MRI manual segmentations	Fuzzy inference of relative intensity differences
Tobon-Gomez et al. [46][†]	2008	Left Ventricle	208	SPECT	NCAT virtual phantom [63]	Simulating the physics of image acquisition
Peters et al. [61]	2010	Whole Heart	13/42/33	CT/MRI/RA	Few manual segmentations	Propagation of segmentations with Simulated Search

ICP= Iterative closest point; MDL= Minimum descriptor length; CT= Computed Tomography; MRI= Magnetic Resonance Imaging; US= Ultrasound; SPECT= Single Photon Emission Computed Tomography; RA= Rotational Angiography; †= Within the scope of this thesis.
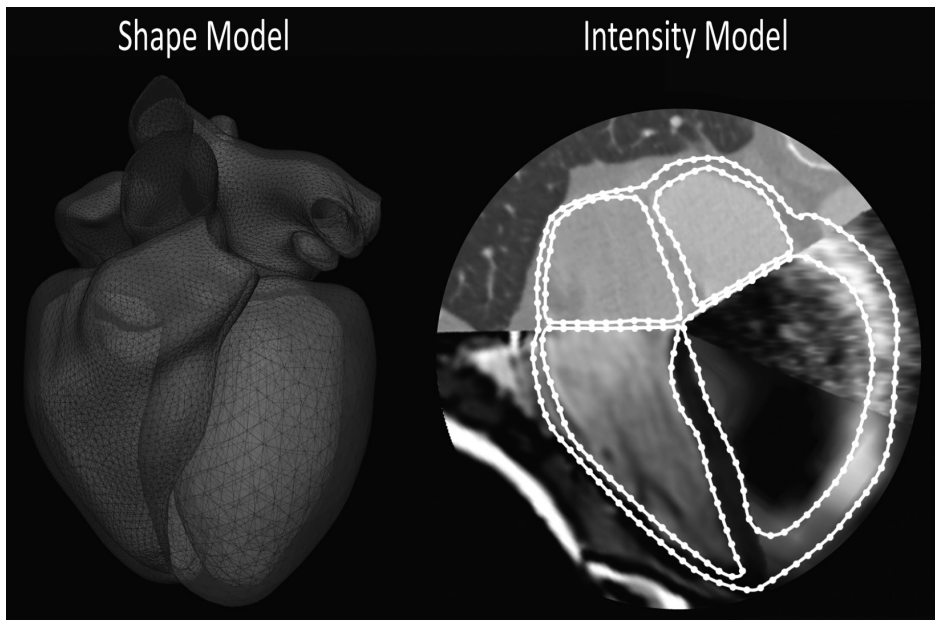
Figure 2.3: *We use a 3D shape model built from CT datasets. The shape information is complemented with intensity information specific to each modality by simulating the physics of acquisition. (See color insert)*

Imaging simulators provide tools for a variety of modalities: SPECT [65–67], CT [68, 69], US [70], and MRI [71, 72]. By simulating the physics of acquisition, we were able to complement the shape information with intensity information specific to each modality (see Fig. 2.3). Given that SPECT simulators have the longest trajectory and provide straightforward tools for cardiac applications, we chose this modality for an initial evaluation of our approach. The results showed that clinical SPECT studies can be successfully segmented by models trained under this scheme. Details on the implementation and evaluation of the methodology will be presented in Chapter 3. At that point, we had implemented the first contribution of this thesis: *a method to automatically construct intensity models for ASMs, based on simulating the physics of acquisition of the given imaging modality.*

To continue developing our methodology, the next step was to extend this method to MRI. We found that the state of the art of cardiac MRI simulation was not as advanced as expected. On the one hand, MRI simulators were widely used for brain applications, yet hardly used for cardiac applications. On the other hand, cardiac digital phantoms were targeted mainly to low contrast imaging modalities, such as SPECT. Hence, they lacked the amount of detail required for a modality with high tissue contrast, such as MRI. This motivated the second contribution of this thesis: *the first extension of an MRI simulator tailored to produce realistic cardiac images.* The extension was based on the MRISIM simulator [72] and the XCAT [73] digital phantom. Digital phantoms were modified in order to include relevant intracavitary structures. The pro-

posed approach obtained a noticeable improvement of the local appearance of the simulated images with respect to the ones obtained originally. Full details will be presented in Chapter 4.

Using the improved simulated datasets developed in Chapter 4, we implemented the third contribution of this thesis: *a novel automatic intensity model and reliability training strategy applied to cardiac MRI studies*. In this strategy the intensity information was complemented with the reliability measure for statistical shape models proposed by Sukno *et al.* [74]. Both the intensity models and the reliability information, were obtained from the simulated datasets. The inclusion of reliability information during matching proved to increase robustness of the segmentation process. It made it less sensible to initialization and reduced the outliers in difficult areas, such as areas with local minima and/or high partial volume effect. Full details will be presented in Chapter 5.

These contributions will be presented in detail in the following three chapters. Each chapter was made self-contained and represents an article published or submitted to a peer-review archival journal.

3

Automatic Construction of 3D-ASM Intensity Models by Simulating Image Acquisition: Application to Myocardial Gated SPECT Studies

Catalina Tobon-Gomez, Constantine Butakoff, Santiago Aguade,
Federico M. Sukno, Gloria Moragas and Alejandro F. Frangi

Abstract

Active shape models bear a great promise for model-based medical image analysis. Their practical use, though, is undermined due to the need to train such models on large image databases. Automatic building of Point Distribution Models (PDMs) has been successfully addressed and a number of autoland-marking techniques are currently available. However, the need for strategies to automatically build intensity models around each landmark has been largely overlooked in the literature. This work demonstrates the potential of creating intensity models automatically by simulating image generation. We show that it is possible to reuse a 3D PDM built from Computed Tomography (CT) to segment gated Single Photon Emission Computed Tomography (gSPECT) studies. Training is performed on a realistic virtual population where image acquisition and formation have been modeled using the SIMIND Monte Carlo simulator and ASPIRE image reconstruction software, respectively. The dataset comprised 208 digital phantoms (4D-NCAT) and 20 clinical studies. The evaluation is accomplished by comparing point-to-surface and volume errors, against a proper gold standard. Results show that gSPECT studies can be successfully segmented by models trained under this scheme with sub-voxel accuracy. The accuracy in estimated LV function parameters, such as End Diastolic Volume, End Systolic Volume and Ejection Fraction, ranged from 90.0% to 94.5% for the virtual population and from 87.0% to 89.5% for the clinical population.

3.1   Introduction

In spite of the high technological developments in medical imaging systems for diagnostic cardiology, cardiac function is still mostly analyzed through visual assessment or manual delineation, which are both time consuming, subjective and error prone. This fact has generated the need for automated analysis tools to support diagnosis with reliable and reproducible image interpretation. However, the success of currently available commercial packages is modest and their use under-diffused.

On the one hand, automated delineation of the cardiac chambers from 3D and 4D image datasets is challenging. Recent surveys have pointed out the prevalence of model-based approaches to accomplish this task [75, 76]. Typically, they require a generic template which undergoes adaptation to fit specific image data. This strategy enables introducing a priori knowledge of shape of the structure of interest into the segmentation process. In particular, Active Shape Models (ASMs) [51] have been successfully employed in image segmentation [77,78]. Unfortunately, construction of these models requires several training steps based on a target image database (ideally a rather extensive one). This is simply unachievable by sole manual processing on 4D datasets due to the huge amount of data involved. These steps include: *1)* manual outlining of target boundaries, *2)*consistent distribution of landmarks across sample shapes, *3)* statistical shape decomposition yielding a Point Distribution Model (PDM) [51], and *4)* learning a statistical model of the intensity around the target object. Substantial efforts have been carried out to automatically construct

PDMs by autolandmarking surface [53–55] or volumetric [56, 57] representations of already segmented structures. Some authors have shown techniques which circumvent the need for segmenting all sample volumes and work directly from the raw images [58, 59].

To the best of our knowledge, no work has attempted to automate the process of creating intensity models. This is precisely the focus of this work, which we use to complement our fully automatic ASM construction strategy initiated with the autolandmarking method by Frangi *et al.* [56], and more recently by Ordas *et al.* [59]. We show that it is possible to build a 3D-ASM, suitable for segmentation of gated Single Photon Emission Computed Tomography (gSPECT) images, with a PDM previously built from a large database of cardiac Computed Tomography (CT) data [59]. The use of a virtual population provided access to known LV surfaces for training purposes and accuracy evaluation.

On the other hand, imaging simulators are currently a mature field of research providing tools for a variety of modalities: SPECT [65–67], CT [68, 69], Ultrasound (US) [70], and Magnetic Resonance Imaging (MRI) [71, 72]. Among them, SPECT simulators have the longest trajectory, hence they now offer straightforward tools for cardiac applications. This has motivated the use of gSPECT as a show case for the usage of our approach. Nonetheless, the underlying concepts regarding automatic building of statistical shape models can be applied to other major diagnostic imaging modalities.

Segmentation of the LV cavity from SPECT imaging is a challenging problem owing to limitations inherent to the modality (i.e. low resolution, blurred boundaries, high noise levels, signal drops, absence of anatomical landmarks, etc) [79]. Model-based postprocessing algorithms are quite widespread in clinical practice [80, 81]. Yet their quantifications are affected by intrinsic imaging drawbacks, specially in patients with small or hypertrophic hearts [82]. Similarly, less accurate calculations have been found in the presence of extracardiac activity, low-dose studies or severe perfusion defects [83, 84]. Hence, new approaches able to cope with these constraints are highly desirable. Deformable models [85] and level set based [86] algorithms are more sophisticated approaches previously applied to SPECT segmentation, giving promising results on simulated data. Still, further validation on real clinical cases is needed.

This manuscript is organized as follows: the theoretical background of ASMs is explained in Section 5.2. The datasets used for our experiments are presented in Section 4.2. A detailed description of the methodology for automatic construction of 3D-ASM intensity models is provided in Section 3.4. Section 3.5 presents the experimental setup of this work, followed by its results in Section 4.3. Section 3.7 aims to further discuss the obtained results. Finally, the last section exposes the clinical contribution and outlook of our work.

3.2   Background

A concise explanation of Active Shape Models (ASM) is provided in the current section. An extended description can be found in [51].

Basically, three main parts constitute the backbone of an ASM: a shape model, an intensity model, and a matching algorithm. The shape model (PDM)

represents the shape variability of the object under study. For a three dimensional space, a linear PDM constructed from n aligned shapes, $\{x_i; i = 1, \ldots, n\}$, of m landmarks each, $\{l_j = (l_{xj}, l_{yj}, l_{zj}); j = 1, \ldots, m\}$, is a linear model defined by:

$$x = \bar{x} + \Phi b \tag{3.1}$$

where x is a $3m$-element vector obtained by concatenating all landmark coordinates in the form $(l_{x1}, l_{y1}, l_{z1}, l_{x2}, l_{y2}, l_{z2}, \cdots, l_{xm}, l_{ym}, l_{zm})$. Then, $\bar{x}$ is the mean of aligned shapes in the training set, b is the shape parameter vector of the model, and Φ is a matrix whose columns are the principal components of the covariance matrix:

$$S = \frac{1}{n-1} \sum_{i=1}^{n} (x_i - \bar{x})(x_i - \bar{x})^T \tag{3.2}$$

Obtaining the m 3D landmarks and their correspondence for all points on every dataset is not a trivial task. Our methodology was inspired on the method proposed by Frangi *et al.* [56]. Because of our particular application, a one chamber model (LV) was used. Such configuration is a subpart of our recently constructed whole heart model, trained from a high-resolution CT dataset [59]. Its training included 100 subjects in 15 temporal phases. Thus, 1500 sample volumes were considered in total.

Once the shape model has been established, the second component (intensity model) comes into action. It aims to grasp the intensity distribution typically found near the object's boundaries. It does so by sampling the gradient of the intensity profiles along the perpendiculars to the mesh. From pixels sampled along each profile, the mean vector and covariance matrix are estimated and stored for later use during matching. An intensity model was calculated for each endocardial and epicardial wall of the 17 LV AHA's segments [87]. Hence a total of 33 regions were obtained, corresponding to 17 epicardial and 16 endocardial.

Finally, the third element (matching algorithm) has the role of deforming the mesh to match image data. Our approach is based on the sparse fitting method, SPASM, put forward by van Assen *et al.* [77]. We modified this technique by using an intensity model where each candidate point is obtained by selecting the minimal Mahalanobis distance between the sampled profiles and the mean profiles of the intensity model. Candidate points operate as deformation forces propagated to neighboring nodes with a weight function

$$w(\lambda, \omega) = e^{-\frac{\|\lambda - \omega\|^2}{2\sigma_p^2}} \tag{3.3}$$

where $(\|\lambda - \omega\|^2)$ is the geodesic distance between nodes, and σ_p is the width of the normalizing Gaussian kernel. Deformation forces drive the mesh to a best-fit location after several iterations. The steps of the algorithm are illustrated in **Algorithm 2**.

Algorithm 1 Matching Algorithm: *SPASM*

 1: InitialMesh←Initialize mean Mesh
 2: **repeat**
 3:     **Intersect**(ImageStack,InitialMesh)
 4:         **for all** Intersection points **do**
 5:             Find closest mesh vertex
 6:         **end for**
 7:         CountourStack←Create 2D contours
 8:     **Candidates**(CountourStack,LearnedProfiles)
 9:         **for all** Possible profile positions **do**
10:             Mahalanobis(LearnedProfiles,SampledProfiles)
11:         **end for**
12:         CandidatePoints←Smallest Mahalanobis
13:     **ForcePropagation**(CanditatePoints)
14:         **for all** CandidatePoints **do**
15:             UpdateVectors←Calculate weight function w
16:         **end for**
17:         Forces←Project UpdateVectors to surface normals
18:         DeformedShape←Apply forces to mesh
19:     **NewValidInstance**(DeformedShape)
20:         BestFit←Best parameters to fit DeformedShape
21: **until** Iterations completed or convergence achieved

3.3   Materials

Two main datasets were used for this work: a virtual and a clinical population. The virtual population consisted of digital phantoms (see Section 3.4.1 for details) and was considered for 3D-ASM intensity model training. Afterwards, it was employed to evaluate performance of the trained models by means of leave-one-out approach: each case was segmented by a model trained with all cases but itself (in total $n-1$ cases).

The clinical population, on the other hand, was only used for performance evaluation. It included 20 subjects of which 2 were healthy, 2 hypertrophic, 11 infarcted and 5 dilated. A rest gSPECT study and an MRI study were obtained for each subject with a mean interval of 53 days given no change in clinical condition.

Gated SPECT studies were acquired at a rate of eight frames per cardiac cycle. Patients were imaged one hour after administration of 99mTc-tetrofosmin using a Siemens ECAM SPECT system (Siemens Medical Systems, Illinois, USA) or an ADAC CardioEpic system (Philips Medical Systems, Best, NL) both with a double-detector at 90° with high resolution collimators. Sixty-four projections of a 64×64 matrix over 180° arc were obtained with a 6.60mm/pixel resolution. Image data was reconstructed with *Filtered Back-projection* (see Fig. 3.1). MRI studies were acquired using a General Electric Signa CV/i, 1.5 T scanner (General Electric, Milwaukee, USA). Datasets contained short-axis image stacks at 30 temporal phases. The slice thickness was 8mm with an in-plane pixel resolution of 0.78mm × 0.78mm.
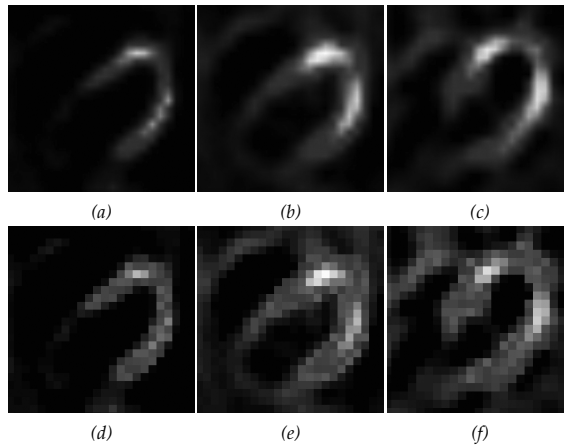
Figure 3.1: *Interpolated (top) and original (bottom) axial views of a virtual (a-b, d-e) and a clinical (c,f) gSPECT study. They were reconstructed by means of OSEM (a,d) and FBP (b-c, e-f). FBP= Filtered Back-projection; OSEM= Ordered-subset Expectation Maximization. (See color insert)*

3.4 Methods

In the current section our methodology for automatic construction of intensity models for 3D-ASM is described thoroughly. For an overall view of the complete pipeline, refer to Fig. 3.2.

3.4.1 Digital Phantoms

To ensure a realistic representation of a clinical population, several anatomical parameters were modified in a random manner, as proposed by He *et al.* [88], resembling a normal distribution obtained from the Emory PET thorax model database [89]. The minimal population size, n, was calculated following the criteria exposed by Jain *et al.* [90]. In our case, close to twenty parameters were modified during patient generation, yielding $n_{min} = 200$. Detailed description of modified parameters follow.

Anatomical Variations

Aiming to include anatomical variations which induce usual attenuation artifacts (i.e. breasts or high diaphragms) [91], three main anatomical groups were implemented (see Fig. 3.3):

- *Normal subjects:* featuring males with a flat diaphragm and females with small breasts.

- *Male subjects with high liver dome:* half the male subjects present a high liver dome, creating strong edges which may attract segmentation algorithms.
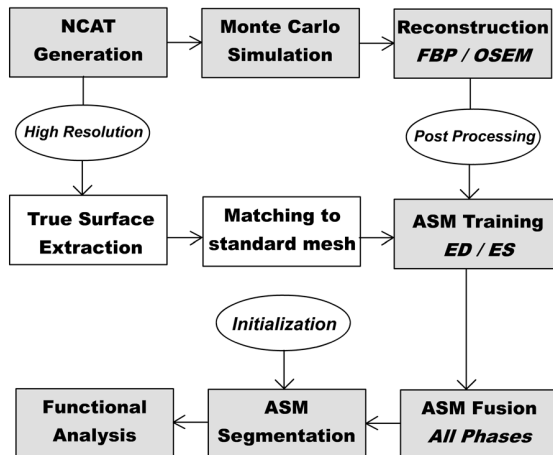
Figure 3.2: *Overall description of the pipeline for construction of 3D-ASM intensity models. Main steps are represented in grey blocks and complementary steps in white ones. FBP= Filtered Back-projection; OSEM= Ordered-subset Expectation Maximization; ED= End diastole; ES= End systole.*

- *Female individuals with large breasts:* breast size, position and orientation were modified in order to represent possible attenuation effects.

In order to generate the population, eight representative individuals were chosen from the Emory PET thorax model database [89]. With these eight anatomical models, four male (*M*1, *M*2, *M*3, *M*4) and four female (*F*1, *F*2, *F*3, *F*4), a total of 208 subjects were created, for which half the males present a high liver dome and half the females were attributed large breasts. Fig. 3.4 presents a graph which illustrates the general distribution of the virtual population. Parameters used as NCAT input are summarized in Table 4.2.

TABLE 3.1: TORSO PARAMETERS OF FEMALE AND MALE SUBJECTS.

		Body		Ribcage	
		LA	SA	LA	SA
Gender	Model	*cm*	*cm*	*cm*	*cm*
Female	F1	29	18	22	14
	F2	31	21	23	16
	F3	33	24	24	19
	F4	32	26	26	20
Male	M1	39	22	25	17
	M2	37	26	22	18
	M3	35	27	25	21
	M4	38	28	27	19

LA= Long-axis; SA= Short-axis.
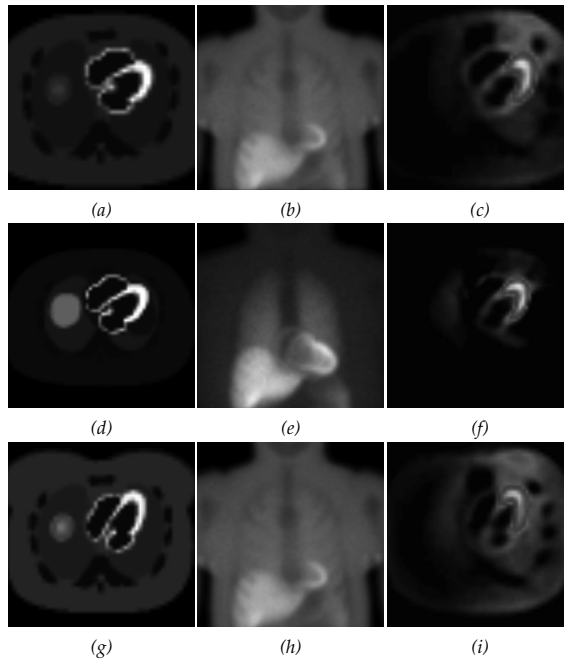
Figure 3.3: *Sample of the three anatomical groups: normal subjects (a-c), male subjects with high liver dome (d-f) and female individuals with large breasts (g-i). Images were generated with NCAT (left), SIMIND (middle) and ASPIRE (right), respectively.*

Heart Variations

The heart of each subject was varied by modifying its length and left ventricular basal radius. Global position was altered by inducing different orientation angles and translations of the heart along posterior-anterior (P-A) and lateral (Lat) directions. Specific parameters are summarized in Table 3.2.

Organ Uptake Ratios

Tracer uptakes of organs differ from patient to patient. To mimic this physiological condition, heart, liver, lung, kidney, spleen and background isotope uptake ratios were also modified in a random manner resembling a normal distribution of a typical clinical population [88]. Parameter values are displayed in Table 3.3.

Phantom Generation

Each voxel phantom included activity and attenuation files for 8 phases of a normal (1 second) cardiac cycle. Each set consisted of 98 slices of 64×64 pixels with a 6.25mm isotropic voxel size. This low resolution matches the usual conditions present in our clinical studies.
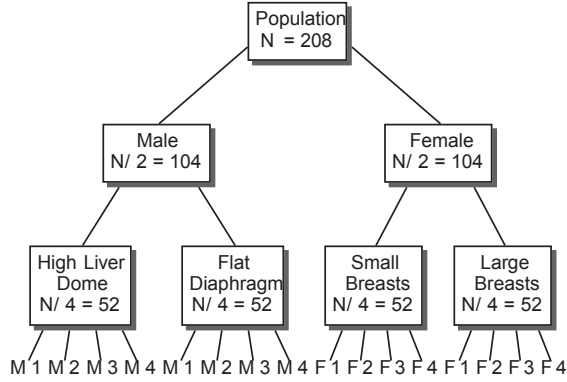
Figure 3.4: *General distribution of the virtual population, subdivided into anatomical groups. See Section 3.4.1 for details.*

TABLE 3.2: ANATOMICAL PARAMETERS FOR HEART VARIATION ACCORDING TO GENDER. ADAPTED FROM [88].

		Size		Orientation		Translation	
		Length	Ratio	Angle ϕ	Angle ψ	Lat	P-A
Gender	Measure	*cm*		°	°	*cm*	*cm*
Female	mean	7.4	3.20	27	40	5.2	-5.0
	SD	0.9	0.30	9	13	1.1	2.6
	max	10.5	4.00	54	76	8.5	0.2
	min	5.7	2.44	8	16	3.0	-10.6
Male	mean	8.3	3.17	21	36	5.6	-6.4
	SD	0.9	0.40	9	12	1.1	2.6
	max	11.6	4.32	41	73	8.0	1.2
	min	6.6	2.29	0	15	3.5	-11.6

Lat= lateral; P-A= posterior-anterior; SD= standard deviation.

Up to this point the anatomical models included a full thorax model that incorporates structures other than the heart, which are important for realistic gSPECT simulation. Aiming to extract LV true surfaces, higher resolution images with only the LV structure were generated. They consisted of 321 slices of 512×512 pixels each, with a 0.78mm isotropic voxel size. Once true surfaces were extracted from these datasets, our 3D model was aligned to them using a similarity transformation through Procrustes Analysis [92]. Subsequently, nodes of the true surfaces acted as exact candidates to deform our mean shape using one iteration of the ASM algorithm. This process allowed warping the atlas model to all the training shapes in order to assure: *1)* control over the distribution of clinical parameters in our training database of heart shapes based on published data, *2)* the same number of nodes and mesh topology for all true LV surfaces, and *3)* the inclusion of high inter-subject and inter-phase variability during the matching process since the PDM is based on a larger database of real patient data.

TABLE 3.3: TYPICAL DISTRIBUTION OF TRACER UPTAKE RATIOS
ON DIFFERENT ORGANS. ADAPTED FROM [88].

	Intensity	Ratio		
	Heart	Liver/	Lung/	Background/
Measure	Value	Heart	Heart	Heart
mean	1419	0.44	0.14	0.11
SD	810	0.19	0.04	0.05
max	4236	1.30	0.25	0.29
min	490	0.16	0.05	0.02

Ratio= with respect to heart uptake; SD= standard deviation.

3.4.2   Monte Carlo Simulation

In order to generate gSPECT studies for the virtual population, Monte Carlo simulation was employed using SIMIND code [65]. Details regarding the simulation set-up are given below.

Collimator Parameters

SIMIND allows for modeling different types of collimators. A Siemens Low Energy High Resolution (LEHR) collimator was chosen since it resembles our current clinical conditions [93]. Characteristics of such a collimator include: hexagonal shape, parallel hole collimator, radius of rotation of 20cm, hole size of 1.24mm, septal size of 0.90mm and thickness of 23.6mm.

Projection Parameters

Noise free projections were obtained by simulating 10^7 photon histories per projection. Sixty-four of them were obtained over a $180°$ arc, from $45°$ left posterior oblique to $45°$ right anterior oblique. Each projection consisted of a 64×64 matrix with 6.25mm/pixel resolution. Energy resolution was set to 9% *Full-Width-at-Half-Maximum* (FWHM) at 140 KeV and energy window threshold to 15% photopeak at 140 KeV.

System Characterization

Ordered-subset Expectation Maximization (OSEM) reconstruction requires FWHM parameters to be determined (see Section 3.4.3). This was accomplished by measuring point-sources at different distances from the collimator surface. The point source response was approximated to a symmetric Gaussian by means of nonlinear least squares fitting [94].

Image Generation

Simulations were run using grid computing on a cluster facility of 20 dual-processor dual-core SGI Tezrix 210/2, 3Ghz/1333 Mhz, Intel Woodcrest processors. InnerGrid v5.0 (GridSystems, Palma de Mallorca, Spain) was employed as

grid middleware. Distribution was achieved in the following manner: each subject corresponds to eight digital phantom datasets (one for each cardiac phase), totalling 1664 digital phantom (208 subjects $\times$ 8 time frames). Each dataset includes sixty-four projections, which were distributed to different nodes of the cluster such that one node will simulate only one projection of one digital phantom. The whole set of projections was then concatenated to obtain full projection volumes. This methodology allowed us to reduce computation time from 16 hours to 48 minutes per subject. For the whole database it represented trading 5 months of calculations for about 7 days.

3.4.3 Tomographic Reconstruction

Aiming to obtain datasets with different intensity features for our model training (see Section 5.2) tomographic reconstruction after simulation was performed in two approaches: *Filtered Back-projection* (FBP) and *Ordered-subset Expectation Maximization* (OSEM).

FBP Reconstruction

Reconstruction was performed with a Butterworth filter. Its cut-off frequency was visually inspected on a range from 0.30 to 0.80 pixels^{-1} with step 0.2. Selected parameters were order 4 and cut-off frequency of 0.66 pixels^{-1}.

OSEM Reconstruction

Reconstruction was carried out using 4 subsets and 20 iterations. It also applied a quadratic penalty function using the 4 nearest neighbors of each pixel within a plane, along with the pixels adjacent to it on the slices above and below, as suggested by Fessler [94].

3.4.4 Postprocessing

Following reconstruction, images were automatically masked for truncation artifact removal. Subsequently, they were scaled to a 100 grey level window, setting negative values to zero. Finally, they were saved in DICOM format in order to be processed by our 3D-ASM algorithm as a regular patient.

3.4.5 3D-ASM Segmentation

Automatic segmentation of LV cavity was performed by means of 3D-ASM (see Section 5.2). Implementation details are provided next.

ASM Parameters

A uni-ventricular model of 2677 points (1835 for endocardium and 842 for epicardium) was used. The algorithm was set to run for 15 iterations or until the change in LV volume was not substantial between iterations ($\Delta Volume <$ 0.01ml). New model instances were generated with 75% of the total shape variability. This constrain was imposed to obtain a smooth fit to match the sparse

(a)   *(b)*   *(c)*

(d)   *(e)*   *(f)*
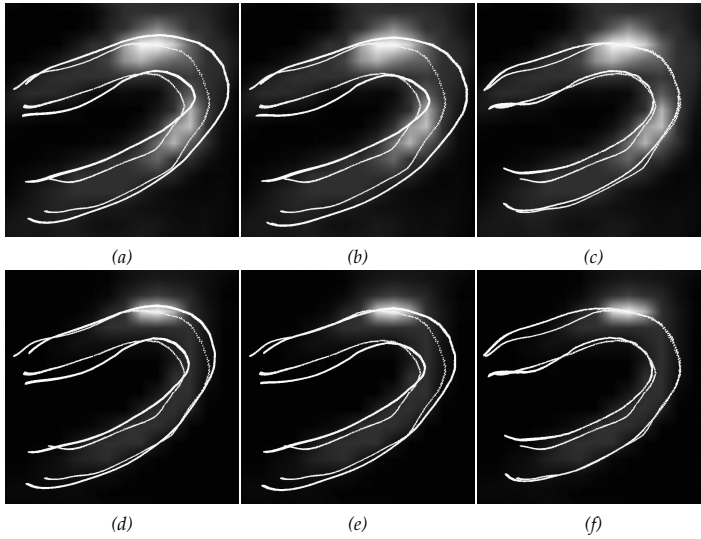
Figure 3.5: *Axial view of a virtual study for FBP (a-c) and OSEM (d-f) reconstructed images. Edges obtained automatically by 3D-ASM with ST (a,d), GR (b,e), FBP (c) and OSEM (f) boundary models are shown in white (thick). True edges are displayed on yellow (thin). ST= step function; GR= maximum gradient; FBP= Filtered Back-projection; OSEM= Ordered-subset Expectation Maximization. (See color insert)*

(a)   *(b)*   *(c)*

(d)   *(e)*   *(f)*
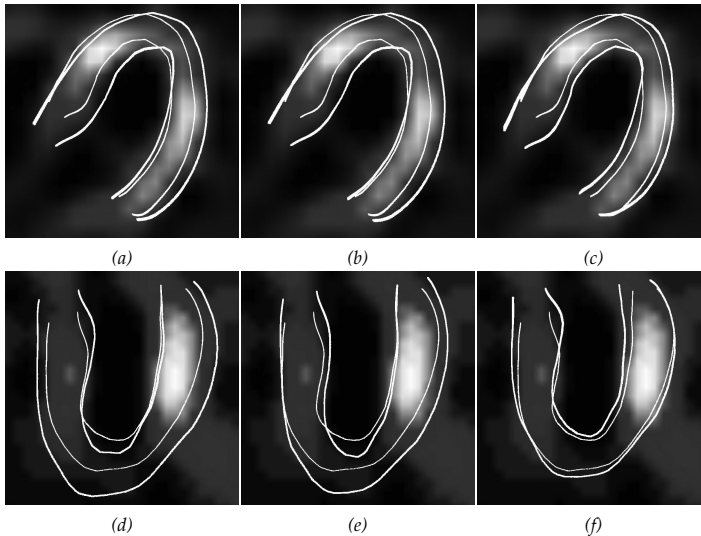
Figure 3.6: *Two clinical cases with severe perfusion defects: case one in axial view (a-c) and case two in long-axis view (d-f). Edges obtained automatically by 3D-ASM with ST (a,d), GR (b,e) and FBP (c,f) boundary models are shown in white (thick). True edges are displayed on yellow (thin). Abbreviations as in Fig. 3.5. (See color insert)*

TABLE 3.4: Parameters used for 3D-ASM Segmentation

Description	Symbol	Value
Allowed Mode Variation	β	$\pm 2\sigma$
Number of Nodes	m	2677
Profile Length	*n.a.*	7
Profile Sampling Interval	*n.a.*	3mm
Shape Variability	*n.a.*	75%
Gaussian Kernel Width	σ_p	7
Maximum Iterations	*n.a.*	15

data obtained from SPECT imaging, as apposed to CT imaging which allows for finer details. Other ASM parameters are summarized in Table 5.1.

Dynamic Studies Segmentation

Cardiac dynamics add to our segmentation process yet another challenge: intensity profile variation per cardiac phase. The most intuitive scheme to approach this matter would be to obtain a model trained for each cardiac frame.

An alternative strategy is to perform ASM fusion [95], which has proven to be an effective technique for intensity model generation [96]. Under this methodology, only End Diastolic (ED) and End Systolic (ES) models were generated, since they represent the two most extreme circumstances on cardiac dynamics. Missing phases were obtained through a weighted fusion of ED and ES models. Weights used for each cardiac phase were set by the current heart phase index (LV contraction percentage) as logged by NCAT [63].

Model Initialization

We followed a very simple mechanism to roughly scale and position the mean shape of the model. The operator defines two epicardial points at the basal level and a third one at the apex. Corresponding anatomical landmarks of the mean shape were previously tagged by an experienced investigator. Consequently, the mean shape is aligned to the landmarks through a similarity transform. The manual interaction required for this procedure lasts about 30 seconds. In complex cases (i.e. large perfusion defects) longer interaction may be required, up to 1.5 minutes, for a correct depiction of basal and apical planes.

For the virtual population, initialization points were extracted automatically from the true shapes, thus eliminating initialization bias for a better analysis of segmentation accuracy. The clinical database, instead, was initialized by an experienced investigator, hereafter referred to as *Obs1*.

Functional Analysis

Once the shape model is correctly matched to specific image data, LV volumes both in End Diastole (EDV) and End Systole (ESV) can be calculated. Ejection Fraction (EF) can be derived from these measurements in order to evaluate systolic function of a patient.

3.5   Experimental Evaluation

3.5.1   Segmentation Accuracy

- *Idealized vs. simulated boundary model:* to evaluate the advantage of using advanced simulations during training, a comparison with two idealized boundary models was performed. The first model consisted of a step function (ST), ranging from zero to one corresponding to a normalized intensity profile. The second model located the boundary at the maximum gradient (GR) of a sampled profile, as initially proposed by Cootes *et al.* [51]. Both virtual and clinical populations were segmented with these models.

- *True vs. fitted geometry:* unsigned point-to-surface (P2S) errors were computed between the fitted meshes obtained with idealized and simulated boundary models and the gold standard LV surfaces. Mean± standard deviation (SD) values of all subjects in all temporal phases were computed.

- *Trained-tested analysis:* to examine the influence of using the same reconstruction method both in training and segmentation stages, we performed an experiment combining trained-tested models. That is, a model trained with FBP reconstructed datasets was tested on an OSEM reconstructed dataset during segmentation, and vice versa. A *Mann-Whitney U-test* [97], with a 95% confidence interval, was carried out to determine statistical significance of the differences.

- *Clinical dataset:* location of LV borders in SPECT datasets is quite subjective due to the blurred nature of these images (see Fig. 3.1). However, to generate a proper gold standard for accuracy evaluation, LV contours were manually drawn according to a standard criterion: LV borders should be located at 40% of the maximum myocardial intensity. This value was obtained based on reported studies [98] and our clinical experience. In case of extensive perfusion defects, the human observer could modify the threshold down to 20%. Endocardial and epicardial border delineation of the LV, at ED, was performed by two observers (*Obs1, Obs2*) in two individual sessions (*S1, S2*). The resulting traces were used to: *1)* evaluate intra and inter-observer variability, and *2)* obtain P2S errors of automatically segmented surfaces.

3.5.2   Sensitivity to Initialization

To evaluate the influence of initialization on our segmentation approach, the fitting process was performed 10 times for each virtual subject. Each set of initialization points was generated by adding a random error to the true landmarks of up to 6.25mm (voxel size) along the X, Y and Z axis. P2S errors between true LV surfaces and the 10 fitted meshes with initialization error were computed. Also, volume errors were measured as the absolute difference between true volumes and calculated volumes.

3.5.3 LV Function Calculations

- *True vs. measured volume:* for the virtual population, volume error was measured with respect to true LV volumes at ED and ES. For the clinical population, gold standard volumes were obtained from manually traced LV contours on the paired MRI datasets. Agreement of measurements with gold standard values was assessed by means of Bland-Altman (B&A) plots [99]. Accuracy error was calculated as the percentage of absolute volume difference (*diff(True,Measured)*) relative to true volume.

- *Clinical tool:* for the clinical dataset, a comparison with the most widespread clinical analysis tool, Quantitative Gated SPECT (QGS), was made. Results were analyzed taking into account previously published studies which describe QGS performance (see Table 5.5).

- *Population subgroups:* in order to analyze the effect of perfusion defects on 3D-ASM volume calculations, we separated our clinical population into three subgroups. Categorization was performed by an expert clinician, *Obs2*, according to severity of the perfusion defect: *1)* none, *2)* mild to moderate, and *3)* severe.

3.6 Results

3.6.1 Quantitative

Segmentation Accuracy

Fig. 3.5 shows LV edges obtained with 3D-ASM for the ST, GR, FBP and OSEM boundary models. Fig. 3.6 displays two clinical cases with severe perfusion defects. LV edges obtained with 3D-ASM for all boundary models are displayed as well. Corresponding true surfaces are included on both figures.

Table 3.5 shows the results for the trained-tested analysis and the idealized vs. simulated boundary model analysis. The P2S errors of the segmentations performed with the idealized models are noticeably larger than the ones of the simulated boundary models. Endocardial errors were 28% larger than those of the FBP model and 20% larger than those of the OSEM model. Epicardial errors were 89% larger than those of the FBP model and 66% larger than those of the the OSEM model.

Sub-voxel accuracy was obtained with our segmentation method for both reconstruction techniques (See Table 3.5). For FBP reconstructed datasets, epicardial borders were segmented 35% more accurately than endocardial ones, while in OSEM reconstructed datasets the difference was 38%.

Fig. 3.7 displays the statistical significance evaluation of the trained-tested analysis. All compared groups generated significantly different P2S errors, except for endocardial errors of FBP-FBP vs. OSEM-FBP and ST-FBP vs. GR-FBP, and epicardial errors of ST-OSEM vs. GR-OSEM.

Fig. 3.8 displays P2S errors for each cardiac phase, with ED being $t = 1$ and ES being $t = 5$. Endocardial errors obtained at ED were 21% larger with respect to ES for both FBP and OSEM reconstructed datasets. On the other

TABLE 3.5: Point-to-surface errors for the virtual population

			Endocardium		Epicardium	
			mean	SD	mean	SD
	Trained	Tested	*mm*	*mm*	*mm*	*mm*
Idealized	ST	FBP	4.57	0.24	4.33	0.23
		OSEM	4.35	0.25	3.67	0.24
	GR	FBP	4.57	0.22	4.49	0.20
		OSEM	4.27	0.24	3.67	0.22
Simulated	FBP	FBP	3.56	0.27	2.33	0.22
		OSEM	3.70	0.29	3.00	0.29
	OSEM	FBP	3.61	0.26	2.69	0.14
		OSEM	3.57	0.27	2.21	0.17

SD= standard deviation; Abbreviations as in Fig. 3.5.
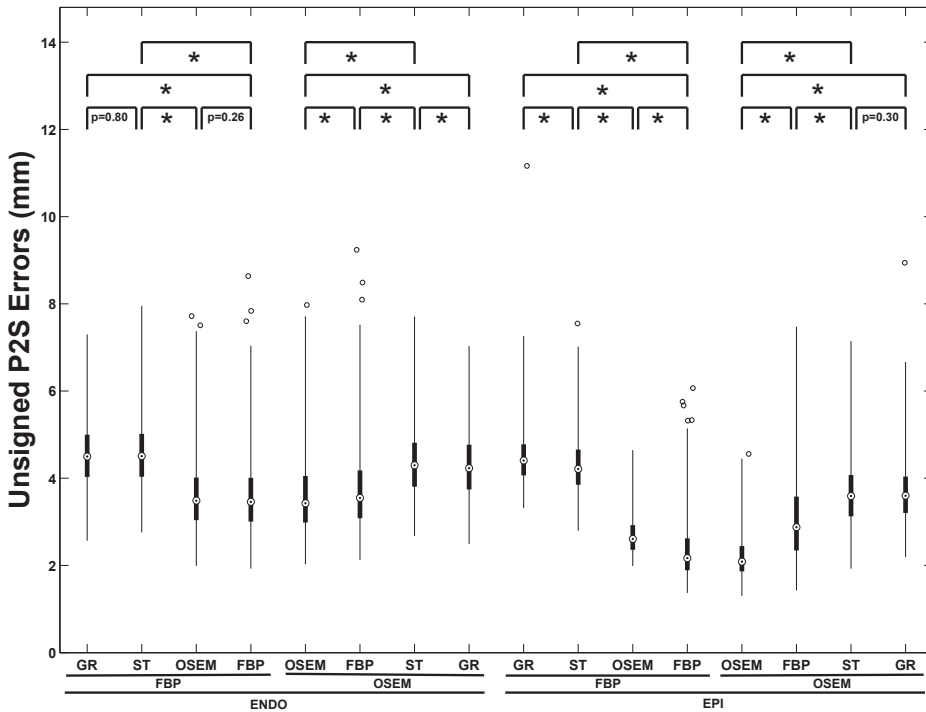
Figure 3.7: *Box-and-whisker plot of the trained-tested analysis for FBP, OSEM, ST and GR boundary models. Connecting lines illustrate compared groups. The stars represent statistically significant differences. p values of the statistically nonsignificant differences are also displayed. Abbreviations as in Fig. 3.5.*

hand, epicardial errors were 18% smaller at ED for FBP reconstructed datasets and only 3% lower for OSEM reconstructed datasets.

Fig. 3.9 shows P2S errors for each of the 17 LV AHA's segments [87]. For the FBP reconstructed datasets, errors corresponding to the basal plane were 43% larger than those of the medial plane and 56% larger than those of the apical
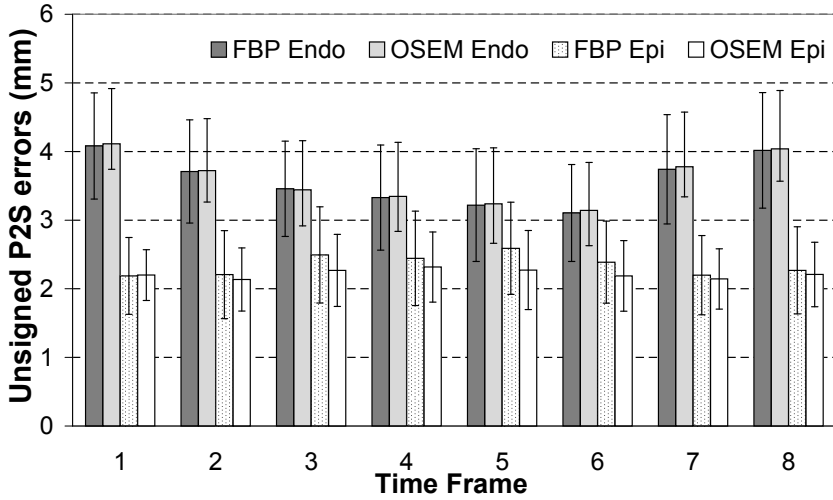
Figure 3.8: *Bar plot of mean point-to-surface errors per cardiac phase for FBP and OSEM reconstructed datasets. ED corresponds to t = 1 and ES to t = 5. Error bars represent standard deviation of the measurements. Endo= Endocardium; Epi= Epicardium; Abbreviations as in Fig. 3.5.*
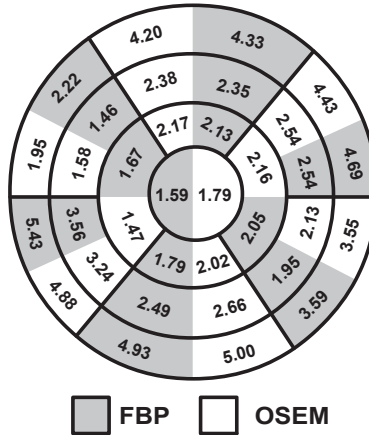
Figure 3.9: *Bull's eye plot of point-to-surface errors for each of the 17 left ventricular AHA's segments for FBP and OSEM reconstructed datasets. Abbreviations as in Fig. 3.5.*

plane. For the OSEM reconstructed datasets, the same comparison generated a 39% and 52% difference, respectively.

For the clinical population, intra and inter-observer variabilities are summarized in Table 3.6. P2S errors between 3D-ASM fitted shapes and manual delineations are also displayed. For endocardial errors, intra- and inter-observer variabilities were not significantly different than those obtained automatically with the FBP and ST boundary models. The GR boundary model, instead, gen-

TABLE 3.6: Point-to-surface errors for the clinical population

		Endocardium		Epicardium	
		mean	SD	mean	SD
	Variability	*mm*	*mm*	*mm*	*mm*
Manual	Intra-observer	4.52	0.96	3.15	0.57
	Inter-observer	4.70	1.01	3.45	0.77
3D-ASM	FBP	4.69	0.78	4.15	0.75
	ST	5.11	0.93	6.16	1.52
	GR	5.26	0.98	4.88	1.20

SD= standard deviation; Abbreviations as in Fig. 3.5.

TABLE 3.7: Sensitivity to initialization

		Point-to-surface error		LV Function		
		Endocardium	Epicardium	EDV	ESV	EF
Dataset	Measure	*mm*	*mm*	*ml*	*ml*	*%*
FBP	mean	3.73	2.54	3.65	3.29	4.79
	SD	0.28	0.25	1.23	1.12	1.16
	max	21.1	21.9	73.9	40.7	24.6
	min	0.25	0.66	0.01	0.00	0.01
OSEM	mean	3.74	2.40	3.85	3.17	4.70
	SD	0.28	0.20	1.22	1.18	1.2
	max	17.90	9.43	52.9	45.8	26.9
	min	0.29	0.31	0.01	0.00	0.00

SD= standard deviation; EDV= End diastolic volume; ESV= End systolic volume;
EF= Ejection fraction; Other abbreviations as in Fig. 3.5.

erated significantly higher P2S errors than intra-observer variability. They were also significantly higher than those of the FBP boundary model. Epicardial errors, on the other hand, were found to be significantly different for all schemes.

Sensitivity to Initialization

Table 3.7 shows the results regarding initialization sensitivity for FBP and OSEM reconstructed datasets. For both of them, the added inaccuracy caused by initialization error was 5% for endocardial borders and 8% for epicardial ones. Volume calculations presented an average error of 3.5ml affecting the EF measurements in 4.7%. However, maximum errors came to be as large as 22mm for accuracy measurements and 74ml for volume calculations.

LV Function Analysis

Fig. 3.10 displays B&A plots of volume calculations for the virtual population. FBP reconstructed datasets produced EDV measurements with a 94.4% accuracy, ESV measurements with a 90.0% accuracy and EF measurements with a 90.8% accuracy. For the OSEM reconstructed datasets, accuracy calculations

3D-ASM on FBP reconstructed datasets

(a)   *(b)*   *(c)*

3D-ASM on OSEM reconstructed datasets

(d)   *(e)*   *(f)*

Figure 3.10: Virtual population: *Bland-Altman plots for EDV (a,d), ESV (b,e) and EF (c,f) comparing gold standard and measured values estimated with 3D-ASM for the datasets reconstructed by means of FBP (top) and OSEM (bottom). Abbreviations as in Table 3.7.*

Figure 3.11: *Plot of Ejection Fraction (EF) error vs End Diastolic (ED) volume for FBP (o) and OSEM (*) reconstructed datasets of the virtual population. Abbreviations as in Fig. 3.5.*

3D-ASM ON CLINICAL DATASET

(a)   (b)   (c)

QGS ON CLINICAL DATASET

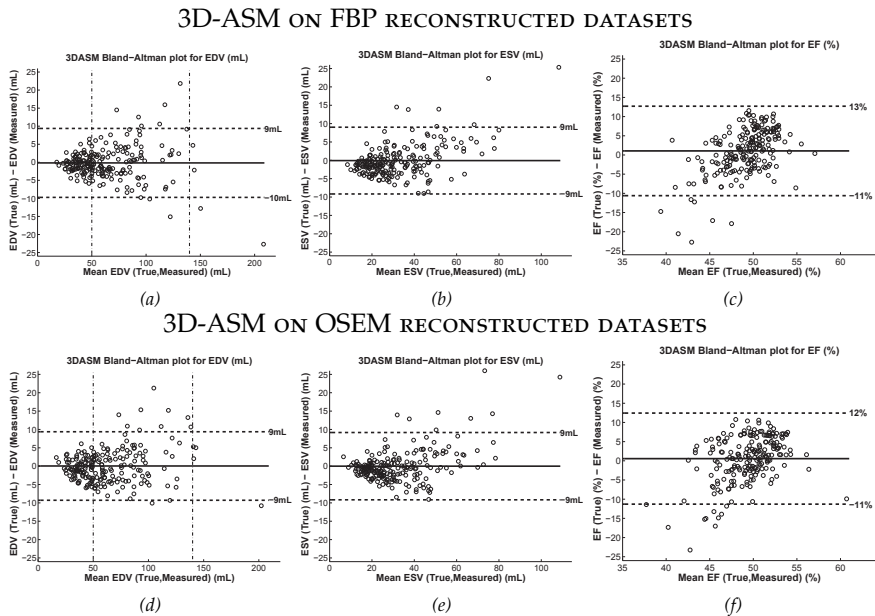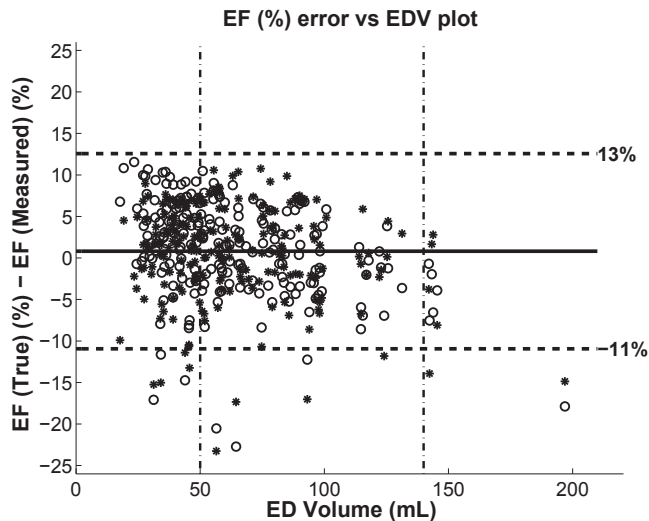(d)   (e)   (f)
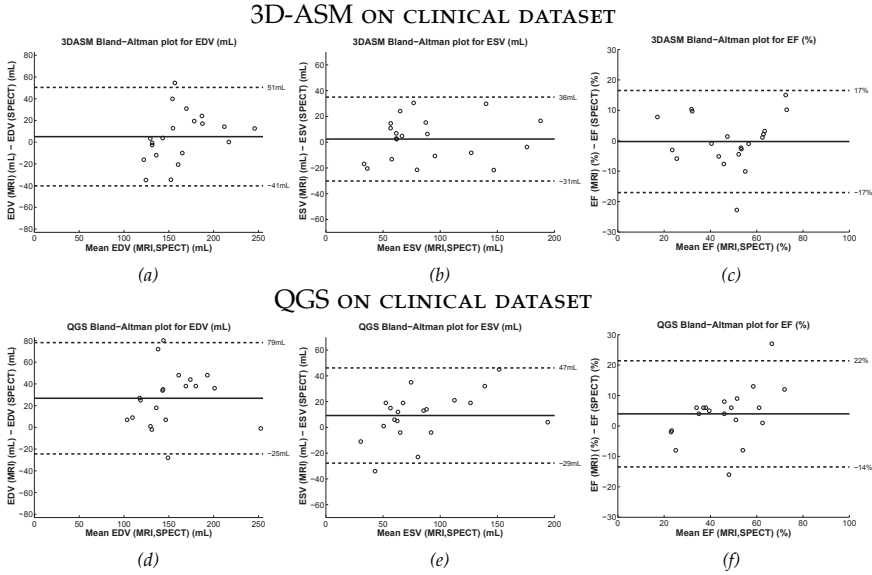
Figure 3.12: Clinical population: *Bland-Altman plots for EDV (a,d), ESV (b,e) and EF (c,f) comparing gold standard and measured values estimated with 3D-ASM (top) and QGS (bottom). QGS= Quantitative Gated SPECT software; Other abbreviations as in Table 3.7.*

were: 94.5% for EDV, 90.2% for ESV, and 90.9% for EF. A further analysis of EF error relative to EDV is presented in Fig. 3.11.

For the clinical population, B&A plots are displayed in Fig. 3.12. 3D-ASM obtained accuracy levels of 89.5% for EDV, 87.0% for ESV, and 88.1% for EF. QGS measurements obtained accuracy levels of 81.7% for EDV, 83.5% for ESV, and 83.9% for EF. In concrete, the B&A plots for EF calculated with 3D-ASM displayed no bias and smaller variance than those of QGS.

Fig. 3.13 displays accuracy errors for the clinical population subgroups. Errors showed no obvious correlation to severity of perfusion defect. Only ESV of the *none* subgroup shows a high inaccuracy for both postprocessing algorithms. It must be noted that half the patients in this group (n_{total}=4) presented hypertrophic LVs with collapsing walls at ES, hence the larger errors in ESV calculations.

3.6.2   Critical Analysis

Segmentation Accuracy

Idealized models demonstrated not to be robust enough for the segmentation task evaluated during this work. Fig. 3.14 illustrates this fact by displaying a bar plot of the gradient profile averaged over all landmarks and all datasets of each population (i.e. $n_{virtual} = 208$ and $n_{clinical} = 20$). Position zero in the horizontal axis indicates the location of the boundary. Due to the absence of OSEM clinical datasets, only the FBP datasets are presented. Comparisons were performed
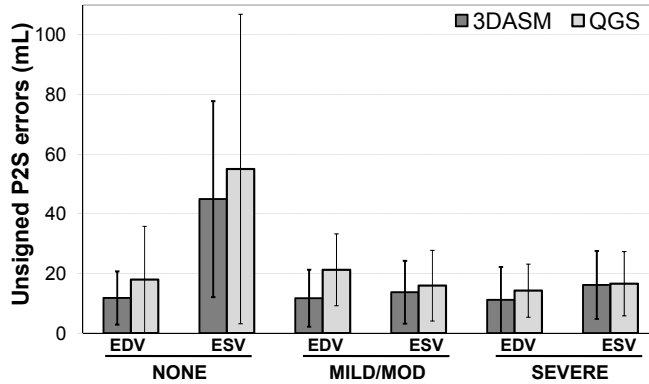
Figure 3.13: *Accuracy errors on volume calculations for the three population subgroups according to perfusion defect severity. EDV and ESV errors for 3D-ASM and QGS. Error bars represent standard deviation. Abbreviations as in Fig. 3.12.*
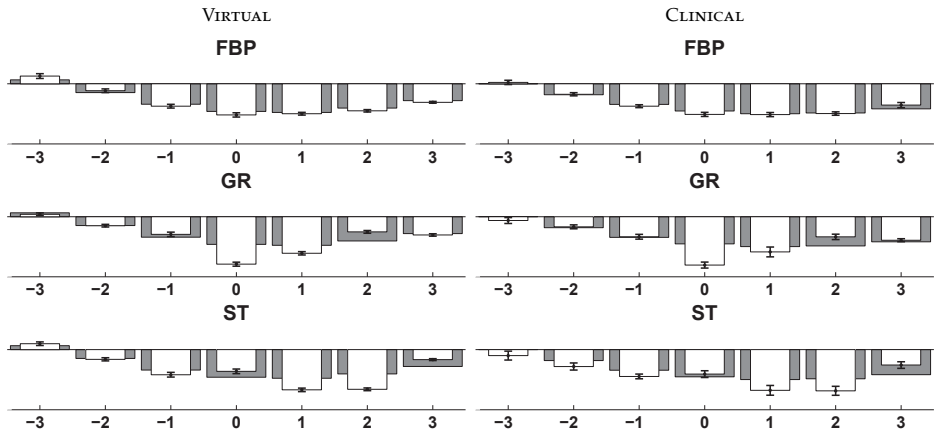
Figure 3.14: *Bar plot comparing the underlying gold standard and the best-fit profiles using the three boundary models in both virtual (left) and clinical (right) populations. Plots show the gradient profiles with respect to the gold standard boundary position (zero abscissa). Dark and light bars stand for the mean gold standard gradient profile (around and along the normal to expert surfaces) and the best-fit gradient profiles (around and along the normal to candidate surfaces based on FBP, GR and ST boundary models), respectively. Error needles on the light bars represent the SD of the difference between the gold standard and model gradient profiles. Means and SDs were computed over all landmarks and all datasets for both populations. Experiments show that the higher accuracy achieved with our proposed technique is consistent with a more accurate modeling of gradient profiles. Abbreviations as in Fig. 3.5*

against the corresponding gold standard which is represented with dark bars. Light bars represent the profile with respect to the best-fit boundary position according to the FBP, GR and ST boundary models. It is interesting to observe

that in all cases (virtual and clinical datasets) the actual best-fit profiles are more alike to the simulated profiles than to the idealized profiles. This is achieved in spite of the limitations of a simulated training set, which may not capture all the details of an actual clinical database. Similarly, the standard deviation of the difference between the gold standard and the simulated boundary models were smaller than those of the two idealized boundary models. In practical terms, it reduced P2S segmentation errors by at least 20% for endocardial borders and 66% for epicardial borders.

The trained-tested analysis showed that more accurate segmentation results are obtained when the same reconstruction method is used both in training and segmentation stages. Despite the fact that OSEM reconstruction allows for better definition of LV structures, endocardial borders are located with errors of the same magnitude as those obtained with FBP. We suspect that a substantial increase in image resolution is necessary before the apparent visual improvement of OSEM reconstructed datasets has a real impact on global quantitative parameters.

Overall decreased accuracy found on endocardial border segmentation is reasonable as the relative image resolution is lower for the inner surface of the LV. That is, the correct position of a large contour (epicardium) can be found more precisely than the position of a smaller contour (endocardium), given the same pixel size.

Greater P2S errors found at basal level are quite understandable since a correct depiction of LV basal plane is a well known complication of cardiac imaging postprocessing for most modalities [100]. SPECT images are specially challenging on this matter owing to the lack of commonly used anatomical landmarks such as the mitral valve or the left atria.

As can be observed in Fig. 3.9, P2S errors are larger at the inferoseptal basal segment. Because of the presence of the membranous septum, this region displays almost no tracer activity. Hence, during fitting the mesh is not actively deformed at this area the LV wall. This is represented in the virtual phantoms as thinner septal structures. It is particularly noticeable at ED where the difference in activity between the basal portion of the lateral wall and the basal portion of the septal wall is quite visible. At ES, though, due to thickening and shortening of the LV walls, the septum can be better defined at basal levels.

For the cardiac phase analysis, the larger epicardial P2S errors found at ES phase are natural (lower resolution and partial volume effect). However, the decrease in error observed for endocardial borders is counterintuitive. Visual inspection suggests this is caused by the higher segmentation inaccuracy at basal level, as mentioned above.

For the clinical studies, 3D-ASM errors for endocardial borders are comparable to inter-observer variability. However, epicardial boundaries presented 20% larger errors than inter-observer variability. This might be due to overestimation of wall thickness in places of extensive perfusion defects. Regardless of lack of data, a human observer may deduct a thinning of the LV walls caused by chronic infarcted myocardium. ASM, on the other hand, will try to conserve the wall thickness present on the remaining sampled data. It must noted that intra and inter-observer variability under uncontrolled circumstances (i.e. without a standardized criterion) will most likely be larger than the ones measured

during our experiments.

Sensitivity to Initialization

The evaluation of initialization sensitivity illustrated the extent of inaccuracy caused by initialization error. Yet, in average, this inaccuracy was rather small. The maximum errors revealed noticeable bias in case of very improper initialization points. However, in clinical dataset processing, initialization would be performed by a trained technician capable of efficiently and correctly defining basal and apical positions.

LV Function Analysis

For the virtual population, the scatter distribution of the B&A plots showed a dependency of the error on the LV volume. B&A plots also revealed that our algorithm tends to underestimate EDV, a tendency also present on QGS (See Table 5.5). The most extreme case of overestimation was found for the largest heart. Yet its difference is within reported limits of discrepancy (30ml from gold standard measurements) [108].

For ESV, a slight overestimation is revealed through the B&A plots, previously stated for QGS as well (Table 5.5). For EF, the confidence intervals in the B&A plots are wider than those for EDV and ESV, probably caused by the higher dispersion observed on lower EF values. Note in Fig. 3.11 that many of the large discrepancies in EF calculations are located around small hearts (50ml EDV). This parameter is known to be overestimated for this type of hearts when calculated from perfusion studies [109]. This is attributed to artificially increased counts in the LV cavity, complicating a proper calculation of ESV volumes.

For the clinical population, overall patterns of B&A plots were comparable to those of QGS. Calculated parameters showed less biased underestimations. Smaller confidence intervals were found for 3D-ASM for all calculated parameters. Similarly, accuracy levels were higher than those obtained with QGS for all measured parameters.

No obvious correlation between perfusion defect severity and segmentation inaccuracy was found for our clinical database. Inaccuracy could be more related to low image quality or segmentation difficulty depending on pathology. For instance, the group with no perfusion defects was composed of hypertrophic patients and one dilated patient with Left Bundle Branch Block, both difficult cases to segment even for a human observer.

3.7   Discussion

3.7.1   Clinical Contributions

Our method obtained higher accuracy compared to QGS, one of the most widespread commercial packages. Although this result is obtained in a small population, this is quite encouraging for a simulation based approach since it by-

TABLE 3.8: META ANALYSIS OF PUBLISHED WORKS COMPARING QGS POSTPROCESSING RESULTS AGAINST A GOLD STANDARD.

Author	Year	n (Fem/Male)	Population	Gold Standard	Postprocessing Software						Small Hearts	
					QGS			Gold Standard			QGS	
					EDV *ml*	ESV *ml*	EF %	EDV *ml*	ESV *ml*	EF %	EDV ⇑ / ⇓	EF
Achtert *et al.* [83]	1998	3 (*n.a.*)	Normal	MCAT	111.0	42.5	61.9	121.8	50.0	59	⇓	⇑
Tadamura *et al.* [101]	1999	16 (3/13)	Surgery	MRI	106.1	54.9	47.9	112.1	55.3	50.8	*n.a.*	*n.a.*
Bavelaar-Croon *et al.* [102]	2000	21 (7/14)	CAD	MRI	151.0	97.0	43.0	191.0	114.0	45.0	*n.a.*	*n.a.*
Nakajima *et al.* [103]	2001	4 (*n.a.*)	Normal	Phantom	123.0	*n.a.*	*n.a.*	131.0	*n.a.*	*n.a.*	⇓	⇑
Nakajima *et al.* [103]	2001	30 (10/20)	Mixed	GBP	98.0	*n.a.*	54.0	103.0	*n.a.*	49.0	⇓	⇑
Lipke *et al.* [104]	2004	54 (15/39)	CAD	MRI	122.0	62.0	52.2	139.0	60.0	60.0	*n.a.*	*n.a.*
Lomsky *et al.* [105]	2005	5 (*n.a.*)	Normal	NCAT	113.0	64.0	45.6	115.2	44.8	61.0	⇓	⇑
Schaefer *et al.* [106]	2005	70 (16/54)	CAD	MRI	120.0	60.0	53.2	137.0	57.0	60.6	*n.a.*	*n.a.*
Stegger *et al.* [82]	2007	70 (16/54)	CAD	MRI	120.0	60.0	53.0	137.0	57.0	61.0	⇓	⇑
Wu *et al.* [107]	2007	33 (*n.a.*)	CAD	MRI	*n.a.*	*n.a.*	40.2	*n.a.*	*n.a.*	40.1	*n.a.*	*n.a.*

n.a. = Not available; Normal= Healthy hearts; Surgery= Coronary artery bypass surgery; CAD= Coronary arterial disease;

Mixed= Common cardiomyopathies; MCAT= 3D dynamic cardiac-torso phantom; MRI= Magnetic resonance imaging;

Phatom=Cylindrical mathematical model; GBP= Gated blood-pool study; NCAT= 4D NURBS-based cardiac-torso phantom;

⇓ = Underestimation; ⇑ = Overestimation; EDV= End diastolic volume; ESV= End systolic volume;

EF= Ejection fraction; QGS= Quantitative Gated SPECT software.

passes the labor of clinical database collection and, furthermore, the underlying methodology is potentially applicable to other modalities.

The employed segmentation method could either be applied on transaxial slices or on reformatted short axis images. The use of the transaxial slices is preferable since time consuming operator assistance is required to define the LV long axis.

As can be concluded from previous works (see Table 5.5) the tendencies of QGS for small hearts still needs further review. Virtual populations with specific heart sizes may be useful for investigating this matter.

3.7.2   Outlook

The feasibility of our approach has been illustrated in the context of one clinical application (viz. cardiac image analysis) and one specific imaging modality (viz. gSPECT). Nevertheless, the potential of this approach is much broader.

To start off, it can help decoupling the sample size requirements of building relevant statistics for the intensity models. Shape models could be built based on a high-resolution imaging modality (e.g. CT) and the derived PDM be sampled to generate a virtual population from which simulated images of other modalities can be produced (e.g. MR, SPECT or US). Regarding sample size, only few real clinical images might be available for extreme anatomical variants (e.g. very small or very large hearts). However, they can be sampled uniformly when creating the virtual population for simulated data.

Another problem in learning intensity models directly from real images is related to the rapid evolution of most imaging technologies. Handling this problem would become simpler with our technique as we can regenerate the intensity models, as long as the employed simulator allows for it. The upgrades can be related to: *1)* improvement of spatial resolution (i.e. smaller pixel size), *2)* increase of temporal resolution (i.e. more frames per cycle), *3)* development of better reconstruction techniques (e.g. iterative algorithms), *4)* isotropic voxels (i.e. for MRI or CT), *5)* variation on physical parameters used during acquisition (e.g. modification of MRI sequences), etc.

As the final advantage, we would like to mention that avoiding the need to use shapes derived from manually contoured shapes prevents expert dependency as the true boundary information is known by construction. Moreover, the possibility to build intensity models in every major modality based on a high-resolution PDM pave the way for handling more consistently multimodal datasets.

This approach, however, may present a number of disadvantages, depending on the realism and accuracy of the image acquisition simulator, such as: computationally expensive processing, large amount of input parameters sometimes hard to determine, use of theoretical noise which may not resemble clinical conditions, etc.

3.8   Conclusion

This paper introduced the notion of using advanced imaging simulators to enable automatic creation of intensity models. Results show that gSPECT studies can be successfully segmented by models trained under this scheme with sub-voxel accuracy. The accuracy in estimated LV function parameters range from 90.0% to 94.5% for the virtual population and from 87.0% to 89.5% for the clinical population. These results are within the intervals reported by other widespread clinical segmentation tools.

Our future efforts along the generic approach we presented here is to extend this technique to other imaging modalities. Efforts are underway to apply this approach to 3D US data [49] and we do not foresee fundamental issues not to extend this technique to MRI and CT.

4

Realistic Simulation of Cardiac Magnetic Resonance Studies Modeling Anatomical Variability, Trabeculae and Papillary Muscles

Catalina Tobon-Gomez, Federico M. Sukno, Bart H. Bijnens,

Marina Huguet and Alejandro F. Frangi

Abstract

Simulated magnetic resonance imaging brain studies have been generated for over a decade. Despite their useful potential, simulated cardiac studies are only emerging. This paper focuses on the realistic simulation of cardiac MRI datasets. The methodology is based on the XCAT phantom, which is modified to increase realism of the simulated images. Modifications include the modeling of trabeculae and papillary muscles based on clinical measurements and published data. To develop and evaluate our approach, the clinical database included 40 patients for anatomical measurements, 10 patients for papillary muscle modeling, and 10 patients for local grey value statistics. The virtual database consisted of 40 digital voxel phantoms. Histograms from different tissues were obtained from the real datasets and compared to histograms of the simulated datasets with the Chi-square dissimilarity metric (χ^2) and Kullback-Leibler divergence (KL). For the original phantom, χ^2 values averaged 0.65±0.06 and KL values averaged 0.69±0.38. For the modified phantom, χ^2 values averaged 0.34±0.12 and KL values averaged 0.32±0.15. The proposed approach demonstrated a noticeable improvement of the local appearance of the simulated images with respect to the ones obtained originally.

4.1   Introduction

Cardiac structural and functional assessment in the clinical environment is still largely dependent on manual postprocessing [110]. Certainly, efficient and accurate tools to perform cardiac function evaluation are highly desirable. This is the goal of many automated algorithms under development. Simulated image datasets are an interesting way to help implement and validate such algorithms. They bring along several advantages: access to a ground truth without expert dependency, the possibility to generate large databases, the capability to update training sets to account for the evolution of imaging devices, and the feasibility to generate a multimodal dataset with the available image simulators [65, 72, 73, 111].

Simulated magnetic resonance imaging (MRI) brain studies have been generated for over a decade [72, 112]. Despite their useful potential, simulated cardiac studies are only emerging [113–115]. This is mainly due to the lack of an appropriate phantom for MRI cardiac simulations. Current digital phantoms suitable for cardiac applications mainly focus on low contrast imaging modalities (i.e. nuclear medicine) where a macroscopic representation of the tissues is sufficient. However, a modality like MRI, mainly characterized by high tissue contrast and improved spatial resolution, requires greater detail to fully represent a real acquisition.

Which brings us to the focus of this paper: realistic simulation of cardiac MRI datasets. Our methodology is based on the XCAT phantom [73, 116], which is modified to increase realism of the simulated datasets to capture features that are important for the development and evaluation of image processing algorithms. The modifications include: *1)* modeling of the left ventricular papillary muscles, *2)* inclusion of trabeculae in both ventricular cavities, *3)* addition

of intensity variability of each tissue by increasing the number of labels of the phantom, and *4)* resemblance of partial volume effect by using a higher resolution phantom as input to the simulator.

4.2 Materials and Methods

4.2.1 Patients

Clinical datasets were used for two main purposes: extracting the anatomical modeling parameters and validating the simulated images. Our database consisted of cardiac MRI studies of 60 patients, which can be divided into three groups:

- *G1:* composed of axial slices of 40 patients (20 females). This group consisted of healthy subjects and was used to characterize anatomical variability. Measurements included long-axis/short-axis of the torso, long-axis/short-axis of the ribcage, long-axis/short-axis of the breasts and angle between the breasts.

- *G2:* composed of short-axis stacks of 10 patients (5 females). Patients with any sign of hypertrophy and/or deposition diseases were excluded. This group was used to model papillary muscle variability. Measurements included thickness, angle from the center of the cavity and distance to the wall. Fig. 4.1 displays a scheme of the obtained measurements. Angle and distance were measured at papillary muscle initial point (midventricular level) and final point (apical level).

- *G3:* composed of short-axis stacks of 10 patients (5 females). This group consisted of healthy subjects, with no history of heart disease, and was used to obtain a gold standard of local appearance for each evaluated tissue.

4.2.2 MR Imaging

Datasets were acquired using a General Electric Signa CVi-HDx, 1.5T scanner (General Electric, Milwaukee, USA). All images were acquired during breathholds of approximately 15 seconds and were gated to the vector ECG. Images were scanned with a multi-slice 2D balanced Steady State Free Precession (SSFP) sequence. Both axial and short-axis datasets were acquired with the following scan parameters: TR/TE= 2.9/1.2ms, flip angle= 45°, pixel spacing= 1.56×1.56mm, slice thickness= 8mm slice separation= 0mm, field of view= 400×340mm, number of signal averages= 1, scan matrix size= 224×224, cardiac phases= 30.

4.2.3 MR Simulation

The MRI simulation code used in this work was developed by Kwan *et al.* [72]. This code uses a *tissue template* to define the spatial distribution. A tissue template is an anatomical image where each tissue is a mask with a certain value
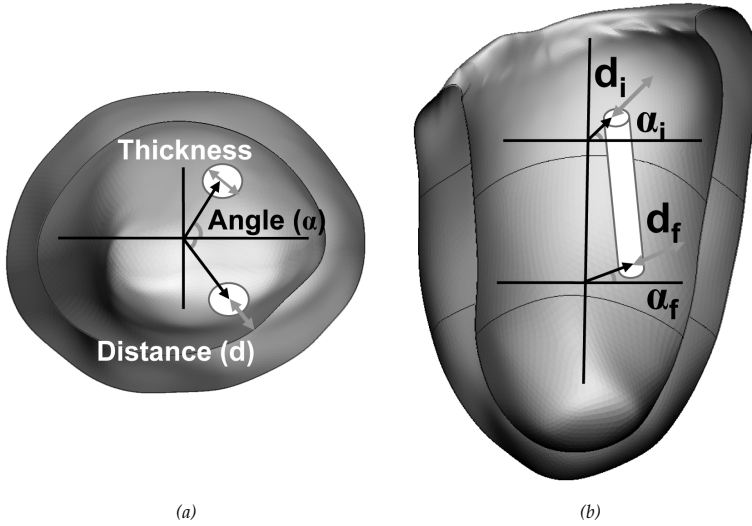
Figure 4.1: *(a) Clinical measurements for papillary muscle modeling: thickness, distance from wall (d) and angle from center of the cavity (α). (b) Long axis view of a left ventricle to illustrate papillary direction assignment: initial angle ($α_i$), initial distance (d_i), final angle ($α_f$) and final distance (d_f). Arrows=distance; Arcs=angles.*

(i.e. a labeled image). A stack of these templates forms a 3D volume used as input for the simulator. A *parameter file* contains characteristic magnetic resonance properties for each tissue label. Specific *scan parameters* define the output images of the simulator. The code models the physical phenomena by solving the Bloch equations [117]. Finally, the images may include acquisition artifacts, such as noise, partial volume effect, chemical shift, etc.

Sequence parameters for the simulation were: TR/TE= 2.9/1.2ms, flip angle= 45°, pixel spacing= 1.56×1.56mm, slice thickness= 7.8mm, slice separation= 0mm, field of view= 400×400mm, number of signal averages= 1, scan matrix size= 256×256. No field inhomogeneities were simulated. Noise settings included: water-fat shift= 2 pixels and Gaussian noise with standard deviation calculated as $0.03 \times intensity\,(reference\,tissue)$.

4.2.4 Digital Voxel Phantoms

Original Phantom

Virtual subjects were generated with XCAT, a 4D NURBS-based cardiac-torso model that allows for the generation of realistic human anatomy and physiology [73]. The code generates a voxelized version of each virtual phantom. This voxelized representation can be used as a 3D labeled volume for the simulation.

The organ shapes of XCAT are based on the Visible Human Male and Female datasets from the National Library of Medicine [118]. Given that the phantom is NURBS-based, the organ shapes can be easily modified according to desired values. To ensure realistic geometrical representations, we used the torso

parameters measured from patient group *G1* and heart parameters from the literature [88, 119, 120] (for details see Table 4.2). We assumed all anatomical parameters follow normal distributions with mean (μ) and standard deviation (σ), truncated to the minimum and maximum values observed in our clinical population. Therefore, to generate each virtual subject, each anatomical parameter was assigned a random value $X \sim \mathcal{N}(\mu, \sigma^2)$ within the allowed range, as summarized in Table 4.2. Based on these distributions a total of 40 virtual subjects (20 females) were generated. Each phantom was computed with 8 types of tissue, labeled as displayed in Table 4.1, where label 0 corresponds to air background.

The cardiac cycle length was kept constant (1 s) for all virtual subjects. Hence, alterations on heart dynamics were limited to volume changes due to each individual heart shape. A total of 30 phases per cycle were generated for each virtual subject. Each set was represented by a stack of 221 axial slices of $512{\times}512$ pixels with a 0.78mm^3 isotropic voxel size. Axial stacks were reformatted to short-axis stacks with the true rotation angles used during phantom generation. Thanks to the isotropy of the axial volume, smooth short-axis slices could be obtained after 3D rotation. A short-axis stack, spanning the whole heart, was used as input to the simulator. For partial volume effect modeling, each simulated MRI slice was computed from 10 slices of the input phantom (simulated slice thickness=7.8mm/phantom slice thickness=0.78mm).

Modified Phantom

Initial simulations with the standard XCAT phantom generated images with a rather artificial appearance. Therefore we modified the phantoms to increase realism of the simulated images. We accomplished this by adding to the 40 original phantoms papillary muscles, trabeculae and tissue sublabels. The MR simulations were computed both for the 40 original and the 40 modified phantoms. Find below a detailed explanation of the modifications.

- *Papillary muscles:* there are two main left ventricular (LV) papillary muscles: anterior and posterior. They have been detailed in a preliminary work by Segars *et al.* [132], but not yet included in the XCAT. Therefore, we modeled them using the measurements from patient group *G2*. Each papillary muscle was assigned a thickness, an initial angle, an initial distance, a final angle, and a final distance (see Fig. 4.1-b). This allowed us to generate a 3D direction vector. At the intersections of this vector with each midventricular short-axis slice, 2D representations of the papillary muscles (disks) were placed. The following anatomical constraints were imposed to avoid unrealistic configurations of the papillary muscles: minimal and maximal **intra**-papillary angle and distance, minimal and maximal **inter**-papillary angle and distance (for details see Table 4.3).

  Three main processes occur to the papillary muscles during cardiac contraction: shortening, thickening and wall attachment. We used the XCAT dynamics as a basis for modeling these three processes. From the original XCAT phantoms, we can calculate the position of the LV base and the variation of the LV radius along the cardiac cycle. Shortening was simply

TABLE 4.1: MAGNETIC RESONANCE PARAMETERS PER TISSUE CLASS

		PATIENT GROUP *Literature*								
$n = 17$†	Label	0	1	2	3	4	5	6	7	8
	Sublabel	0-27	28-55	56-83	84-111	112-139	140-167	168-195	196-223	224-251
$[5-32]$‡	Tissue	Bkg	Lung	Bone	Body	Liver	Gastric	Peric	Myo	Blood
PD	mean	0	0.12	0.08	0.25	0.45	0.71	0.20	0.50	0.90
	SD	0	0.20	0.01	0.20	0.15	0.25	1.00	0.30	0.50
	max	0	0.20	0.10	0.30	0.50	0.90	1.00	0.70	1.00
	min	0	0.00	0.00	0.24	0.40	0.62	0.10	0.20	0.50
T1	mean	0	1199	269	549	586	765	500	982	1516
	SD	0	117	30	52	39	75	37	46	21
	max	0	1380	329	653	664	915	574	1092	1558
	min	0	1040	209	445	508	615	426	902	1474
T2	mean	0	79	55	49	46	58	70	54	189
	SD	0	29	21	20	20	24	21	12	26
	max	0	137	97	89	86	106	112	78	276
	min	0	21	13	9	6	10	28	30	115
T2*	mean	0	30	35	16	27	30	61	30	153
	SD	0	4	3.8	4	6	4	12	8	12
	max	0	38	43	24	38	38	85	49	223
	min	0	22	27.6	8	17	22	37	14	96

Each parameter was sampled from a normal distribution with mean and standard deviation (SD)

within the minimum (min) and maximum (max) values listed above.

Bkg= Background; Peric= Pericardium; Myo= Myocardium;

† Average and ‡ range of sample sizes from references [114, 121–131]

modeled by varying the initial longitudinal position of the papillary mus-
cles relative to the LV base. Since the LV base moves downwards (towards
the apex) during contraction, the initial longitudinal position of the pap-
illary muscles does as well. Wall attachment was modeled by reducing
the distance from the papillary muscles to the wall following the radial
dynamics of the phantom. In a similar manner, radial dynamics of the
phantom were used to increase the thickness of each papillary muscle.
The volume of each muscle is conserved over the course of a cardiac cycle
by adjusting its length. As a result, at end diastole (ED) papillary muscles
are thin, long and separated from the wall, while at end systole (ES) they
are shorter, thicker and touching the wall.

- *Trabeculae:* besides the papillary muscles, trabeculae are an important
component of the ventricular anatomy. However, the modeling of trabecu-
lae has been mainly focused on oxygen delivery processes and contractile
function [133, 134]. To the best of our knowledge, no previous mathemat-
ical model of spatial distribution of trabeculae has been proposed. Our
modeling strategy takes into account the reported anatomical descrip-
tions of trabeculae [135], along with careful observation of our clinical
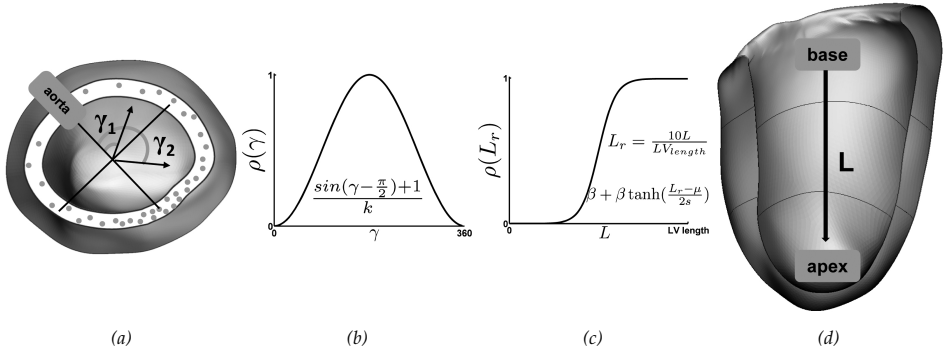datasets. Basically, the amount of trabeculae increases from base to apex.

Figure 4.2: *Illustration of trabeculae generation. The density of trabeculae*
$(\rho_{trab} = \rho(\gamma) \cdot \rho(L_r))$ *increases with: (a-b) angular distance (γ) from the aorta, and (c-d)*
longitudinal distance (L) from the base (k = 180, β = 0.5; μ = 5; s = 3).

They are absent along the outflow track towards the aorta in the LV and
towards the pulmonary trunk in the right ventricle (RV). In addition, they
are more visible at ED. During contraction, trabeculae are displaced until
they are fused with the wall.

To resemble this, we used the following procedure (see Fig. 4.2):

▶ We selected all short-axis slices from LV base to LV apex.

▶ On each slice *i*, we selected a region adjacent to the wall of both
ventricles. The region included all possible locations of trabeculae
on slice *i*, where *region thickness* = 0.7 × *LV wall thickness*.

▶ Within this region, a random location was selected to place a trabec-
ular structure, represented as a 3-pixels-wide disk.

▶ For each slice *i*, this process was repeated until a desired density of
myocardium (myocardium/blood ratio) was achieved. The desired
trabeculae density was calculated as $\rho_{trab} = \rho(\gamma) \cdot \rho(L_r)$, with Eq. 4.1
and Eq. 4.2:

$$\rho(\gamma) = \frac{\sin(\gamma - \frac{\pi}{2}) + 1}{k} \tag{4.1}$$

$$\rho(L_r) = \beta + \beta \tanh(\frac{L_r - \mu}{2s}) \tag{4.2}$$

$$L_r = \frac{10L}{LV_{length}}, \tag{4.3}$$

where γ = angular distance from aorta, k = 180, β = 0.5, μ = 5,
s = 3 and *L*=longitudinal distance from the base.

▶ In order to add a component in Z-direction to the trabecular struc-
tures, the obtained pattern was repeated for the following 10 slices.
Then, for slice $i + 10$ a new trabecular pattern was computed.

▶ A myocardium label was assigned to each of the trabecular structures.

Given the rapid change in LV radius at apical level, for slices with $L_r > 0.65$ (Eq. 4.3) the trabecular pattern was updated every $i + 3$ slices. For these same slices, $\rho(\gamma)$ was set to 0.16 to resemble the uniform radial distribution of trabeculae at apical level.

For each subject, the trabecular pattern was determined at ED and maintained alike for the duration of the cardiac cycle. The process of wall thickening (as modeled by XCAT) naturally managed to reduce the density of trabeculae throughout the cycle. Meaning, as the wall thickens it displaces trabeculae until they appear to be fused with the wall.

- *Tissue sublabels:* even with the Gaussian noise added by the simulator, the variability of the intensity distributions of simulated images based on the original phantom was found to be limited. Mainly, the input phantom allows for a unique label per tissue, which results in a unique intensity value on the simulation output. In a real acquisition, however, tissues have a wider range of intensities. We aimed at incrementing intensity realism by increasing the number of labels in the input phantom. The modification was done such that each original label was composed of 27 randomly distributed sublabels (reaching the 255 maximum labels allowed by the simulator). Afterwards, magnetic resonance properties were assigned to each sublabel according to its original tissue class. Properties were sampled from a normal distribution with mean and standard deviation (SD), as listed in Table 4.1, which were gathered from the literature [114, 121–131].

- *Partial volume effect:* due to the spatial resolution inherent to every image modality, some of the pixels of an acquired image are a contribution of multiple types of tissue. This basically translates into blurriness and is particularly noticeable at the edges of most organs. Aiming to resemble this effect, a higher resolution phantom was used as input to the simulator (double the in-plane resolution). Therefore, the intensity value of each voxel in the output image included the contribution of 40 voxels from the input phantom: 4 pixels in each of the 10 slices.

4.2.5 Experimental Evaluation

Typical intensity distributions were obtained from group *G3* to evaluate the realism of the simulated results. To cope with the inconsistency of intensity values typical of MRI data, intensity values of all the datasets were standardized with the approach proposed by Nyul *et al.* [136]. Briefly, this method deforms the histogram of the sample image to a previously defined histogram by using a set of landmarks. In our case the set of landmarks included: s_1 and s_2 representing the minimal and maximal intensities, respectively, and μ_{01} and μ_{97} with μ_p representing the pth percentile. The final configuration of these parameters were: *min*=0, μ_{01}=2, μ_{97}=53083, *max*=65535.

A region-of-interest (ROI) for the most relevant tissues for cardiac appli-
cations were outlined by a researcher with experience in cardiac MRI in two
independent sessions. Each ROI included the largest possible area with an ho-
mogeneous visual appearance. For each patient of group *G3*, one basal, one
midventricular and one apical slice, both at ED and ES, were processed. Five
ROI's per slice were obtained: lung, pericardium, myocardium, blood and tra-
becular region of both ventricles (including papillary muscles). This yielded
300 manually delineated ROI's per session, for a total of 600 ROI's to be used
as gold standard. For the virtual datasets, intensity distributions of each tis-
sue were obtained automatically using binary masks derived from the original
labeled phantoms. After intensity standardization, the distributions were aver-
aged for all the virtual subjects.

Average real distributions were compared with average simulated distribu-
tions with the *1)* original phantom and *2)* the modified phantom as input. All
of them were analyzed with histograms. All histograms were obtained with a
consistent number of bins, estimated according to Scott's rule (70 bins) [137].
Histograms were then compared using two distance metrics: chi-square dis-
similarity metric (χ^2) [137] and Kullback–Leibler divergence (KL) [138]. χ^2 was
calculated with Eq. 4.4 and KL was calculated with Eq. 4.5. For both of them
P is the real histogram, **Q** is the simulated histogram, and *n* is the number of
bins:

$$\chi^2 = \sum_{i=1}^{n} \frac{(\mathbf{P}_i - \mathbf{Q}_i)^2}{\mathbf{P}_i + \mathbf{Q}_i} \tag{4.4}$$

$$D_{KL}(P||Q) = -\sum_{i=1}^{n} \mathbf{P}_i \log(\mathbf{Q}_i) + \sum_{i=1}^{n} \mathbf{P}_i \log(\mathbf{P}_i) \tag{4.5}$$

4.3   Results

4.3.1   Anatomical Variability

Measurements describing anatomical variability of our clinical datasets are dis-
played on Table 4.2. This table includes parameters obtained from group *G1*
and from the literature (marked with †, ‡ and §). Measurements for papillary
muscles modeling, all obtained from group *G2*, are summarized in Table 4.3.

4.3.2   Simulated Images

Some examples of the simulated images with both input phantoms are shown
in Fig. 4.3. The simulated images based on the modified phantom show good
resemblance of the intensity values from real images. However, mainly due to
the simplified anatomy of the virtual population, they still have a synthetic
appearance. Note that the right ventricular papillary muscles, very visible in
the real dataset (Fig. 4.3-e-f), are not yet included in our model. Fig. 4.5 shows
simulated images from a different virtual patient in several stages of the cardiac
cycle. We can observe the behavior of the LV papillary muscles along the cycle.

TABLE 4.2: ANATOMICAL PARAMETERS FOR TORSO AND HEART VARIATION ACCORDING TO GENDER

		TORSO							HEART						
		Torso		Ribcage		Breasts			Size†		Ori‡		Trans‡		Peri§
$n = 40$		LA	SA	LA	SA	LA	SA	θ	Lth	Dmt	ϕ	ψ	Lat	P-A	Thk
		cm	*cm*	*cm*	*cm*	*cm*	*cm*	°	*cm*	*cm*	°	°	*cm*	*cm*	*mm*
Female	mean	31.4	21.3	26.0	18.1	18.2	4.8	141	7.2	4.6	27	40	5.2	-5.0	1.2
	SD	2.99	2.44	2.13	2.24	2.32	1.5	2	0.5	0.3	9	13	1.1	2.6	0.8
	max	35.1	24.9	28.9	22.2	21.0	8.4	176	8.1	5.1	54	76	8.5	0.2	2.5
	min	23.8	15.0	20.7	12.5	11.5	2.0	110	6.3	4.1	8	16	3.0	-10.6	0.0
Male	mean	34.6	25.2	29.8	21.5	*n.a.*	*n.a.*	*n.a.*	8.3	5.0	21	36	5.6	-6.4	1.2
	SD	2.12	2.37	2.12	2.77	*n.a.*	*n.a.*	*n.a.*	0.6	0.4	9	12	1.1	2.6	0.8
	max	37.7	30.3	34.4	27.0	*n.a.*	*n.a.*	*n.a.*	9.4	5.8	41	73	8.0	1.2	2.5
	min	28.5	20.4	25.4	17.1	*n.a.*	*n.a.*	*n.a.*	7.0	4.2	0	15	3.5	-11.6	0.0

Each parameter was sampled from a normal distribution with mean and standard deviation (SD) within the minimum (min) and maximum (max) values listed above. Heart parameters from [119]†, [88]‡ and [120]§; Ori= Orientation; Trans= Translation; Peri= Pericardium; LA= Long Axis; SA= Short Axis; Lth=Length; Dmt= Diameter; Lat= Lateral; P-A= Posterior-anterior; Thk= Thickness; *n.a.*= Not applicable.

For the original phantom, χ^2 values averaged 0.65±0.06 and KL values averaged 0.69±0.38. For the modified phantom, χ^2 values averaged 0.34±0.12 and KL values averaged 0.32±0.15. Meaning that the modifications applied to the phantom improved the simulated histograms by 48% according to χ^2 and 54% according to KL.

Fig. 4.4 plots the resulting χ^2 and KL values for each of the tissues at basal, midventricular, apical level, both at ED and ES. It can be observed that the modifications of the phantom resulted on the improvement of the intensity distributions for the lung, myocardium and blood. The pericardial tissue was not specially improved. Looking at the histogram it is evident that this tissue presents a wide range of intensity values and both real and simulated histograms have coarse features. This is understandable since the intensity values of the pericardium has a high inter-patient variability given its components (i.e. fat and fluid).

TABLE 4.3: CLINICAL MEASUREMENTS FOR PAPILLARY MUSCLES MODELING

PATIENT GROUP G2

n = 10	ANGLE Ant Init (°)	Ant Final (°)	Ant Intra (°)	Pos Init (°)	Pos Final (°)	Pos Intra (°)	Inter Init (°)	Inter Final (°)	DISTANCE Ant Init (ratio)	Ant Final (ratio)	Ant Intra (ratio)	Pos Init (ratio)	Pos Final (ratio)	Pos Intra (ratio)	Inter Init (ratio)	Inter Final (ratio)	THCK Ant (ratio)	Pos (ratio)
mean	64.3	50.8	n.a.	82.8	66.1	n.a.	n.a.	n.a.	0.50	0.20	n.a.	0.42	0.17	n.a.	n.a.	n.a.	0.43	0.39
SD	13.9	16.9	n.a.	21.3	24.8	n.a.	n.a.	n.a.	0.07	0.08	n.a.	0.06	0.07	n.a.	n.a.	n.a.	0.11	0.08
max	93	88	34	121	112	29	183	158	0.51	0.32	0.43	0.52	0.29	0.35	0.29	0.18	0.57	0.57
min	49	35	5	54	25	8	112	74	0.45	0.10	0.24	0.33	0.06	0.15	0.00	0.00	0.28	0.30

Each parameter was sampled from a normal distribution with mean and standard deviation (SD) within the minimum (min) and maximum (max) values listed above.

Distance= *(distance to wall)/(LV end diastolic radius)*; Thck= *(thickness)/(LV end diastolic radius)*;

Ant= Anterior papillary muscle; Pos= Posterior papillary muscle; Inter= Inter-papillary;

Intra= Intra-papillary; Init= Value at midventricular level; Final= Value at apical level; *n.a.*= Not applicable.
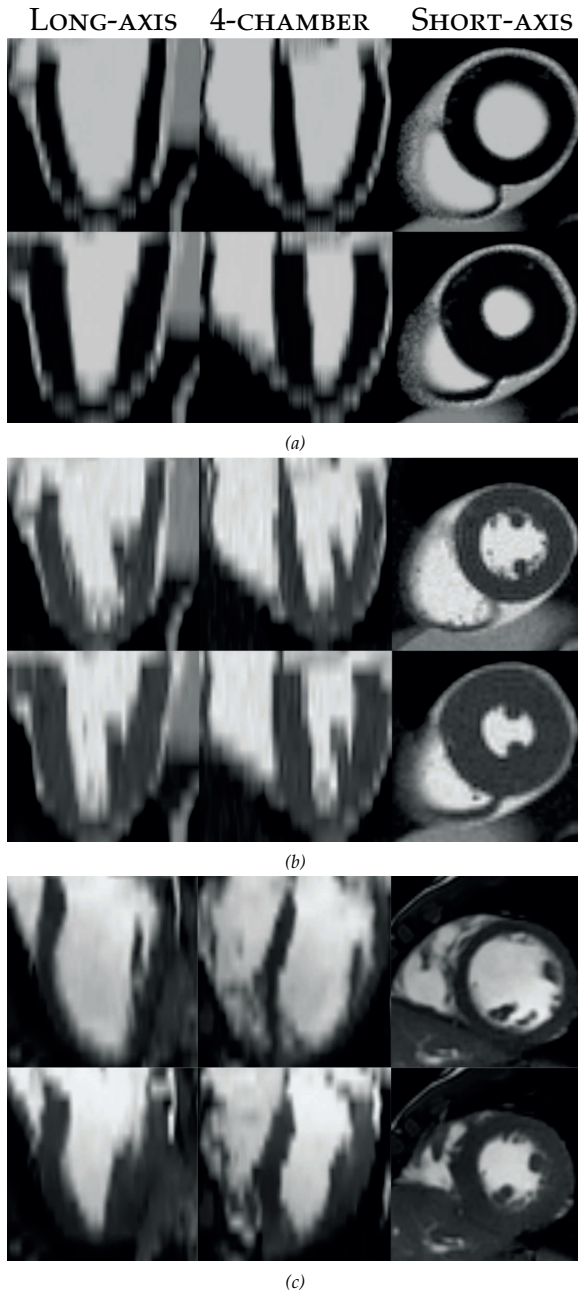
LONG-AXIS   4-CHAMBER   SHORT-AXIS

(a)

(b)

(c)

Figure 4.3: *Examples of simulated images with the original phantom (a) at End Diastole (top) and End Systole (bottom). Examples of simulated images with the modified phantom (b) at End Diastole (top) and End Systole (bottom). Examples of a real dataset (c) at End Diastole (top) and End Systole (bottom).*
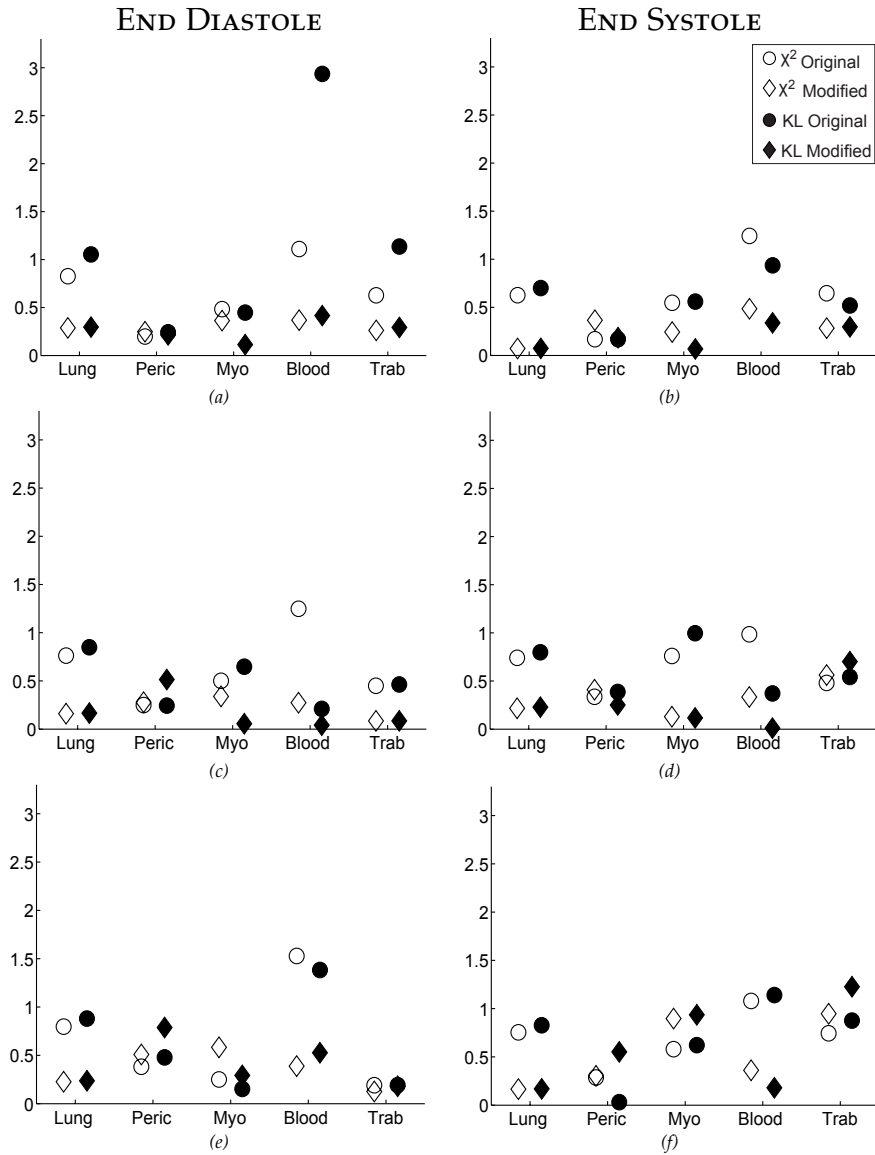
Figure 4.4: *Plot of the Chi–square dissimilarity metric (χ^2) and the Kullback-Leibler divergence (KL) at basal (a-b), midventricular (c-d) and apical level (e-f). Note that lower metric values represent more similar histograms. Histograms were computed from the whole population for each tissue and normalized by the number of samples per ROI. Peric= Pericardium; Myo= Myocardium; Trab= Trabecular region.*

To further analyze the behavior of blood, trabecular region and myocardium in our data, Fig. 4.6 displays representative histograms of these tissues. Simulated histograms of blood from the original phantom are characterized by a sharp peak at high intensity. On the other hand, in real histograms the peak is smoother and much lower. The modified phantom better resembles this behavior, specially at basal and midventricular level (Fig. 4.6-a-d). Fig. 4.6-d shows the blood histogram with the largest improvement of the modified phantom with respect to the original phantom, according to both metrics.

For the trabecular region, the simulated distributions from the modified phantom improved the similarity to the real histograms at all levels of the end diastolic phase (Fig. 4.6-b). The improvement of this tissue was less noticeable at end systole. Particularly at ED apical level, the trabecular region presents a good match of the real myocardium/blood ratio (Fig. 4.4-e). On the other hand, the ES apical level, we can observe that high intensity components of blood were reduced, but the presence of trabecula was not strong enough to match the darker components of the real histogram (Fig. 4.6-e).

For the myocardium, the simulated distributions from the modified phantom were very similar to the real distributions both at basal and midventricular levels (Fig. 4.4-a-d, Fig. 4.6-c). At the apical level, however, the distribution was slightly shifted towards higher intensities. Therefore, regardless of its very similar shape, the metrics were not favorable (Fig. 4.4-e-f, Fig. 4.6-f).

4.4   Discussion and Conclusions

Our approach has demonstrated a noticeable improvement of the local appearance of the simulated images with respect to the ones obtained initially. These are favorable results with potential use in edge driven algorithms or algorithms based on average intensity distributions. Furthermore, the simulated images can be generated with different MRI sequences, increasing the applicability of our proposed strategy. These algorithms will then aid daily clinical practice by providing accurate tools to make the postprocessing of cardiac studies easier and faster.

Evidently, the amount of details found on real images are far greater than the details obtained with the simulation strategy proposed with our work. For instance, our research is focused on cardiac structures, which led us to overlook typical characteristics of other tissues, such as liver vessels or stomach contents.

Another characteristic that gives the simulated images still a synthetic appearance is that cardiac structures are based on basic geometrical shapes. Therefore, despite the positive match of real and simulated intensity distributions, the shape and dynamics of the cardiac structures seem oversimplified. Current research on modeling of cardiac shape and dynamics is under development worldwide.

Finally, the modeling strategy we proposed was specially targeted to the influence of intracavitary structures on the final appearance of cardiac MRI datasets. This is, however, a simplified approach and requires further investigation if aimed at applications with detailed anatomical information (i.e. electrophysiological/mechanical simulations).

In summary, this manuscript presents a realistic cardiac MRI simulation pipeline based on the MRISIM simulator and the XCAT phantom. Phantoms were modified in order to include relevant intracavitary structures, such as papillary muscles and trabeculae. The modeling of all cardiac structures was based on clinical measurements and published data. Performance was measured by comparing data of 40 virtual datasets with 10 clinical datasets. The modifications applied to the phantom improved the simulated histograms by 48% according to χ^2 and by 54% according to KL. In this sense, the comparison of histograms indicated a good match between the local appearance of real and simulated images. Results are quite encouraging for potential use in training and evaluation of image processing and analysis algorithms. Since our approach is based on the XCAT phantom, and all anatomical measurements are summarized, this strategy can be easily implemented by other researchers. Further improvements may include the addition of motion artifacts due to respiration and addition of right ventricular papillary muscles.
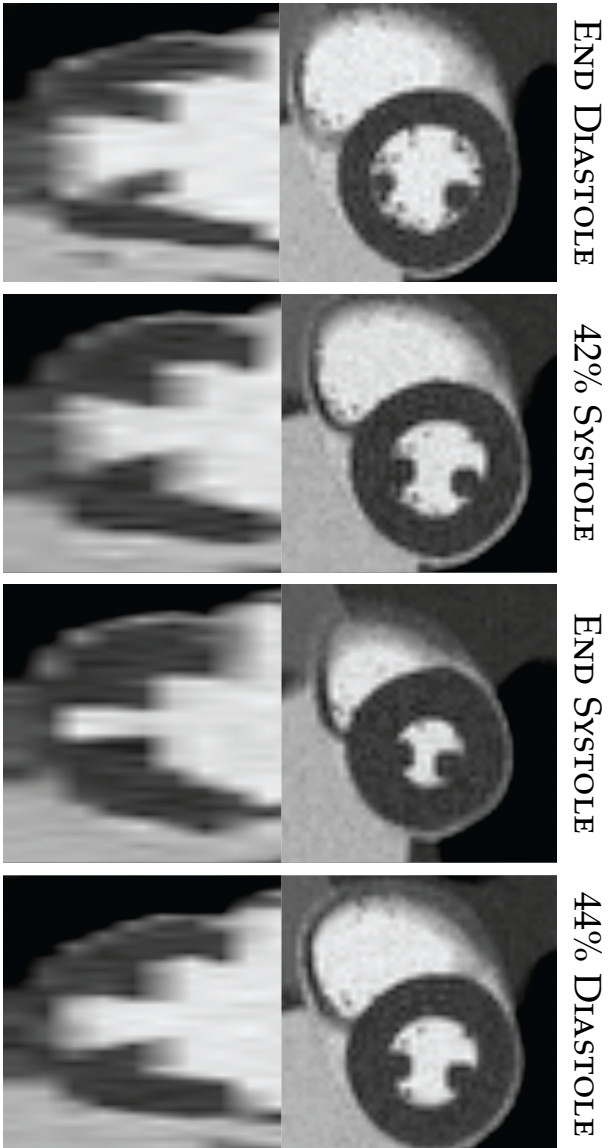
Figure 4.5: *Simulated images from a virtual patient in several stages of the cardiac cycle. During contraction, trabeculae are displaced until they are fused with the wall (top), and papillary muscles become shorter and thicker (bottom).*
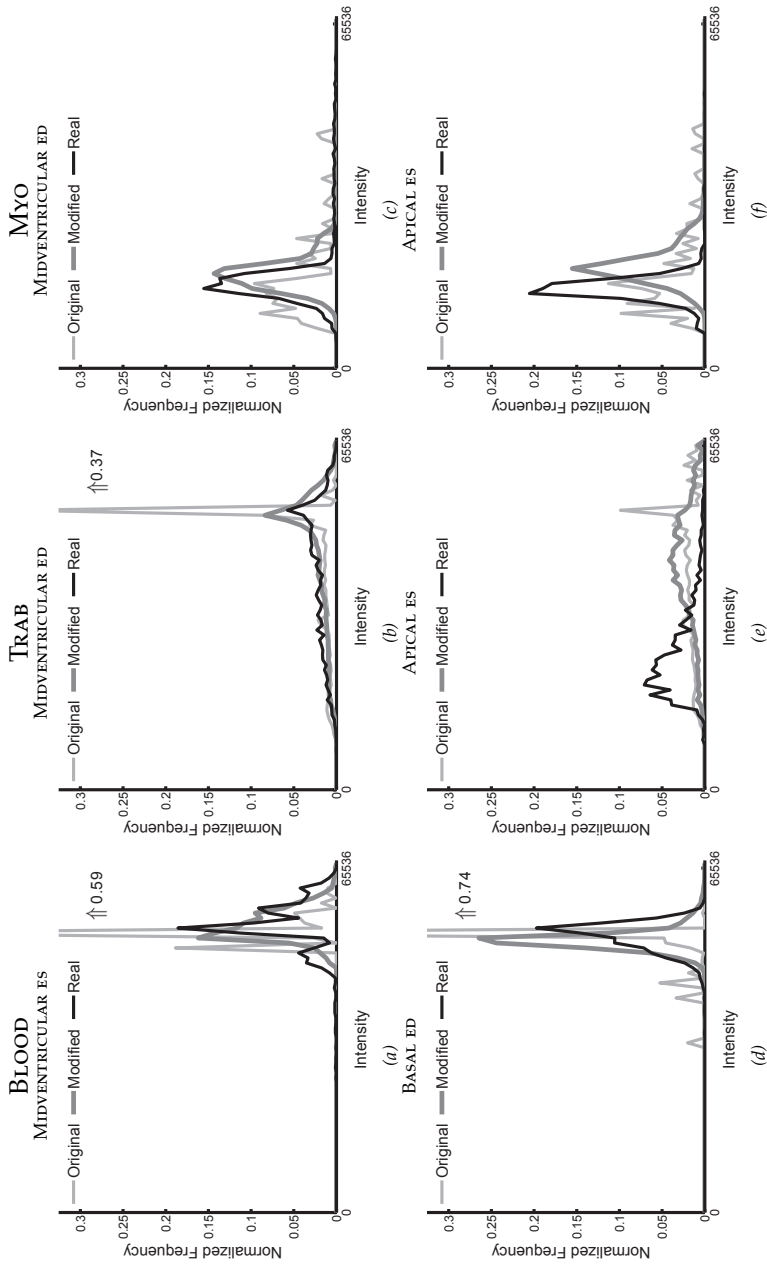
Figure 4.6: *Representative histograms of blood, trabecular region (trab) and myocardium (myo). Histograms were computed from the whole population for each tissue and normalized by the number of samples per ROI. The ⇑ value represents the peak value of the histogram from the original phantom. Blood histogram with the lowest KL value for the modified phantom (a) and the largest improvement with respect to the original phantom (d). Trab histogram with the lowest (b) and the highest (e) KL value for the modified phantom. Myo histogram with the lowest (c) and the highest (f) KL value for the modified phantom.*

5

Automatic Training and Reliability Estimation for 3D-ASM Applied to Cardiac MRI Segmentation

Catalina Tobon-Gomez, Federico M. Sukno, Constantine Butakoff, Marina Huguet and Alejandro F. Frangi

Abstract

Model-based approaches are widely used in cardiac segmentation. In this paper, we use a 3D Active Shape Model (3D-ASM) approach to segment the left and right ventricular cavities from cardiac MRI studies. Training the ASMs requires the collection of manual ground-truth meshes in a large image database. While shape information can be reused across multiple imaging modalities, intensity information needs to be imaging modality- and protocol-specific. In this context, this study has two main purposes: *1)* to test the potential of using intensity models learned from MRI simulated datasets, *2)* to test the potential of including a measure of reliability during the matching process to increase robustness. We used a population of 400 virtual subjects (XCAT phantom), and two clinical populations of 40 and 45 subjects. A subset of 20 studies was segmented by a radiologist to evaluate inter-observer variability (IV). Virtual subjects were used to generate simulated datasets (MRISIM simulator). Real datasets included short-axis slices at end diastole and end systole. Intensity models were trained both on simulated and real datasets. The trained models were used to segment the left (LV) and right ventricles (RV) from real datasets. Segmentations were also obtained with and without reliability information. The methodology was analyzed for each pathology and tested for initialization sensitivity. Performance was evaluated with point-to-surface and volume errors. Simulated intensity models achieved accuracy 15% below IV for LV. Discrepancies on LV volume measurements were within the limits of IV (10ml for volumes and 5% for EF). The right ventricular model of the simulated images needs further improvement to generate proper profiles around the myocardial edges. The inclusion of reliability information proved to increase robustness of the segmentation process making it less sensible to initialization and reducing the influence of outliers in difficult areas.

5.1   Introduction

Imaging data has become essential in clinical routine. Analyzing it often requires extensive manual postprocessing. Most of the collected information is disregarded during actual diagnosis/treatment. This fact has motivated the development of computer based techniques to translate the data into clinically relevant and quantitative information.

In the cardiac field, model-based approaches have found wide acceptance given the 3D (or 3D+t) nature of most data [76, 139, 140]. Active Shape Models (ASMs) is one of these approaches [51, 141]. It is based on a generic template of the target organ, which encodes knowledge of shape variability across a population. The template is constituted by a distribution of landmarks, known as a Point Distribution Model (PDM). To construct a PDM, several training steps must be fulfilled. While in 2D datasets these training steps are achievable with manual processing, in 3D datasets they are nearly unfeasible. This complication has inspired the development of automatic techniques for PDM construction. Some authors have proposed techniques for auto-landmarking surface [53–55] or volumetric [56, 57] representations of the target organ. Other authors have

shown techniques that work directly from raw images [58,59].

Fitting a PDM to unseen data requires knowledge about the appearance of the image being processed. ASMs have a second component, known as gray-level or intensity model, which takes care of this. However, the appearance of the images changes from modality to modality. Thus, to be able to handle multi-modal datasets, the intensity model needs retraining. That requires the collection of manual ground-truth contours. To bypass this step, several authors have proposed to reuse a previously built PDM and generate the appearance information some other way [46,61,62]. [61] use a few manual delineations per modality, which are propagated and refined with the Simulated Search method. [62] use a fuzzy inference system based on relative intensity differences. Our approach is to learn the intensity models from simulated datasets. We have previously explored this concept on gated Single Photon Emission Computed Tomography (gSPECT) studies, obtaining sub-voxel accuracy [46]. However, applying this method to a modality with higher spatial resolution, such as MRI, raises a new question regarding its achievable accuracy.

The aim of this study is to test two hypotheses in the context of cardiac MRI segmentation with a 3D-ASM approach. *1)* An intensity model trained with simulated images can obtain segmentation accuracy comparable to inter-observer variability; *2)* Including a measure of reliability during the matching process can increase robustness. To test hypothesis 1, we train the intensity models with simulated images generated as described in [47]. We evaluate the segmentation accuracy obtained with these models in comparison to the inter-observer variability. We also compare their accuracy with the accuracy obtained with models trained on real images from manual ground-truth meshes. Unlike gSPECT studies, in MRI studies both ventricular cavities are visible. Therefore, we use a bi-ventricular model for our segmentation approach (further details in Section 5.5.1). To test hypothesis 2, we employ the generic reliability measure for statistical shape models proposed by [74]. Only the landmarks labeled as *reliable* are used to deform the PDM during matching (further details in Section 5.3). In Section 5.8.3, we discuss our results considering other model-based cardiac segmentation studies [61,62,142–144].

5.2   Active Shape Models

The essential components of an ASM are: a shape model, an intensity model, and a matching algorithm (full description in [51]). The shape model is a template of the organ of interest represented as a distribution of landmarks or Point Distribution Model (PDM). The PDM encodes statistical information of variability in the training set. For a 3D space, a linear PDM trained from n shapes, $\{\mathbf{x}_i; i = 1, \ldots, n\}$, of m landmarks each, $\{\mathbf{l}_j = (l_{xj}, l_{yj}, l_{zj}); j = 1, \ldots, m\}$, is a linear model defined as:

$$\mathbf{x} = \bar{\mathbf{x}} + \mathbf{\Phi}\mathbf{b} \tag{5.1}$$

where $\mathbf{x}$ is a concatenated vector of all landmark coordinates in the form $(l_{x1}, l_{y1}, l_{z1}, l_{x2}, l_{y2}, l_{z2}, \cdots, l_{xm}, l_{ym}, l_{zm})$. Then, $\bar{\mathbf{x}}$ is the average of all aligned shapes, $\mathbf{b}$ is the shape parameter vector of the model, and $\mathbf{\Phi}$ is a matrix formed

---

Algorithm 2 Matching with Reliability Information

 1: **repeat**
 2:     **Intersect**(ImageStack,InitialShape)
 3:         **for all** Intersection points **do**
 4:             Find closest mesh vertex
 5:         **end for**
 6:         CountourStack←Create 2D contours
 7:     **Candidates**(CountourStack,MeanProfiles)
 8:         **for all** Possible profile positions **do**
 9:             Mahalanobis(MeanProfiles,SampledProfiles)
10:         **end for**
11:         **if** MinMahalanobis $< \zeta_{th}$ **then**
12:             CandidatePoints←Update best positions
13:         **end if**
14:     **ForcePropagation**(CanditatePoints)
15:         **for all** CandidatePoints **do**
16:             UpdateVectors←Calculate weight w
17:         **end for**
18:         DeformedShape←Apply forces to mesh
19:     **NewValidInstance**(DeformedShape)
20:         BestFit←Best parameters to fit DeformedShape
21: **until** Iterations completed

---

by the principal components of the covariance matrix:

$$\mathbf{S} = \frac{1}{n-1} \sum_{i=1}^{n} (\mathbf{x}_i - \bar{\mathbf{x}})(\mathbf{x}_i - \bar{\mathbf{x}})^T \tag{5.2}$$

The intensity model, as mentioned in the introduction, learns the appearance around the boundaries of the target organ. Typically, this means sampling a 1D profile of gray-level values (or gradients) for each landmark along the direction perpendicular to the boundary. From the values sampled along each profile, the mean vector and covariance matrix are estimated. The matching algorithm uses the intensity model to match unseen image data. Our approach is based on the sparse fitting method SPASM [77]. It is sparse in the sense that image data is obtained only from the acquired image planes. This characteristic is quite relevant for MRI datasets given their anisotropic nature. The algorithm first finds the intersections of the mesh with the image planes. These intersections make a stack of 2D contours. Each landmark in the contour stack will be displaced to a new location. The new location, or candidate position, is selected by locally searching a profile which better resembles the one stored during training. In our case, the best candidate position is selected by computing the minimal Mahalanobis distance between the sampled profiles and the mean profiles of the intensity model. Each candidate point forces a deformation on the mesh. The deformation propagates to the rest of the nodes with a weighting function, normalized by a Gaussian kernel. The mesh is deformed for several iterations until a best-fit is found.
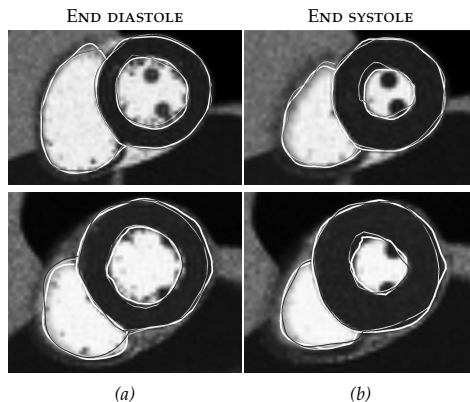
Figure 5.1: *Images from virtual group V1: two virtual patients at end diastole (a) and end systole (b). Edges obtained automatically by 3D-ASM with simulated intensity models are displayed in color. Thick white= ground-truth surface; Dark gray= matched surface with no reliability; Light gray= matched surface with reliability.*

5.3   Reliability Estimation

In this work, we use the generic approach proposed by [74]. This method uses a probabilistic framework to identify whether the position identified by the image model for a given landmark is trustworthy (*reliable*). The reliability $\hat{r}_i^{(j)}$ can be thought of as an estimation of the random variable $r_i^{(j)}$, which indicates whether landmark *j* of shape *i* is correctly placed. The landmark will be labeled as reliable when its distance with respect to the ground-truth position is within the intrinsic precision of the algorithm.

To compute reliability thresholds, we run the matching algorithm on the training set. At each iteration, we store the minimal Mahalanobis distance for each landmark. Then, for each landmark *j-th* of shape *i*, we compute the segmentation error $\epsilon_i^{(j)}$ from the ground-truth. The threshold ζ_{th} is chosen to maximize the mutual information between $\hat{r}_i^{(j)}$ and $r_i^{(j)}$ across the training set:

$$\zeta_{th}^{(j)} = \underset{x}{\mathrm{argmax}} \ MI\left(1(\epsilon_i^{(j)} < \epsilon_{th}^{(j)}); 1(\zeta_i^{(j)} < x)\right) \qquad (5.3)$$

where $MI(x,y)$ is the mutual information between x and y, and 1(b) is one if b = true and zero otherwise. The thresholds ζ_{th} are stored to be used during matching. The steps of the algorithm, including reliability information, are described in **Algorithm 2**.

5.4 Image Datasets

5.4.1 Population Group 1 (V1)

This population included 400 virtual subjects generated with XCAT [73]. The XCAT generates a voxelized version of each virtual subject containing several thoracic structures: heart, great vessels, lungs, ribs, liver, spleen, stomach, intestines, body background. Each volume was represented by a stack of 221 axial slices of 512×512 pixels with a 0.78mm^3 isotropic voxel size. We reformatted the axial stacks with the true rotation angles used during phantom generation. Each short-axis stack was used as input to the simulator (further details in Section 5.5.1). This group was used for training and testing (see Fig. 5.1).

5.4.2 Clinical Population Group 1 (C1)

This group included 40 patients, with 12 healthy subjects, 18 patients with hypertrophy, and 10 patients with infarction. The studies were acquired using a GE Signa CVi-HDx, 1.5T scanner (General Electric, Milwaukee, USA). Short-axis images were scanned with a Steady State Free Precession (SSFP) sequence. The slice thickness was 8mm with an in-plane pixel resolution of 1.56mm × 1.56mm. Both left and right ventricles (LV and RV) were manually segmented at End Diastole (ED) and End Systole (ES) by an experienced researcher. A subset of 20 studies was segmented by a radiologist to evaluate inter-observer variability. This group was used for training and testing.

5.4.3 Clinical Population Group 2 (C2)

This group included 45 patients, with 9 healthy subjects, 12 patients with ischemic heart failure, 12 patients with non-ischemic heart failure and 12 patients with hypertrophy. The database was collected at Sunnybrook Health Sciences Centre as part of the cardiac MRI LV segmentation challenge [145]. The studies were acquired using a GE Signa, 1.5T scanner (General Electric, Milwaukee, USA). Short-axis images were scanned with a SSFP sequence. The slice thickness was between 8mm and 10mm with an in-plane pixel resolution of 1.36mm × 1.36mm. Ground-truth contours, provided in the segmentation challenge package, were drawn by an experienced cardiologist. The contours included endo and epicardium at ED and endocardium at ES. All the contours were confirmed by another cardiologist. This group was used for testing only.
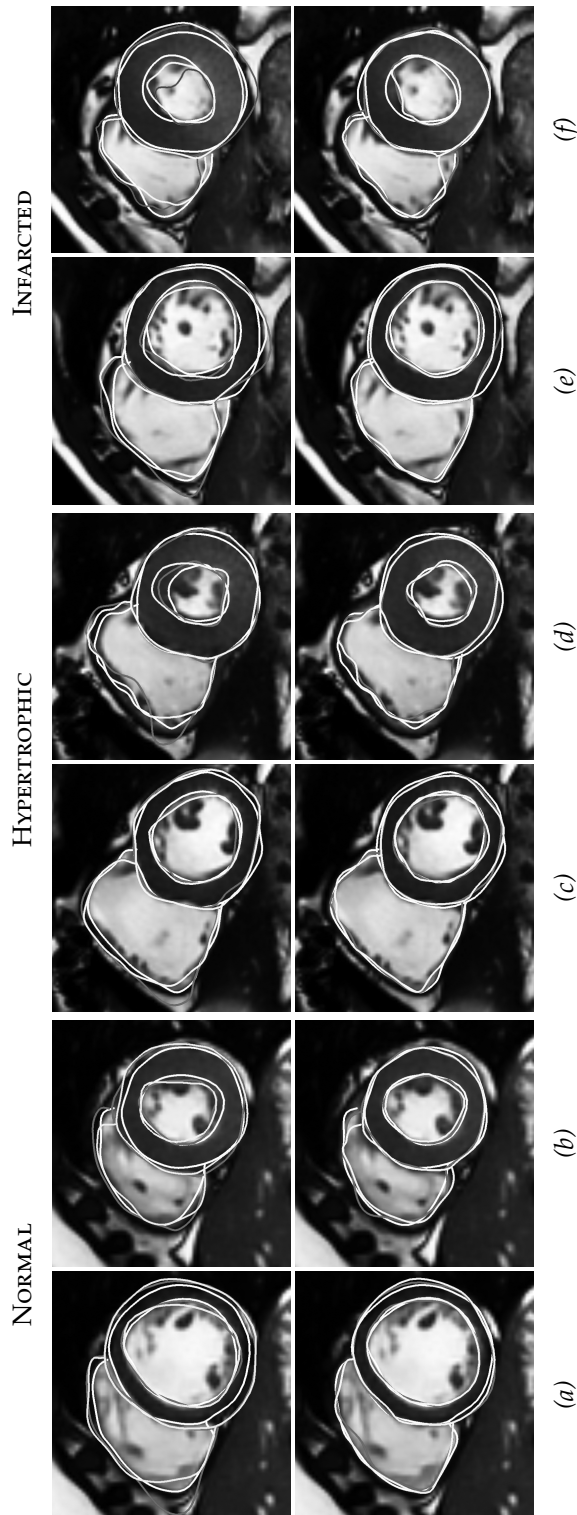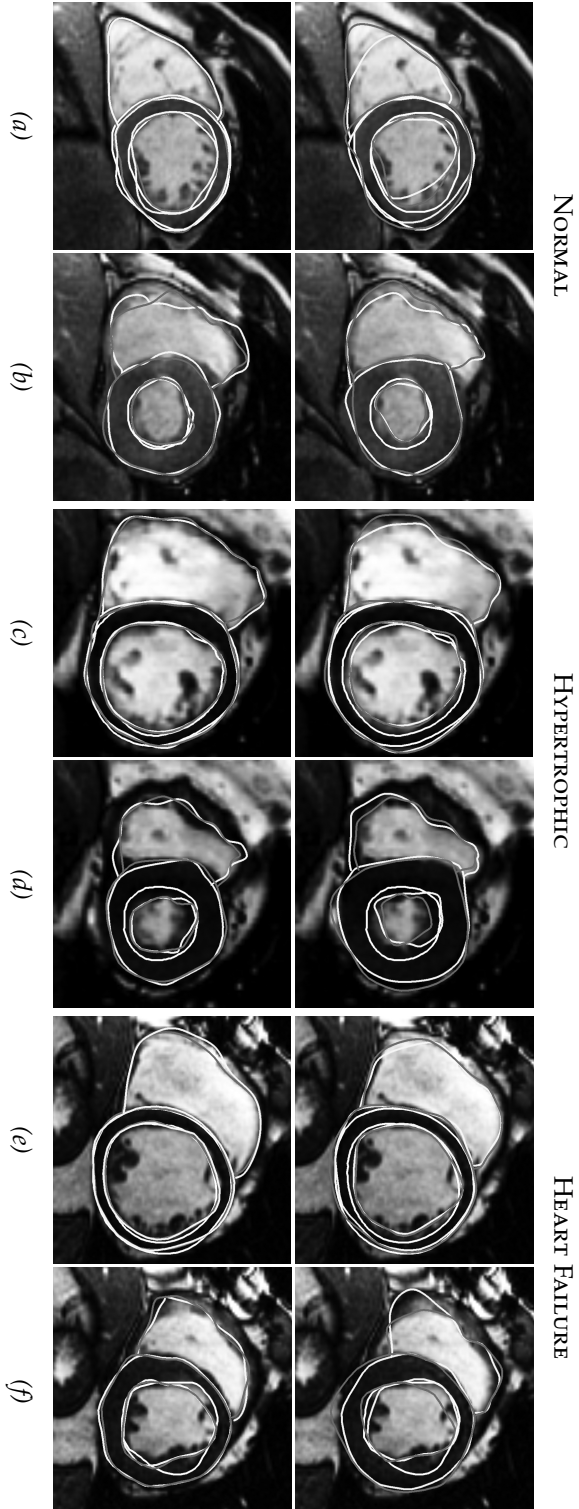
Figure 5.2: *Images from clinical group C1: a normal subject (a-b), a hypertrophic patient(c-d), and an infarcted patient (e-f). Edges obtained automatically by 3D-ASM with simulated (top) and real (bottom) intensity models at end diastole (a,c,e) and end systole (b,d,f). Note the influence of reliability information for the simulated models (top), specially for the right ventricle. White= ground-truth surface; Red= matched surface with no reliability; Yellow= matched surface with reliability. (See color insert)*

Figure 5.3: *Images from clinical group C2: a normal subject (a–b), a hypertrophic patient(c–d), and a heart failure patient (e–f). Edges obtained automatically by 3D-ASM with simulated (top) and real (bottom) intensity models at end diastole (a,c,e) and end systole (b,d,f). Note the influence of reliability information for the simulated models (top), specially for the left ventricular epicardium. White= ground-truth surface; Red= matched surface with no reliability; Yellow= matched surface with reliability. (See color insert)*

NORMAL

HYPERTROPHIC

HEART FAILURE

(a) (b) (c) (d) (e) (f)

5.5 Methods

5.5.1 MRI Simulation

The MRI simulator used in this work models the physical phenomena by solving the Bloch equations [72]. It uses a labeled volume as input, where each label corresponds to a tissue with certain magnetic resonance properties.

The virtual population in group V1 was used as input to the simulator. Each virtual patient was modified to increase the realism of the simulated images. These modifications were evaluated in [47]. Briefly: *1)* we included papillary muscles in the LV and trabecular structures in both ventricles. Papillary muscles generation was based on clinical measurements and trabeculae generation was based on a mathematical model; *2)* we incremented the intensity variability of each body tissue in the simulated image by increasing the number of labels of the virtual patient. Magnetic resonance properties, gathered from the literature, were assigned to each sublabel according to its tissue class; *3)* we modeled partial volume effect by using a higher resolution virtual patient as input to the simulator. Each pixel was computed from 4 input pixels and each slice was computed from 10 input slices. Therefore, each voxel in the output image included the contribution of 40 voxels from the input virtual patient. An example of the obtained simulations can be found in Fig. 5.1.

5.5.2 3D-ASM Training

Our shape model is a surface mesh representing the left and right ventricles. The model is constituted by three regions: LV endocardium, LV epicardium and RV endocardium. This configuration is a subpart of a whole heart model trained from 100 high-resolution CT datasets [59].

For intensity model training, we require all training meshes to have identical topology. To accomplish this on the simulated datasets, we extracted the LV and RV as binary masks from the 3D labeled phantoms in group V1 (Section 5.4.1). We generated isosurfaces from the binary images. Our shape model was aligned to these surfaces using finite Iterative Closest Point registra-

TABLE 5.1: Parameters used for 3D-ASM segmentation

Shape Model	Number of nodes	
LV endocardium	880	
LV epicardium	1797	
RV endocardium	3478	
Intensity Model	*Profile*	
Length	17	
Sampling interval	1.56mm	
Matching	*Coarse search*	*Fine search*
Resolution number	3-2	1
Profile search range	21	21
Allowed mode variation	$\pm 1\sigma$	$\pm 2\sigma$
Shape variability	95%	99%
Gaussian kernel width	2mm	2mm
Iterations	100	100

tion [146]. The aligned shape models were then deformed to match the binary images using our 3D-ASM algorithm[1]. Shape model parameters were set to 99.9% of the total variance and $\pm 3\sigma$ along each principal component. These constrains allowed our model to capture fine details of the XCAT phantom geometry.

For the real datasets in group C1 (Section 5.4.2), we enforced topological consistency by obtaining 3D manual segmentations. We used an in-house software and manually deformed our shape model to fit the cardiac boundaries [147]. To initialize the shape model, the observer selected four anatomical landmarks: one in the aortic valve, one in the mitral valve, one in the tricuspid valve, and one in the LV endocardial apex. We registered these initialization points to the corresponding anatomical landmarks in the shape model with a similarity transformation. The shapes were manually deformed by the observer to obtain the manual ground-truth shapes. Note that the shape model constrains were not used to prevent statistical bias.

We trained one intensity model for each landmark of the PDM. The intensity models were independently trained for each cardiac phase. This means that for the simulated datasets we obtained 30 intensity models and for the real datasets we obtained 2 intensity models (ED and ES). The same applies for the reliability thresholds: one threshold per landmark and per phase (Section 5.3).

5.5.3   3D-ASM Segmentation

To run the segmentation on groups V1 and C1, we used the initialization shapes described above (Section 5.5.2). For group C2, initialization shapes were obtained in the same manner as for group C1.

To process the datasets, we used a coarse-to-fine search strategy [148]. It consists on building a multi-resolution pyramid from the original image and processing each level independently. In the coarse levels, we increased the constrains of the model to avoid local minima. In the fine level, we relaxed the constrains to allow for finer details [149]. Table 5.1 summarizes the parameters of our 3D-ASM segmentation approach.

5.6   Experimental Setup

5.6.1   Segmentation Accuracy

- *Simulated vs. real intensity models:* the intensity models were trained both on simulated and real datasets. The simulated intensity models were used to segment the datasets in all test groups (V1, C1 and C2). The real intensity models were used to segment datasets in groups C1 and C2. Datasets in C1 were segmented by means of leave-one-out cross validation. To test performance, we calculated point-to-surface (P2S) errors with respect to the ground-truth meshes/contours described previously (Sec. 5.5.2 and Sec. 5.4.3). Statistical significance was assessed with a Mann-Whitney test [97].

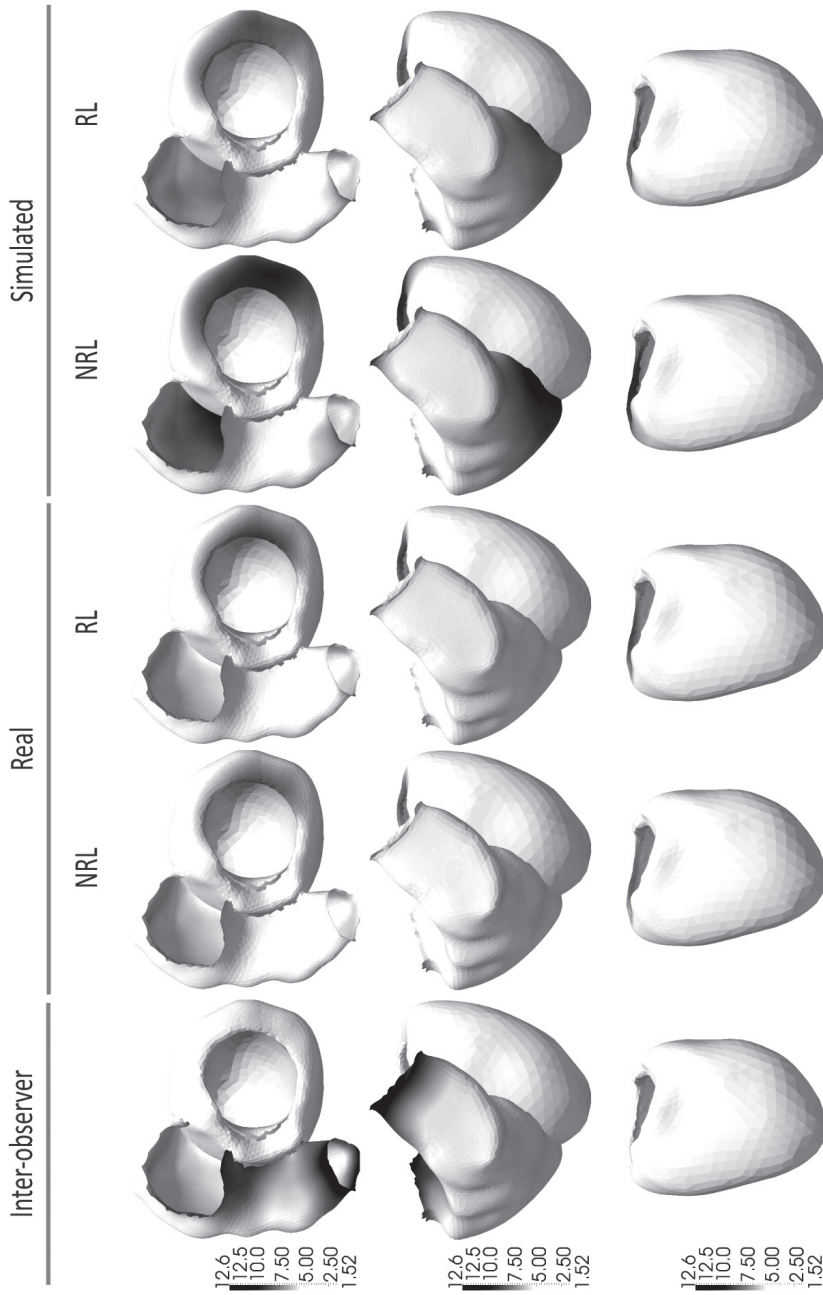[1]We assumed an ideal profile (background=0, myocardium=1) to search for candidate positions.

Figure 5.4: *Average segmentation errors for group C1 (end diastole and end systole). Color-map displayed on the mean shape model with data range from inter-observer values in mm (a). Note the reduction of large errors at the LV base and RV free wall for simulated intensity models with reliability information (d-e). Top view (top), front view (mid) and septal view (bottom). NRL= No reliability; RL= reliability. (See color insert)*

- *Effect of reliability:* we performed the experiment described above with and without reliability information. To include reliability information during matching, each landmark is displaced to a new candidate position only if the Mahalanobis distance is below its corresponding reliability threshold (Sec. 5.3). Therefore, only the landmarks marked as reliable contribute to the deformation of the shape model. We calculated P2S errors and evaluated statistical significance with a Mann-Whitney test.

- *Clinical population subgroups:* to analyze the influence of pathology on segmentation errors, we separated our clinical population in three main groups: *1)* normal, *2)* hypertrophic, and *3)* infarcted and/or with heart failure. We computed the segmentation errors within each of these groups. Statistical significance was assessed with a Mann-Whitney test.

- *Initialization sensitivity:* to test the sensitivity of the segmentation to initialization, we executed the segmentation four times: 1 with favorable and 3 with unfavorable initialization. The favorable initialization shape was obtained as described in Sec. 5.5.2. The unfavorable initialization shapes were obtained by translating the favorable initialization shape. The translation was performed on each axis (x, y, z) by a random factor. The random factors were obtained independently for each axis from a Gaussian distribution with SD equals to $\pm$ 3SD of inter-observer initialization variability (8.07mm). We calculated the ratio of segmentation error with unfavorable initialization over the segmentation error with favorable initialization.

5.6.2   Volume Measurements

We calculated the ground-truth volumes from the ground-truth meshes in group V1 and C1. For group C2, we computed volumes from the ground-truth contours by summing the volume of each slice (area inside contour $\times$ slice thickness). We calculated the measured volumes from the matched meshes in all groups. Relevant parameters were computed: end diastolic volume (EDV), end systolic volume (ESV), ejection fraction (EF) of both ventricles and myocardial mass (MASS) of the LV. Measurement agreement with respect to ground-truth volumes was evaluated with the mean signed difference (*Ground-truth - Measured*) and its corresponding SD.

5.7   Results

5.7.1   Segmentation Accuracy

Visual results of the segmentation for V1, C1 and C2 are displayed in Fig. 5.1, Fig. 5.2 and Fig. 5.3, respectively. Table 5.2 summarizes the P2S errors for all data groups and their corresponding division per pathology. For group V1, we obtained sub-pixel average accuracy (1.42mm). The errors were lowest for the LV endocardium at ED and highest for LV epicardium at ES. For group C1, real intensity models achieved accuracy below inter-observer variability (IV)

for all regions except for RV in ED (5% above). Simulated intensity models achieved accuracy 15% below IV for LV endo and epicardium in ED and for LV endocardium in ES. For RV the obtained accuracy was 30% above IV. On the other hand, the simulated intensity models achieved accuracy above the one obtained with real intensity models by 27% for LV at ED, 55% for LV at ES and 56% for RV at both phases. For group C2, simulated intensity models achieved average accuracy 29% above the one obtained by the real intensity models.

Analyzing each clinical group, we observe that on the normal population of C1, simulated intensity models can segment the LV with average accuracy 17% below IV. For normal and infarcted patients, end systolic RV can be segmented with accuracy 5% below IV. Also for infarcted patients, LV epicardium in ES was segmented by the simulated intensity models with accuracy 13% below the one obtained for other clinical groups. On the normal population of C2, the simulated intensity models can segment the LV with average accuracy of 79% the one obtained by the real intensity models. It is also evident that the hypertrophic group is the most challenging one, specially from population C2. This is understandable since hypertrophic patients can present alterations in shape beyond the bounds of the PDM. Besides the alterations in shape, the myocardial walls often collapse during systole leaving no cavity to be segmented. For this clinical group, the reliability information increased accuracy at ES for both real and simulated intensity models. Examples of each pathology are also included in Fig. 5.2 and Fig. 5.3.

Table 5.2 also shows that including reliability information during the matching process can improve accuracy in ES, noticeable on groups V1 and C1. This is mainly manifested as a reduction of SD in the accuracy measurements.

To have a better understanding of the distribution of outliers, Fig. 5.4 displays average P2S errors for group C1 color-mapped on the mean shape model. In the inter-observer maps, LV outliers are located at the base and slightly at the apex. For RV, outliers are located on the outflow tracks (Fig. 5.4-a). Both for real and simulated intensity models, LV outliers are located at the base and at the apex as well (Fig. 5.4-b). For simulated intensity models, some RV outliers are located on the outflow tracks, while most of them are located along the free wall (Fig. 5.4-d). Note the reduction of outliers for simulated intensity models with reliability information (Fig. 5.4-e).

Table 5.3 summarizes the initialization sensitivity results. It shows that real intensity models are relatively robust to initialization (1%-5% error increase), while simulated intensity models are more sensible to it (5%-19% error increase). This is likely due to the presence of body structures in the real datasets which are absent on the simulated images. Nevertheless, the inclusion of reliability information increased the robustness of real and simulated intensity models, specially on group C2.

TABLE 5.2: Segmentation errors for each clinical subgroup
with *favorable* initialization

					End Diastole						End Systole					
					LV				RV		LV				RV	
					Endo		Epi		Endo		Endo		Epi		Endo	
					mean	SD	mean	SD	mean	SD	mean	SD	mean	SD	mean	SD
		Train	Test	n	mm	mm	mm	mm	mm	mm	mm	mm	mm	mm	mm	mm
Inter-observer			C1	20	2.26	2.12	2.54	2.49	3.02	2.75	3.14	2.83	3.12	3.08	4.67	4.61
All	NRL	sim	V1	400	0.79	0.83	1.51	2.08	1.73	2.35†	1.07	1.26	2.11	2.84	1.51	2.15
		sim	C1	40	1.88	2.23	2.21	2.10	4.56	4.36	2.64	3.13	3.33	3.09	5.27	4.76
		real	C1	40	1.51	1.86†	1.70	2.14†	3.18	4.41†	1.95	2.13†	1.91	2.19†	3.10	3.76
		sim	C2	45	3.64	4.00	3.06	3.10	n.a.	n.a.	4.85	4.63	n.a.	n.a.	n.a.	n.a.
		real	C2	45	2.41	2.42	2.23	2.07	n.a.	n.a.	4.12	2.76	n.a.	n.a.	n.a.	n.a.
	RL	sim	V1	400	0.80	0.83	1.42	1.91	1.73	2.36†	1.04	1.20	1.98	2.68	1.46	2.12
		sim	C1	40	2.37	2.64	2.45	2.54	4.57	4.52	2.67	2.59	3.02	2.64	5.08	4.88
		real	C1	40	1.49	1.75†	1.69	1.92†	3.19	4.19†	1.92	2.00†	1.91	2.07†	3.82	4.11
		sim	C2	45	4.51	4.17	3.38	2.96	n.a.	n.a.	5.23	4.57	n.a.	n.a.	n.a.	n.a.
		real	C2	45	2.59	2.57	2.36	2.19	n.a.	n.a.	4.05	2.96	n.a.	n.a.	n.a.	n.a.
Normal	NRL	sim	C1	12	1.56	1.61	2.17	1.91†	4.43	4.12†	2.33	2.38†	3.29	2.81	4.42	4.01†
		real	C1	12	1.28	1.24†	1.48	1.44†	3.27	4.00†	1.93	2.18†	2.08	2.46†	2.98	3.51
		sim	C2	9	3.15	3.22	2.94	2.59	n.a.	n.a.	3.94	3.35†	n.a.	n.a.	n.a.	n.a.
		real	C2	9	2.60	2.78	2.38	2.37†	n.a.	n.a.	2.87	2.52†	n.a.	n.a.	n.a.	n.a.
	RL	sim	C1	12	1.97	2.18	2.24	2.21†	4.58	4.33†	2.41	2.38†	3.17	2.78	4.36	3.96†
		real	C1	12	1.29	1.31†	1.48	1.47†	3.19	3.92†	1.96	2.17†	2.09	2.43†	3.52	3.71
		sim	C2	9	3.82	3.57	3.17	2.69	n.a.	n.a.	3.82	3.12†	n.a.	n.a.	n.a.	n.a.
		real	C2	9	2.69	2.84	2.45	2.46†	n.a.	n.a.	2.92	2.58†	n.a.	n.a.	n.a.	n.a.
Hypertrophic	NRL	sim	C1	18	2.21	2.78	2.26	2.33	4.73	4.79†	3.00	3.90	3.60	3.61	6.23	5.40
		real	C1	18	1.79	2.39†	1.98	2.75†	3.43	5.17	2.09	2.31†	2.02	2.31†	3.56	4.38
		sim	C2	12	5.72	5.42†	4.06	4.41	n.a.	n.a.	4.36	3.81	n.a.	n.a.	n.a.	n.a.
		real	C2	12	3.03	2.61†	2.82	2.52	n.a.	n.a.	3.26	3.10†	n.a.	n.a.	n.a.	n.a.
	RL	sim	C1	18	2.81	3.08	2.66	2.94	4.75	4.85†	2.98	2.93	3.02	2.81	6.02	5.82
		real	C1	18	1.77	2.16†	1.94	2.35†	3.46	4.72	1.97	2.08†	1.94	2.03†	4.35	4.72
		sim	C2	12	5.38	4.69†	4.20	3.77	n.a.	n.a.	4.59	4.00	n.a.	n.a.	n.a.	n.a.
		real	C2	12	3.11	2.70†	2.90	2.53	n.a.	n.a.	3.36	3.33†	n.a.	n.a.	n.a.	n.a.
Infarcted / HF	NRL	sim	C1	10	1.66	1.54	2.15	1.84†	4.44	3.85	2.33	1.99†	2.88	2.08†	4.67	4.0
		real	C1	10	1.24	1.15†	1.42	1.30†	2.64	3.27†	1.72	1.67†	1.52	1.48	2.45	2.55
		sim	C2	24	3.12	3.41	2.76	2.59	n.a.	n.a.	5.08	4.91	n.a.	n.a.	n.a.	n.a.
		real	C2	24	2.18	2.22	2.00	1.75	n.a.	n.a.	4.39	4.92	n.a.	n.a.	n.a.	n.a.
	RL	sim	C1	10	2.01	2.05	2.30	1.98†	4.24	4.12	2.39	2.04†	2.83	2.11†	4.34	3.72
		real	C1	10	1.23	1.21†	1.46	1.35†	2.70	3.40†	1.77	1.60†	1.66	1.65	3.28	3.23
		sim	C2	24	4.41	4.09	3.16	2.65	n.a.	n.a.	5.58	4.80	n.a.	n.a.	n.a.	n.a.
		real	C2	24	2.40	2.44	2.17	1.96	n.a.	n.a.	3.41	3.21	n.a.	n.a.	n.a.	0.0

LV= left ventricle; RV= right ventricle; SD= standard deviation; HF= Heart Failure;

NRL= no reliability; RL= with reliability; sim = simulated; *n.a.*= not applicable;

NRL errors are significantly different from RL errors unless indicated (†$p > 0.05$).

TABLE 5.3: Ratio of P2S errors with unfavorable/favorable initialization

	Train	Test	n	End Diastole						End Systole					
				LV Endo		LV Epi		RV Endo		LV Endo		LV Epi		RV Endo	
				mean	SD	mean	SD	mean	SD	mean	SD	mean	SD	mean	SD
				mm	mm	mm	mm	mm	mm	mm	mm	mm	mm	mm	mm
NRL	sim	V1	400	1.05	1.18	1.02	1.05	1.05	1.07	1.07	1.17	1.02	1.04	1.08	1.09
	sim	C1	40	1.05	1.05	1.05	1.06	1.06	0.99	1.16	1.24	1.12	1.19	1.05	0.99
	real	C1	40	0.97	0.82	0.95	0.77	1.05	0.93	0.99	0.97	0.99	0.92	1.09	1.04
	sim	C2	45	1.10	1.08	1.27	1.11	*n.a.*	*n.a.*	1.18	1.29	*n.a.*	*n.a.*	*n.a.*	*n.a.*
	real	C2	45	1.06	1.12	1.07	1.09	*n.a.*	*n.a.*	0.92	1.49	*n.a.*	*n.a.*	*n.a.*	*n.a.*
RL	sim	V1	400	1.06	1.20	1.03	1.07	1.05	1.07	1.06	1.15	1.02	1.04	1.08	1.09
	sim	C1	40	1.07	1.10	1.05	1.01	1.07	1.02	1.08	1.20	1.13	1.18	1.12	1.04
	real	C1	40	0.98	0.89	0.98	0.89	1.02	0.97	1.01	1.00	1.02	1.00	1.07	1.00
	sim	C2	45	1.18	1.14	1.15	1.17	*n.a.*	*n.a.*	1.07	1.01	*n.a.*	*n.a.*	*n.a.*	*n.a.*
	real	C2	45	1.00	1.04	1.01	1.03	*n.a.*	*n.a.*	0.86	1.16	*n.a.*	*n.a.*	*n.a.*	*n.a.*

All abbreviations as in Table 5.2.

TABLE 5.4: Volume measurements: mean signed difference

	Train	Test	n	LV EDV		LV ESV		LV EF		LV MASS		RV EDV		RV ESV		RV EF	
				MSD	SD	MSD	SD	MSD	SD	MSD	SD	MSD	SD	MSD	SD	MSD	SD
				ml	ml	ml	ml	%	%	gr	gr	ml	ml	ml	ml	%	%
Inter-observer		C1	20	-9.26	11.19	-11.19	15.53	5.09	12.23	-2.52	14.58	-19.42	19.60	-34.58	32.13	15.06	17.73
NRL	sim	V1	400	-0.30	5.20	-0.29	3.07	0.65	3.33	-0.69	7.38	-0.68	7.54	-0.23	9.52	1.53	9.03
	sim	C1	40	1.67	15.52	-4.25	23.61	4.52	22.76	-31.57	18.51	-2.59	30.27	-25.49	46.13	20.19	32.13
	real	C1	40	1.39	12.91	-6.01	9.73	5.23	8.99	4.12	16.99	23.35	27.87	3.67	19.96	8.85	11.93
	sim	C2	45	39.99	37.45	31.59	27.76	-4.98	14.60	-38.55	49.07	*n.a.*	*n.a.*	*n.a.*	*n.a.*	*n.a.*	*n.a.*
	real	C2	45	28.50	32.48	22.46	41.83	2.34	32.85	-10.30	30.21	*n.a.*	*n.a.*	*n.a.*	*n.a.*	*n.a.*	*n.a.*
RL	sim	V1	400	1.15	5.35	0.88	3.23	-0.26	3.13	1.92	7.82	0.52	7.73	0.27	9.73	1.93	9.05
	sim	C1	40	7.50	16.56	-0.27	12.05	3.49	13.52	-19.02	20.86	23.83	28.31	-14.84	42.65	27.07	35.02
	real	C1	40	0.11	12.04	-7.32	9.61	5.78	9.16	4.43	16.77	20.58	28.09	-5.86	23.45	16.11	16.31
	sim	C2	45	54.49	38.47	31.93	35.79	1.13	11.03	-44.87	50.59	*n.a.*	*n.a.*	*n.a.*	*n.a.*	*n.a.*	*n.a.*
	real	C2	45	31.64	32.27	14.16	35.02	6.77	34.10	-11.45	30.25	*n.a.*	*n.a.*	*n.a.*	*n.a.*	*n.a.*	*n.a.*

LV= left ventricle; RV= right ventricle; EDV= end diastolic volume; ESV= end systolic volume;

EF= ejection fraction; MSD= mean signed difference; Other abbreviations as in Table 5.2.

5.7.2   Volume Measurements

Table 5.4 summarizes the volume measurement analysis. For group C1, the discrepancies on LV volume measurements are within the limits of IV (10ml for volumes and 5% for EF). LV MASS was overestimated above IV limits. This is most likely due to the large segmentation errors on hypertrophic patients. The error was substantially reduced in the segmentation including reliability information. Regardless of the large segmentation errors for RV, volume measurements were below the bounds of IV. The measurement of EF was underestimated by the simulated models beyond the bounds of IV. For group C2, the overestimation of volume might be due to difference on volume measurement (3D vs. 2D approach). This effect was also observed in other 3D approaches during the segmentation challenge, and it applies to EDV, ESV, and LV MASS [145,150]. The overestimation was compensated in the calculation of EF.

5.8   Discussion

5.8.1   Evidence for Hypothesis 1 - *an intensity model trained with simulated images can obtain segmentation accuracy comparable to inter-observer variability*

Our first hypothesis mainly holds true for the LV. As for the RV, the segmentation accuracy with simulated intensity models was comparable to IV only at ES. This was particularly noticeable on normal and infarcted patients. Taking a closer look at the simulated images, we can observe that the RV model seems oversimplified. On the one hand, it still lacks RV papillary muscles making the cavity more even than in real images. On the other hand, the anterolateral wall changes diameter rather rapidly generating extremely blurred edges. This effect is less noticeable at ES, where the wall thickens and partial volume effect is reduced. It is also less noticeable along the posterior wall due to its smoother change of diameter. This drawback can be improved either by: *1)* modifying the geometry of the phantom to provide a smoother transition towards the apex and/or increasing the wall thickness of the RV model; *2)* simulating thinner MRI slices to reduce partial volume effect. We chose not to explore the second option in this work to maintain consistency of MRI acquisition parameters between our real and simulated datasets.

   With respect to the LV model, it would be interesting to include in the phantom geometrical alterations due to pathology, since the appearance of the profiles are evidently affected by them. For instance, a chronic infarction makes the walls thinner while a hypertrophy makes the walls thicker. Besides the alteration of the profiles, the pathology can also modify the overall shape of the ventricles and the relationship between them. Therefore, a specific PDM per pathology can also greatly improve segmentation accuracy. This will require, as well, an automatic technique to select the proper PDM when processing a new case.

   As for the location of outliers, both the base and the apex are known to be challenging areas. First, the correct definition of the basal plane is a known

TABLE 5.5: Segmentation errors of other model-based cardiac MRI segmentation studies (in works with multiple modalities only MRI data is reported)

Author	n (Nor/Path)	Population	Resolution (mm^3)	Stack	Regions	Phase	LV Endo		LV Epi		RV Endo	
							mean mm	SD mm	mean mm	SD mm	mean mm	SD mm
van Assen et al. [62]	15 (15)	Nor	1.50×1.50×6.0	SA	LV	ED	1.72	n.a.	1.55	n.a.	n.a.	n.a.
Löetjöenen et al. [144]	40 (15/14/11)	Nor/Isch/Dil	1.50×1.50×7.1	SA/LA	LV/RV	ED/ES	1.54	0.39	1.47	0.34	2.37	0.65
Koikkalainen et al. [151]	25 (25/0)	Nor	1.20×1.20×6.5	SA/LA	WH	ED	1.46	0.30	1.87	0.63	2.26	0.46
Zhang et al. [142]	50 (25/25)	Nor/TOF	1.70×1.70×7.0	SA/LA	LV/RV	4D	1.69	0.38	1.89	0.49	2.53	0.56‡
Peters et al. [61]	42 (n.a.)	Mixed	0.60×0.60×0.8	3D	WH	ED	0.69	1.13	0.83	1.17	0.74	0.96
Zhuang et al. [143]	37 (18/19)	Nor/Mixed	1.00×1.00×1.0	3D	WH	ED	1.47	0.32	2.32	0.82	2.13	0.70
Our approach	40 (12/18/10)	Nor/Hyp/Isch	1.56×1.56×8.0	SA	LV/RV	ED/ES	1.73	2.00	1.80	2.17	3.14	4.08

LV= Left ventricle; RV= Right ventricle; SD= Standard deviation; Nor= Normal; Path= Pathologic; Isch= Ischemic; Dil= Dilated;

TOF= Tetralogy of Fallot; Hyp= Hypertrophy; SA= Short-axis; LA= Long-axis; WH= Whole heart; ‡= epicardium;

complication of cardiac imaging postprocessing for most modalities. Second, the boundaries at the apex are specially blurred due to high density of trabeculae. Both of these difficulties can be greatly improved by including long-axis images in the matching process. In this type of images, the base and apex are clearly visible.

5.8.2   Evidence for Hypothesis 2- *including a measure of reliability during the matching process can increase robustness*

Our second hypothesis mainly holds true for the simulated intensity profiles. The real intensity profiles proved to be robust enough on their own. Possibly, since the real images already include everything that could draw the model away from the true boundary. For the simulated intensity models, reliability not only increases robustness, it may also increase accuracy. This was noticeable for LV epicardium and RV at ES. In general, the inclusion of reliability made the segmentation based on simulated intensity models less sensitive to initialization. Reliability also reduced outliers in end systolic volumes and LV mass computation.

We can conclude that in the presence of clear edges, the segmentation without reliability draws the model to a correct position. When the edges are less clear, like in the epicardium or in severe hypertrophy, the reliability information helps the model stay in a more correct position.

5.8.3   Comparison to Previous Relevant Studies

Table 5.5 summarizes the segmentation errors of other model-based cardiac MRI segmentation approaches. Given that comparisons across studies are difficult since datasets are different (i.e. type of patients, number of cardiac phases, image quality, image resolution), our purpose is to identify consistent trends. In general, endocardial errors tend to be the smallest, followed by the epicardial ones, and RV errors tend to be the largest. We also observed that trend in our work. For most studies, at least half of their database is comprised by normal subjects. In our study only 30% of datasets corresponded to normal subjects, which most likely contributed to the inaccuracies. The performance of model-based approaches on hypertrophic patients seems understudied in the literature. We found in our work, including 45% of hypertrophic patients, that this pathology poses a special challenge to our model-based segmentation approach.

5.9   Conclusion and Future work

In this work, we tested the ability of intensity models trained on simulated MRI datasets to segment the ventricular cavities from real datasets. A motivation to train intensity models from simulated datasets is to be able to handle multimodal datasets more efficiently. Another motivation is to avoid the need for manual outlining, because it is very laborious and very expert dependant. The

accuracy obtained by the simulated intensity models was compared to the one obtained by real intensity models and to inter-observer variability.

We can conclude the following: if the proper ground-truth meshes (with point correspondence) are available, this dataset is ideal for intensity model training since they perform with good accuracy and robustness. If, in the other hand, no such dataset is available, training the intensity models on simulated data can achieve accuracy below inter-observer variability (mainly for the left ventricle). The right ventricular model of the simulated images needs further improvement to generate proper profiles around the myocardial edges.

We also tested how the inclusion of reliability information during the matching process can increase robustness. Reliability information was also obtained from the simulated datasets. It proved to increase robustness of the segmentation process making it less sensible to initialization and reducing the outliers in difficult areas.

Future work should target the incorporation of long-axis information during training and matching for a better segmentation of the base and apex. Another factor that needs to be tackled is the correction for z-shift due to respiration. While currently it is handled by the statistical constrains of the PDM, a correction of this artifact can aid the segmentation. Finally, building a specific PDM per pathology, alongside with an automatic technique to select the proper PDM, should benefit the segmentation in cases of severe hypertrophy and infarction.

6

General Conclusions

6.1   Overview

The work developed in this thesis was motivated by the clinical challenge to handle large amounts of multimodal data. This challenge is typically found in the cardiovascular care cycle. As mentioned in Chapter 1, to tackle this challenge we require an approach that:

- is able to accurately segment the cardiac cavities from multimodal datasets

- provides a unified frame of reference to integrate multiple information sources

- aids the classification of a patient's cardiac condition

This thesis builds upon the idea that statistical shape models, in particular Active Shape Models, are a robust and accurate approach with the potential to incorporate all these requirements. The use of a statistical model-based approach provides a way to unify multiple sources of data in a unique frame of reference (i.e. atlas). The proposed approach decouples the shape information from the appearance information. On the one hand, the shape information is trained from high-resolution CT datasets. On the other hand, the appearance information is obtained for each modality by simulating the physics of acquisition. We tested the proposed approach in two major modalities: SPECT and MRI. Implementation and evaluation details can be found in Chapter 3-Chapter 5. For both modalities, the constructed models were tested on virtual and clinical datasets. The automatically built 3D-ASM were able to segment the left ventricular cavity below inter-observer variability.

We hereby complete the automatic 3D-ASM construction pipeline including: *1)* the autolandmarking method by Frangi *et al.* [56], *2)* the automatic PDM generation method by Ordas *et al.* [59] and Hoogendoorn *et al.* [64], and *3)* the automatic construction of intensity models method by Tobon-Gomez *et al.* [46].

6.2   Outlook

A complete pipeline to automatically train 3D-ASM brings several advantages. Let us review some of them:

6.2.1   Efficient Handling of Multimodal Datasets

Multimodal imaging is a fast gowning field. In fact, efforts to build devices which are multimodal in nature are increasing enormously. Their basic concept is to combine a modality with high spatio-temporal resolution with a modality with molecular specificity (i.e. SPECT/CT, PET/CT, PET/MRI). Although mainly targeted to cancer research, their working principles are applicable to other pathologies. This highlights the importance of a multimodal approach, like the one developed along the scope of this thesis. Given that our segmentation approach is based on the same methodology for different modalities, the information retrieved can be considered comparable. This eases up the integration and subsequent visualization of functional information.
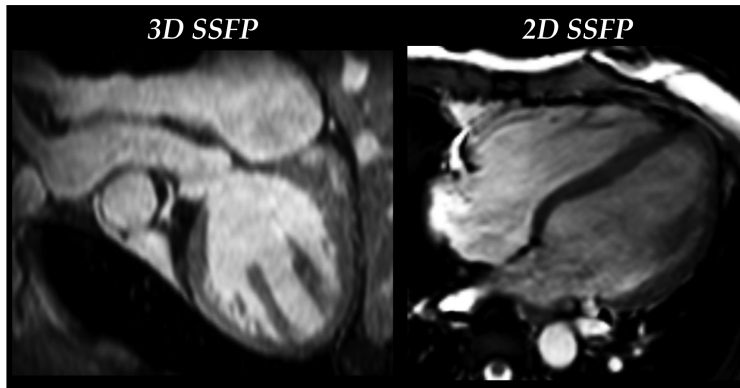
Figure 6.1: *MRI images acquired with a 3D isotropic SSFP sequence (coronal view) and a 2D non-isotropic SSFP sequence (long-axis view). Both images belong to the same subject.*

6.2.2 Intensity Model Update

We can identify two main scenarios that can modify the intensity distributions of cardiac images: *1)* acquisition parameters are modified to visualize a specific physiological phenomena, and, *2)* acquisition devices are able to produce datasets with higher spatial and/or temporal resolution due to technical upgrades. A classical example of scenario *1* is a late gadolinium enhancement MRI sequence in which myocardium appears darker than in a SSFP sequence (see Fig. 1.4). An example of scenario *2* is found with the new SPECT/CT devices. Low-dose CT images are used to improve tomographic reconstruction of SPECT datasets obtaining images with higher spatial resolution and reduced noise. Another example is the 3D isotropic MRI acquisition recently implemented by Uribe *et al.* [11]. Such a sequence modifies the blood/myocardium contrast and sharpens the edges (see Fig.6.1). In all these cases, being able to retrain the intensity models to handle the new appearance of the datasets is highly desirable.

6.2.3 Population of Virtual Subjects

With the statistical information encoded in the PDM of the 3D-ASM approach, we can generate a population of virtual subjects. This can be interesting from several points of view: *1)* to generate a large imaging database to train post-processing algorithms, *2)* to create extreme anatomical variants, such as small or big hearts, and, *3)* to run a parametric study with uniformly distributed anatomies, thus ensuring that all the shape space is represented in our database.

6.3 Research Opportunities

The information to potentially integrate in a computational model is not limited to classical functional parameters. As research advances, novel functional
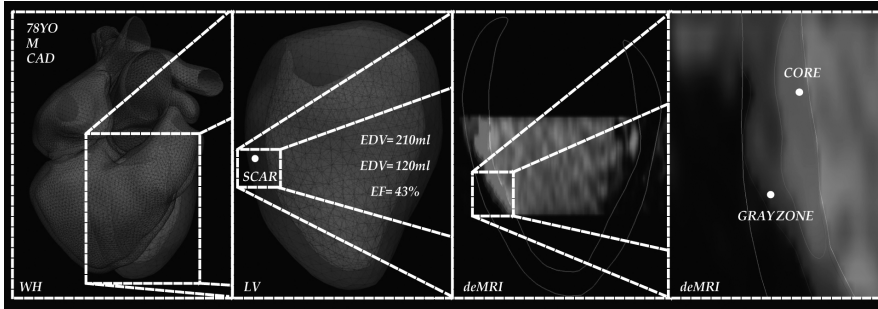
Figure 6.2: *Illustration of a multilevel computational model: the anatomical geometry is complemented with functional information at different levels. WH= Whole heart; LV= Left Ventricle; EDV= End diastolic volume; ESV= End systolic volume; EF= Ejection fraction; deMRI= Delayed enhancement Magnetic Resonance Imaging; Core= Infarct core; Gray Zone= Area peripheral to the core. (See color insert)*

parameters are proposed. Most likely, those parameters will be quantifiable from a retrospective population of patient-specific computational models.

Such a computational model is a perfect candidate to provide an integrative frame of reference to enrich electrophysiological simulations. Besides providing patient specific anatomy, it can provide complementary functional information (i.e. scar) and *ex-vivo* information (i.e. fiber orientation) to constrain the simulations. Another research opportunity can be targeted to comparing population subgroups. Building a statistical model of population subgroups allows for comparing them among each other. For instance, the shape and/or deformation patterns of a normal population can be compared to the patterns of a hypertrophic population. A measure of distance from normality can be used as a quantifiable parameter specific to a pathology. Other clear opportunity comes from cardiac remodeling research. The information gathered at different stages of a CVD can be displayed in a computational model. Ideally, the clinician could navigate through the multiple computational models, each representing a point in time, and observe the development of the disease. This scheme could also be used for evaluation of cardiac surgery outcome, by visualizing pre and posttreatment models. Finally, surgical procedures (i.e. ablation and CRT) can be aided by the use a patient-specific computational model. The preoperative model can be used to optimally plan the treatment and to guide the procedure with intraoperative information. This presents a wide range of opportunities along the footsteps towards a multilevel computational model of the heart (see Fig. 6.2).

List of Publications

Peer reviewed papers in international journals

- **C. Tobon-Gomez**, F. M. Sukno, C. Butakoff, M. Huguet, A. F. Frangi. Automatic Training and Reliability Estimation for 3D-ASM Applied to Cardiac MRI Segmentation. (submitted)

- **C. Tobon-Gomez**, F. M. Sukno, B. H. Bijnens, M. Huguet, A. F. Frangi. Realistic Simulation of CMR Studies Modeling Anatomical Variability, Trabeculae and Papillary Muscles. *Magn Res Med* 65: 280–288 (2011)

- **C. Tobon-Gomez**, C. Butakoff, S. Aguade, F. M. Sukno, G. Moragas, A. F. Frangi. Automatic Construction of 3D-ASM Intensity Models by Simulating Image Acquisition: Application to Myocardial Gated SPECT Studies. *IEEE Trans Med Imaging* 27(11): 1655–1667 (2008)

- G. Avegliano, M. Huguet, J. P. Costabel, R. Ronderos, B. H. Bijnens, P. Kuschnir, J. Thierer, **C. Tobon-Gomez**, G. O. Martinez, and A. F. Frangi. Morphologic Pattern of Late Gadolinium Enhancement in Takotsubo Cardiomyopathy Detected by Early Cardiovascular Magnetic Resonance. *Clin Cardiol*, 34(3): 178–182 (2011)

- G. Piella, M. De Craene, B. H. Bijnens, **C. Tobon-Gomez**, M. Huguet, G. Avegliano, A. F. Frangi. Characterization of Myocardial Deformation in Patients with Left Ventricular Hypertrophy of Different Etiologies Using Strain Distribution obtained by MRI. *Rev Esp Cardiol* 63: 1281–1291 (2010)

- M. Huguet, **C. Tobon-Gomez**, B. H. Bijnens, A. F. Frangi, M. Petit. Cardiac Injuries in Blunt Chest Trauma: Case Report. *J Cardiovasc Magn Res* 11(1): 35 (2009)

Book chapters

- **C. Tobon-Gomez**, S. Ordas, S. Aguade, J. Castell and A. F. Frangi. Statistical Deformable Models for Cardiac Segmentation and Functional Analysis in Gated-SPECT Studies. In J.S. Suri and A. Farag, editor, *Deformable Models: Biomedical and Clinical Applications (Topics in Biomedical Engineering. International Book Series)*, volume 1, pages 163–193. Springer-Verlag New York, Inc., Mar 2007.

Peer reviewed papers in conferences proceedings

- **C. Tobon-Gomez**, C. Butakoff, P. Yushkevich, M. Huguet, A. F. Frangi. 3D Mesh Based Wall Thickness Measurement: Identification of Left Ventricular Hypertrophy Phenotypes. In *IEEE Engineering in Medicine and Biology Society*, p. 2642–2645; Buenos Aires, Argentina, 2010.

- **C. Tobon-Gomez**, F. M. Sukno, C. Butakoff, M. Huguet, A. F. Frangi. Simulation of Late Gadolinium Enhancement Cardiac Magnetic Resonance Studies. In *IEEE Engineering in Medicine and Biology Society*, p. 1469–1472; Buenos Aires, Argentina, 2010.

- **C. Tobon-Gomez**, F. M. Sukno, B. H. Bijnens, M. Huguet, A. F. Frangi. Realistic Simulation of Local Image Appearance of Cardiac Magnetic Resonance Imaging Using a Virtual Phantom Population. In *MICCAI Workshop on Cardiovascular Interventional Imaging and Biophysical Modelling*, p. 132–140; London, United Kingdom, 2009.

- **C. Tobon-Gomez**, B. H. Bijnens, M. Huguet, F. M. Sukno, G. Moragas, A. F. Frangi. Systolic and Diastolic Assessment by 3D-ASM Segmentation of gated-SPECT Studies: A Comparison with MRI. In *SPIE Medical Imaging 2009: Biomedical Applications in Molecular, Structural, and Functional Imaging*, volume 7262, p. 726227; Orlando, USA, 2009.

- **C. Tobon-Gomez**, C. Butakoff, S. Ordas, S. Aguade, A. F. Frangi. Comparative Study of Diversely Trained 3D-ASM Models for Segmentation of Gated SPECT Data. In *SPIE Medical Imaging: Physiology, function, and structure from medical images*, volume 6511, p. 65112G; San Diego, USA, 2007.

- M. De Craene, F. M. Sukno, **C. Tobon-Gomez**, C. Butakoff, R. M. Figueras I Ventura, C. Hoogendoorn, G. Piella, N. Duchateau, E. Muñoz-Moreno, R. Sebastian, O. Camara, A. F. Frangi. Atlas Construction and Image Analysis Using Statistical Cardiac Models. In *Statistical Atlases and Computational Models of the Heart STA-COM workshop at MICCAI*, Lecture Notes in Computer Science, volume 6364, p. 1–13; Beijing, China, 2010.

- H. Sun, A. F. Frangi, H. Wang, F. M. Sukno, **C. Tobon-Gomez**, P. Yushkevich. Automatic Cardiac MRI Segmentation Using a Biventricular Deformable Medial Model. In *Medical Image Computing and Computer-Assisted Intervention*, Lecture Notes in Computer Science, volume 6361, p. 468–475; Beijing, China, 2010.

- H. Sun, **C. Tobon-Gomez**, S. Das, M. Huguet, P. Yushkevich, A. F. Frangi. Ventricular Wall Thickness Analysis in Acute Myocardial Infarction and Hypertrophic Cardiomyopathy. In *IEEE International Symposium on Biomedical Imaging*, Boston, USA, 2009.

Abstracts in conferences proceedings

- G. Piella, M. De Craene, B. H. Bijnens, **C. Tobon-Gomez**, M. Huguet, A. F. Frangi. The Use of Strain Distribution from MRI Tagging to Evaluate Deformation in Hypertrophic Cardiomyopathies. In *Annual Meeting of the European Association of Echocardiography*, Madrid, Spain, 2009.

- M. Huguet, **C. Tobon-Gomez**, A. Pijuan, L. Dos, A. Mallol, M.Petit, J. Casaldaliga. Congenital Heart Disease In Adulthood: Usefulness Of Cardiac Magnetic Resonance Imaging. In *Annual Meeting of North American Society for Cardiac Imaging–NASCI*, Orlando, USA, 2009.

- G. Avegliano, M. Huguet, P. Kuschnir, J. Thierer, **C. Tobon-Gomez**, D. Capdeferro, C. Butakoff, A. F. Frangi, M. Petit, R. Ronderos. Utility of the Real Time 3D Echocardiography for Assessment of Left Ventricular Mass in Patients with Hypertrophic Cardiomyopathy: Comparison with Cardiac Magnetic Resonance. In *World Congress of Cardiology*, Buenos Aires, Argentina, May 2008.

- S. Ordas, **C. Tobon-Gomez**, C. Moure, M. Huguet, and A. F. Frangi. Automatic Assessment of Left Ventricular Contraction Synchronicity in Cine MRI Studies. In *ISMRM 14th Scientific Meeting*, Seattle, USA, 2006.

Acknowledgements

Biography

Catalina Tobon-Gomez has a Biomedical Engineering background. She obtained her Bachelors degree from Antioquia's Engineering School, Colombia, in 2005. During 2004, as part of her undergraduate studies, she visited the Bioinstrumentation Laboratory in Massachusetts Institute of Technology (MIT) for an internship. After graduation, she traveled to Barcelona to join CISTIB as a researcher. Since then, her main research line has been multimodal cardiac imaging analysis. From years 2007 to 2009, she took a part time research appointment in a clinical center (CETIR Sant Jordi). In early 2011, she completed a research stay in King's College London. Thanks to these experiences, she increased her understanding of cardiac MRI acquisition and analysis.

Bibliography

[1] J. Bogaert, "Cardiac function," in *Clinical Cardiac MRI*, ser. Medical Radiology, J. Bogaert, S. Dymarkowski, and A. Taylor, Eds.   Springer Berlin Heidelberg, 2005, pp. 99–141.

[2] C. C. Moore, C. H. Lugo-Olivieri, E. R. McVeigh, and E. A. Zerhouni, "Three-dimensional systolic strain patterns in the normal human left ventricle: characterization with tagged mr imaging." *Radiology*, vol. 214, no. 2, pp. 453–466, Feb 2000.

[3] W. J. Paulus, C. Tschöpe, J. E. Sanderson, C. Rusconi, F. A. Flachskampf, F. E. Rademakers, P. Marino, O. A. Smiseth, G. D. Keulenaer, A. F. Leite-Moreira, A. Borbély, I. Edes, M. L. Handoko, S. Heymans, N. Pezzali, B. Pieske, K. Dickstein, A. G. Fraser, and D. L. Brutsaert, "How to diagnose diastolic heart failure: a consensus statement on the diagnosis of heart failure with normal left ventricular ejection fraction by the Heart Failure and Echocardiography Associations of the European Society of Cardiology," *Eur Heart J*, vol. 28, no. 20, pp. 2539–2550, Oct 2007.

[4] C. Akincioglu, D. S. Berman, H. N. P. B. Kavanagh, P. J. Slomka, A. Abidov, S. Hayes, J. D. Friedman, and G. Germno, "Assessment of diastolic function using 16-frame 99mTc-sestamibi gated myocardial perfusion SPECT: Normal values," *J Nucl Med*, vol. 46, pp. 1102–8, 2005.

[5] M. Motoyasu, T. Kurita, K. Onishi, S. Uemura, T. Tanigawa, T. Okinaka, K. Takeda, T. Nakano, M. Ito, and H. Sakuma, "Correlation between late gadolinium enhancement and diastolic function in hypertrophic cardiomyopathy assessed by magnetic resonance imaging," *Circ J*, vol. 72, no. 3, pp. 378–383, 2008.

[6] R. O. Bonow, B. A. Carabello, C. Kanu, A. C. de Leon, D. P. Faxon, M. D. Freed, W. H. Gaasch, B. W. Lytle, R. A. Nishimura, P. T. O'Gara, R. A. O'Rourke, C. M. Otto, P. M. Shah, J. S. Shanewise, S. C. Smith, A. K. Jacobs, C. D. Adams, J. L. Anderson, E. M. Antman, D. P. Faxon, V. Fuster, J. L. Halperin, L. F. Hiratzka, S. A. Hunt, B. W. Lytle, R. Nishimura, R. L. Page, and B. Riegel, "ACC/AHA 2006 guidelines for the management of patients with valvular heart disease: a report of the American College of Cardiology/American Heart Association," *Circulation*, vol. 114, no. 5, pp. e84–231, Aug 2006.

[7] P. E. Vardas, A. Auricchio, J.-J. Blanc, J.-C. Daubert, H. Drexler, H. Ector, M. Gasparini, C. Linde, F. B. Morgado, A. Oto, R. Sutton, and M. Trusz-Gluza, "Guidelines for cardiac pacing and cardiac resynchronization therapy of the European Society of Cardiology in collaboration with the European Heart Rhythm Association," *Europace*, vol. 9, no. 10, pp. 959–998, Oct 2007.

[8] K. Dickstein, A. Cohen-Solal, G. Filippatos, J. J. V. McMurray, P. Ponikowski, P. A. Poole-Wilson, A. Strömberg, D. J. van Veldhuisen, D. Atar, A. W. Hoes, A. Keren, A. Mebazaa, M. Nieminen, S. G. Priori, K. Swedberg, E. S. C. C. for Practice Guidelines, A. Vahanian, J. Camm, R. D. Caterina, V. Dean, K. Dickstein, G. Filippatos, C. Funck-Brentano, I. Hellemans, S. D. Kristensen, K. McGregor, U. Sechtem, S. Silber, M. Tendera, P. Widimsky, J. L. Zamorano, D. Reviewers, M. Tendera, A. Auricchio, J. Bax, M. Böhm, U. Corrà, P. D. Bella, P. M. Elliott, F. Follath, M. Gheorghiade, Y. Hasin, A. Hernborg, T. Jaarsma, M. Komajda, R. Kornowski, M. Piepoli, B. Prendergast, L. Tavazzi, J.-L. Vachiery, F. W. A. Verheugt, J. L.

Zamorano, and F. Zannad, "ESC guidelines for the diagnosis and treatment of acute and chronic heart failure 2008 of the European Society of Cardiology developed in collaboration with the Heart Failure Association and endorsed by the European Society of Intensive Care Medicine," *Eur Heart J*, vol. 29, no. 19, pp. 2388–2442, Oct 2008.

[9] R. J. Gibbons, P. A. Araoz, and E. E. Williamson, "The year in cardiac imaging." *J Am Coll Cardiol*, vol. 55, no. 5, pp. 483–495, Feb 2010.

[10] M. Habis, A. Capderou, A. Sigal-Cinqualbre, S. Ghostine, S. Rahal, J. Y. Riou, P. Brenot, C. Y. Angel, and J. F. Paul, "Comparison of delayed enhancement patterns on multislice computed tomography immediately after coronary angiography and cardiac magnetic resonance imaging in acute myocardial infarction," *Heart*, vol. 95, no. 8, pp. 624–629, 2009.

[11] S. Uribe, V. Muthurangu, R. Boubertakh, T. Schaeffter, R. Razavi, D. L. Hill, and M. S. Hansen, "Whole-heart cine MRI using real-time respiratory self-gating," *Magn Res Med*, vol. 57, no. 3, pp. 606–613, 2007.

[12] A. K. Rutz, S. Ryf, S. Plein, P. Boesiger, and S. Kozerke, "Accelerated whole-heart 3D CSPAMM for myocardial motion quantification." *Magn Res Med*, vol. 59, no. 4, pp. 755–763, Apr 2008.

[13] A. Frydrychowicz, C. J. François, and P. A. Turski, "Four-dimensional phase contrast magnetic resonance angiography: Potential clinical applications," *Eur J Radiol*, vol. In Press, Corrected Proof, pp. –, 2011.

[14] M. Markl, P. J. Kilner, and T. Ebbers, "Comprehensive 4D velocity mapping of the heart and great vessels by cardiovascular magnetic resonance." *J Cardiovasc Magn Res*, vol. 13, p. 7, 2011.

[15] A. Lutz, A. Bornstedt, R. Manzke, P. Etyngier, G. U. Nienhaus, and V. Rasche, "Acceleration of tissue phase mapping by k-t BLAST: a detailed analysis of the influence of k-t-blast for the quantification of myocardial motion at 3t." *J Cardiovasc Magn Res*, vol. 13, p. 5, 2011.

[16] N. Toussaint, M. Sermesant, C. T. Stoeck, S. Kozerke, and P. G. Batchelor, "In vivo human 3D cardiac fibre architecture: reconstruction using curvilinear interpolation of diffusion tensor images." *Med Imag Comput & Comput-Assist Intervention*, vol. 13, no. Pt 1, pp. 418–425, 2010.

[17] V. L. Roger, A. S. Go, D. M. Lloyd-Jones, R. J. Adams, J. D. Berry, T. M. Brown, M. R. Carnethon, S. Dai, G. de Simone, E. S. Ford, C. S. Fox, H. J. Fullerton, C. Gillespie, K. J. Greenlund, S. M. Hailpern, J. A. Heit, P. M. Ho, V. J. Howard, B. M. Kissela, S. J. Kittner, D. T. Lackland, J. H. Lichtman, L. D. Lisabeth, D. M. Makuc, G. M. Marcus, A. Marelli, D. B. Matchar, M. M. McDermott, J. B. Meigs, C. S. Moy, D. Mozaffarian, M. E. Mussolino, G. Nichol, N. P. Paynter, P. D. Sorlie, R. S. Stafford, T. N. Turan, M. B. Turner, N. D. Wong, and J. Wylie-Rosett, "Heart disease and stroke statistics–2011 update: a report from the American Heart Association," *Circulation*, vol. 123, no. 4, pp. e18–e209, Feb 2011.

[18] W. J. M. Scholte op Reimer, A. K. Gitt, E. Boersma, and M. L. Simoons, "Cardiovascular Diseases in Europe. Euro Heart Survey – 2006," *Sophia Antipolis. European Society of Cardiology*, 2006.

[19] S. Dymarkowski, J. Bogaert, and Y. Ni, "Ischemic heart disease," in *Clinical Cardiac MRI*, ser. Medical Radiology, J. Bogaert, S. Dymarkowski, and A. M. Taylor, Eds. Springer Berlin Heidelberg, 2005, pp. 173–216.

[20] B. J. Maron, J. A. Towbin, G. Thiene, C. Antzelevitch, D. Corrado, D. Arnett, A. J. Moss, C. E. Seidman, and J. B. Young, "Contemporary definitions and classification of the cardiomyopathies: an American Heart Association scientific statement from the council on clinical cardiology, heart failure and transplantation committee; quality of care and outcomes research and functional genomics and translational biology interdisciplinary working groups; and council on epidemiology and prevention," *Circulation*, vol. 113, no. 14, pp. 1807–1816, Apr 2006.

[21] B. J. Maron, "Hypertrophic cardiomyopathy: a systematic review." *J Am Coll Cardiol*, vol. 287, no. 10, pp. 1308–1320, Mar 2002.

[22] J. Bogaert and A. Taylor, "Nonischemic myocardial disease," in *Clinical Cardiac MRI*, ser. Medical Radiology, J. Bogaert, S. Dymarkowski, and A. Taylor, Eds. Springer Berlin Heidelberg, 2005, pp. 217–270.

[23] J. I. E. Hoffman and S. Kaplan, "The incidence of congenital heart disease." *J Am Coll Cardiol*, vol. 39, no. 12, pp. 1890–1900, Jun 2002.

[24] M. Cikes, B. Bijnens, Z. Duric, M. L. Bencic, I. Gosev, V. Velagic, H. Gasparovic, D. Milicic, and B. Biocina, "Detecting volume responders prior to implantation of a cardiac resynchronization therapy device via minithoracotomy: the septal flash as a predictor of immediate left ventricular reverse remodeling," *Heart Surg Forum*, vol. 12, no. 6, pp. E362–E367, Dec 2009.

[25] European Society of Cardiology/American College of Cardiology Committee, "Myocardial infarction redefined–a consensus document for the redefinition of myocardial infarction," *Eur Heart J*, vol. 21, pp. 1502–1513, 2000.

[26] E. M. Antman, D. T. Anbe, P. W. Armstrong, E. R. Bates, L. A. Green, M. Hand, J. S. Hochman, H. M. Krumholz, F. G. Kushner, G. A. Lamas, C. J. Mullany, J. P. Ornato, D. L. Pearle, M. A. Sloan, S. C. S. Jr, J. S. Alpert, J. L. Anderson, D. P. Faxon, V. Fuster, R. J. Gibbons, G. Gregoratos, J. L. Halperin, L. F. Hiratzka, S. A. Hunt, A. K. Jacobs, and J. P. Ornato, "ACC/AHA guidelines for the management of patients with ST-elevation myocardial infarction: a report of the American College of Cardiology/American Heart Association," *J Am Coll Cardiol*, vol. 44, no. 3, pp. E1 – E211, 2004.

[27] J. L. Anderson, C. D. Adams, E. M. Antman, C. R. Bridges, R. M. Califf, D. E. Casey, W. E. Chavey, F. M. Fesmire, J. S. Hochman, T. N. Levin, A. M. Lincoff, E. D. Peterson, P. Theroux, N. K. Wenger, R. S. Wright, S. C. Smith, A. K. Jacobs, C. D. Adams, J. L. Anderson, E. M. Antman, J. L. Halperin, S. A. Hunt, H. M. Krumholz, F. G. Kushner, B. W. Lytle, R. Nishimura, J. P. Ornato, R. L. Page, and B. Riegel, "ACC/AHA 2007 guidelines for the management of patients with unstable angina/non-ST-elevation myocardial infarction: a report of the American College of Cardiology/American Heart Association," *J Am Coll Cardiol*, vol. 50, no. 7, pp. e1–e157, Aug 2007.

[28] J.-P. Bassand, C. W. Hamm, D. Ardissino, E. Boersma, A. Budaj, F. Fernández-Avilés, K. A. A. Fox, D. Hasdai, E. M. Ohman, L. Wallentin, and W. Wijns, "Guidelines for the diagnosis and treatment of non-ST-segment elevation acute coronary syndromes. task force for diagnosis and treatment of non-ST-segment elevation acute coronary syndromes of European Society of Cardiology," *Eur Heart J*, vol. 28, no. 13, pp. 1598–1660, Jul 2007.

[29] F. V. de Werf, D. Ardissino, A. Betriu, D. V. Cokkinos, E. Falk, K. A. A. Fox, D. Julian, M. Lengyel, F.-J. Neumann, W. Ruzyllo, C. Thygesen, S. R. Underwood, A. Vahanian, F. W. A. Verheugt, and W. Wijns, "Management of acute myocardial infarction in patients presenting with ST-segment elevation. the task force on the management of acute myocardial infarction of the European Society of Cardiology," *Eur Heart J*, vol. 24, no. 1, pp. 28–66, Jan 2003.

[30] I. Graham, D. Atar, K. Borch-Johnsen, G. Boysen, G. Burell, R. Cifkova, J. Dallongeville, G. D. Backer, S. Ebrahim, B. Gjelsvik, C. Herrmann-Lingen, A. Hoes, S. Humphries, M. Knapton, J. Perk, S. G. Priori, K. Pyorala, Z. Reiner, L. Ruilope, S. Sans-Menendez, W. S. op Reimer, P. Weissberg, D. Wood, J. Yarnell, J. L. Zamorano, E. Walma, T. Fitzgerald, M. T. Cooney, and A. Dudina, "European guidelines on cardiovascular disease prevention in clinical practice: executive summary: Fourth joint task force of the european society of cardiology and other societies on cardiovascular disease prevention in clinical practice," *Eur Heart J*, vol. 28, no. 19, pp. 2375–2414, Oct 2007.

[31] L. Mosca, E. J. Benjamin, K. Berra, J. L. Bezanson, R. J. Dolor, D. M. Lloyd-Jones, L. K. Newby, I. L. Piña, V. L. Roger, L. J. Shaw, D. Zhao, T. M. Beckie, C. Bushnell, J. D'Armiento, P. M. Kris-Etherton, J. Fang, T. G. Ganiats, A. S. Gomes, C. R. Gracia, C. K. Haan, E. A. Jackson, D. R. Judelson, E. Kelepouris, C. J. Lavie, A. Moore, N. A. Nussmeier, E. Ofili, S. Oparil, P. Ouyang, V. W. Pinn, K. Sherif, S. C. Smith, G. Sopko, N. Chandra-Strobos, E. M. Urbina, V. Vaccarino, and N. K. Wenger, "Effectiveness-based guidelines for the prevention of cardiovascular disease in women-2011 update a guideline from the American Heart Association," *J Am Coll Cardiol*, vol. 57, no. 12, pp. 1404–1423, Mar 2011.

[32] T. R. Dawber and W. B. Kannel, "The framingham study. an epidemiological approach to coronary heart disease." *Circulation*, vol. 34, no. 4, pp. 553–555, Oct 1966.

[33] P. W. Wilson, R. B. D'Agostino, D. Levy, A. M. Belanger, H. Silbershatz, and W. B. Kannel, "Prediction of coronary heart disease using risk factor categories." *Circulation*, vol. 97, no. 18, pp. 1837–1847, May 1998.

[34] Expert Panel on Detection, Evaluation, and Treatment of High Blood Cholesterol in Adults, "Executive summary of the third report of the national cholesterol education program (NCEP) expert panel on detection, evaluation, and treatment of high blood cholesterol in adults (Adult Treatment Panel III)," *J Am Med Assoc*, vol. 285, pp. 2486–2497, 2001.

[35] R. M. Conroy, K. Pyörälä, A. P. Fitzgerald, S. Sans, A. Menotti, G. D. Backer, D. D. Bacquer, P. Ducimetière, P. Jousilahti, U. Keil, I. Njølstad, R. G. Oganov, T. Thomsen, H. Tunstall-Pedoe, A. Tverdal, H. Wedel, P. Whincup, L. Wilhelmsen, and I. M. Graham, "Estimation of ten-year risk of fatal cardiovascular disease in Europe: the SCORE project." *Eur Heart J*, vol. 24, no. 11, pp. 987–1003, Jun 2003.

[36] P. M. Ridker, J. E. Buring, N. Rifai, and N. R. Cook, "Development and validation of improved algorithms for the assessment of global cardiovascular risk in women: the Reynolds Risk Score," *J Am Med Assoc*, vol. 297, no. 6, pp. 611–619, Feb 2007.

[37] J. Gruettner, T. Henzler, T. Sueselbeck, C. Fink, M. Borggrefe, and T. Walter, "Clinical assessment of chest pain and guidelines for imaging." *Eur J Radiol*, Mar 2011.

[38] B. J. Maron, W. J. McKenna, G. K. Danielson, L. J. Kappenberger, H. J. Kuhn, C. E. Seidman, P. M. Shah, W. H. Spencer, P. Spirito, F. J. T. Cate, and E. D. Wigle, "ACC/ESC clinical expert consensus document on hypertrophic cardiomyopathy. a report of the American College of Cardiology Foundation and the European Society of Cardiology," *Eur Heart J*, vol. 24, no. 21, pp. 1965–1991, Nov 2003.

[39] J. Deanfield, E. Thaulow, C. Warnes, G. Webb, F. Kolbel, A. Hoffman, K. Sorenson, H. Kaemmer, U. Thilen, M. Bink-Boelkens, L. Iserin, L. Daliento, E. Silove, A. Redington, P. Vouhe, S. Priori, M. A. Alonso, J.-J. Blanc, A. Budaj, M. Cowie, J. Deckers, E. F. Burgos, J. Lekakis, B. Lindahl, G. Mazzotta, J. Morais, A. Oto, O. Smiseth, H. J. Trappe, W. Klein, C. Blömstrom-Lundqvist, G. de Backer, J. Hradec, G. Mazzotta, A. Parkhomenko, P. Presbitero, and A. Torbicki, "Management of grown up congenital heart disease," *Eur Heart J*, vol. 24, no. 11, pp. 1035–1084, Jun 2003.

[40] D. P. Zipes, A. J. Camm, M. Borggrefe, A. E. Buxton, B. Chaitman, M. Fromer, G. Gregoratos, G. Klein, A. J. Moss, R. J. Myerburg, S. G. Priori, M. A. Quinones, D. M. Roden, M. J. Silka, C. Tracy, J.-J. Blanc, A. Budaj, V. Dean, J. W. Deckers, C. Despres, K. Dickstein, J. Lekakis, K. McGregor, M. Metra, J. Morais, A. Osterspey, J. L. Tamargo, J. L. Zamorano, S. C. Smith, A. K. Jacobs, C. D. Adams, E. M. Antman, J. L. Anderson, S. A. Hunt, J. L. Halperin, R. Nishimura, J. P. Ornato, R. L. Page, and B. Riegel, "ACC/AHA/ESC 2006 guidelines for management of patients with ventricular arrhythmias and the prevention of sudden cardiac death–executive summary: A report of the American College of Cardiology/American Heart Association in collaboration with the European Heart Rhythm Association and the Heart Rhythm Society," *Eur Heart J*, vol. 27, no. 17, pp. 2099–2140, Sep 2006.

[41] C. Parsai, A. Baltabaeva, L. Anderson, M. Chaparro, B. Bijnens, and G. R. Sutherland, "Low-dose dobutamine stress echo to quantify the degree of remodelling after cardiac resynchronization therapy." *Eur Heart J*, vol. 30, no. 8, pp. 950–958, Apr 2009.

[42] S. Dymarkowski and J. Bogaert, "Heart failure, pulmonary hypertension, and heart transplantation," in *Clinical Cardiac MRI*, ser. Medical Radiology, J. Bogaert, S. Dymarkowski, and A. Taylor, Eds. Springer Berlin Heidelberg, 2005, pp. 271–283.

[43] K. S. Rhode, D. L. G. Hill, P. J. Edwards, J. Hipwell, D. Rueckert, G. Sanchez-Ortiz, S. Hegde, V. Rahunathan, and R. Razavi, "Registration and tracking to integrate X-ray and MR images in an XMR facility," *IEEE Trans Med Imaging*, vol. 22, no. 11, pp. 1369–1378, Nov 2003.

[44] S. G. Duckett, M. R. Ginks, B. R. Knowles, Y. Ma, A. Shetty, J. Bostock, M. Cooklin, J. S. Gill, G. S. Carr-White, R. Razavi, T. Schaeffter, K. S. Rhode, and C. A. Rinaldi, "Advanced image fusion to overlay coronary sinus anatomy with real-time fluoroscopy to facilitate left ventricular lead implantation in CRT," *Pacing Clin Electrophysiol*, vol. 34, no. 2, pp. 226–234, Feb 2011.

[45] M. D. Craene, F. Sukno, C. Tobon-Gomez, C. Butakoff, R. F. i Ventura, C. Hoogendoorn, G. Piella, N. Duchateau, E. Munoz-Moreno, R. Sebastian, O. Camara, and A. Frangi, "Atlas construction and image analysis using statistical cardiac models," in *Statistical Atlases and Computational Models of the Heart (STACOM). MICCAI Workshop*, 2010.

[46] C. Tobon-Gomez, C. Butakoff, S. Aguade, F. M. Sukno, G. Moragas, and A. F. Frangi, "Automatic construction of 3D-ASM intensity models by simulating image acquisition: Application to myocardial gated SPECT studies," *IEEE Trans Med Imaging*, vol. 27, pp. 1655–1667, 2008.

[47] C. Tobon-Gomez, F. M. Sukno, B. H. Bijnens, M. Huguet, and A. F. Frangi, "Realistic simulation of cardiac magnetic resonance studies modeling anatomical variability, trabeculae and papillary Muscles," *Magn Res Med*, vol. 65, pp. 280–288, 2011.

[48] C. Tobon-Gomez, F. M. Sukno, C. Butakoff, M. Huguet, and A. F. Frangi, "Automatic training and reliability estimation for 3D-ASM applied to cardiac mri segmentation," submitted.

[49] C. Butakoff, S. Balocco, S. Ordas, and A. F. Frangi, "Simulated 3D ultrasound LV cardiac images for active shape model training," in *SPIE Medical Imaging 2007: Image Processing*, J.P. Pluim and J.M. Reinhardt, Ed., vol. 6512, 2007, p. 65123U.

[50] R. T. Chin and C. R. Dyer, "Model-based recognition in robot vision," *Comput Surv*, vol. 18, pp. 67–108, 1986.

[51] T. F. Cootes, C. J. Taylor, D. H. Cooper, and J. Graham, "Active Shape Models - their training and application," *Comp Vis Image Underst*, vol. 61, no. 1, pp. 38–59, 1995.

[52] I. L. Dryden and K. Mardia, *Statistical Shape Analysis*. Wiley, 1998.

[53] G. Subsol, J. P. Thirion, and N. Ayache, "A scheme for automatically building three-dimensional morphometric anatomical atlases: application to a skull atlas," *Med Image Anal*, vol. 2, no. 1, pp. 37–60, Mar 1998.

[54] A. D. Brett and C. J. Taylor, "A method of automated landmark generation for automated 3D PDM construction," *Imag Vis Comp*, vol. 18, no. 9, pp. 739 – 748, 2000.

[55] R. H. Davies, C. J. Twining, T. F. Cootes, J. C. Waterton, and C. J. Taylor, "A minimum description length approach to statistical shape modeling," *IEEE Trans Med Imaging*, vol. 21, no. 5, pp. 525–537, May 2002.

[56] A. F. Frangi, D. Rueckert, J. A. Schnabel, and W. J. Niessen, "Automatic construction of multiple-object three-dimensional statistical shape models: application to cardiac modeling," *IEEE Trans Med Imaging*, vol. 21, no. 9, pp. 1151–1166, Sep 2002.

[57] M. R. Kaus, V. Pekar, C. Lorenz, R. Truyen, S. Lobregt, and J. Weese, "Automated 3-D PDM construction from segmented images using deformable models," *IEEE Trans Med Imaging*, vol. 22, no. 8, pp. 1005–1013, Aug 2003.

[58] D. Rueckert, A. F. Frangi, and J. A. Schnabel, "Automatic construction of 3-D statistical deformation models of the brain using nonrigid registration," *IEEE Trans Med Imaging*, vol. 22, no. 8, pp. 1014–1025, Aug 2003.

[59] S. Ordas, E. Oubel, R. Leta, F. Carreras, and A. F. Frangi, "A statistical shape model of the whole heart and its application to model-based segmentation," in *SPIE Medical Imaging: Physiology, function, and structure from medical images*, vol. 6511, 2007, p. 65111K.

[60] C. Lorenz and J. von Berg, "A comprehensive shape model of the heart." *Med Image Anal*, vol. 10, no. 4, pp. 657–670, Aug 2006.

[61] J. Peters, O. Ecabert, C. Meyer, R. Kneser, and J. Weese, "Optimizing boundary detection via simulated search with applications to multi-modal heart segmentation," *Med Image Anal*, vol. 14, no. 1, pp. 70–84, Feb 2010.

[62] H. C. van Assen, M. G. Danilouchkine, M. S. Dirksen, J. H. C. Reiber, and B. P. F. Lelieveldt, "A 3-D active shape model driven by fuzzy inference: application to cardiac CT and MR," *IEEE Trans Inf Technol Biomed*, vol. 12, no. 5, pp. 595–605, Sep 2008.

[63] W. P. Segars, "Development and application of the new dynamic NURBS-based cardiac-torso (NCAT) phantom," Ph.D. dissertation, The University of North Carolina, 2001.

[64] C. Hoogendoorn, F. Sukno, S. Ordas, and A. F. Frangi, "Bilinear models for spatio-temporal point distribution analysis," *International Journal of Computer Vision*, vol. 85, no. 3, pp. 237–252, 2009.

[65] M. Ljungberg and S. E. Strand, "A Monte Carlo program simulating scintillation camera imaging," *Comp Meth Programs Biomed*, vol. 29, pp. 257–272, 1989.

[66] T. K. Lewellen, R. L. Harrison, , and S. Vannoy, "The SimSET program, in monte carlo calculations," in *Monte Carlo Calculations in Nuclear Medicine*, M. Ljungberg, S. Strand, and M. King, Eds. Philadelphia: Institute of Physics Publishing, 1998, pp. 77–92.

[67] OpenGate Collaboration, "Geant4 Application for Emission Tomography (GATE)." [Online]. Available: http://opengatecollaboration.healthgrid.org

[68] W. P. Segars, B. M. W. Tsui, E. C. Frey, and E. K. Fishman, "Extension of the 4D NCAT phantom to dynamic x-ray CT simulation," *Nuclear Science Symposium Conference Record, 2003 IEEE*, vol. 5, pp. 3195–3199, Oct 2003.

[69] K. M. Rosenberg, "The open source computed tomography simulator (CTSim)." [Online]. Available: http://www.ctsim.org

[70] J. A. Jensen, "Field II: A Program for Simulating Ultrasound Systems," 1996. [Online]. Available: http://server.oersted.dtu.dk/personal/jaj/field

[71] H. Benoit-Cattin, G. Collewet, B. Belaroussi, H. Saint-Jalmes, and C. Odet, "The SIMRI project: A versatile and interactive MRI simulator," *J Magn Reson*, vol. 173, pp. 97–115, 2005.

[72] R. K. Kwan, A. C. Evans, and G. B. Pike, "MRI simulation-based evaluation of image-processing and classification methods," *IEEE Trans Med Imaging*, vol. 18, no. 11, pp. 1085–1097, Nov 1999.

[73] W. P. Segars, M. Mahesh, T. J. Beck, E. C. Frey, and B. M. W. Tsui, "Realistic CT simulation using the 4D XCAT phantom," *Med Phys*, vol. 35, no. 8, pp. 3800–3808, Aug 2008.

[74] F. M. Sukno and A. F. Frangi, "Reliability estimation for statistical shape models." *IEEE Trans Imag Proces*, vol. 17, no. 12, pp. 2442–2455, Dec 2008.

[75] A. F. Frangi, W. J. Niessen, and M. A. Viergever, "Three-dimensional modeling for functional analysis of cardiac images: A review," *IEEE Trans Med Imaging*, vol. 20, no. 1, pp. 2–25, 2000.

[76] B. P. F. Lelieveldt, A. F. Frangi, S. C. Mitchell, H. C. van Assen, S. Ordas, J. H. C. Reiber, and M. Sonka, "3D active shape and appearance models in medical image analysis," in *Handbook of Mathematical Models of Computer Vision*, N. Paragios, O. Faugeras, and Y. Chen, Eds. Springer Publishers, 2006, pp. 471–486.

[77] H. C. van Assen, M. G. Danilouchkine, A. F. Frangi, S. Ordas, J. J. M. Westenberg, J. H. C. Reiber, and B. P. F. Lelieveldt, "SPASM: a 3D-ASM for segmentation of sparse and arbitrarily oriented cardiac MRI data," *Med Image Anal*, vol. 10, no. 2, pp. 286–303, Apr 2006.

[78] D. Shen, Y. Zhan, and C. Davatzikos, "Segmentation of prostate boundaries from ultrasound images using statistical shape model," *IEEE Trans Med Imaging*, vol. 4, no. 22, pp. 539–551, Apr. 2003.

[79] G. Germano and D. S. Berman, "Quantitative gated perfusion SPECT," in *Clinical gated cardiac SPECT*. Futura Publishing Co, NY, 1999, pp. 115–146.

[80] G. Germano, H. Kiat, B. Kavanagh, M. Moriel, M. Mazzanti, H. Su, K. F. V. Train, and D. S. Berman, "Automatic quantification of ejection fraction from gated myocardial perfusion SPECT," *J Nucl Med*, vol. 36, p. 2138, Nov 1995.

[81] T. L. Faber, C. Cooke, R. Folks, J. Vansant, K. Nichols, E. DePuey, R. Pettigrew, and E. V. Garcia, "Left ventricular function and perfusion from gated SPECT perfusion images: An intergrated method," *J Nucl Med*, vol. 40, pp. 650–659, 1999.

[82] L. Stegger, C. S. Lipke, P. Kies, B. Nowak, O. Schober, U. Buell, M. Schafers, and W. M. Schaefer, "Quantification of left ventricular volumes and ejection fraction from gated 99mTc-MIBI SPECT: validation of an elastic surface model approach in comparison to cardiac magnetic resonance imaging, 4D-MSPECT and QGS," *Eur J Nucl Med Mol Imaging*, vol. 34, no. 6, pp. 900–909, Jun 2007.

[83] A. D. Achtert, M. A. King, S. T. Dahlberg, P. H. Pretorius, K. J. LaCroix, and B. M. W. Tsui, "An investigation of the estimation of ejection fractions and cardiac volumes by a quantitative gated SPECT software package in simulated gated SPECT images," *J Nucl Cardiol*, vol. 5, no. 2, pp. 144–52, 1998.

[84] E. Vallejo, D. P. Dione, W. L. Bruni, R. T. Constable, P. P. Borek, J. P. Soares, J. G. Carr, S. G. Condos, F. J. T. Wackers, and A. J. Sinusas, "Reproducibility and Accuracy of Gated SPECT for Determination of Left Ventricular Volumes and Ejection Fraction: Experimental Validation Using MRI," *J Nucl Med*, vol. 41, pp. 874–882, 2000.

[85] J. Montagnat and H. Delingette, "4D deformable models with temporal constraints: application to 4D cardiac image segmentation," *Med Image Anal*, no. 9, pp. 87–100, 2005.

[86] D. Lingrand, A. Charnoz, P. M. Koulibaly, J. Darcourt, and J. Montagnat, "Toward accurate segmentation of the LV myocardium and chamber for volumes estimation in gated SPECT sequences," in *Eur Conf Comp Vision*, ser. Lect Notes Comp Science, vol. 3024, 2004, pp. 267–278.

[87] M. D. Cerqueira, N. J. Weissman, V. Dilsizian, A. K. Jacobs, S. Kaul, W. K. Laskey, D. J. Pennell, J. A. Rumberger, T. Ryan, and M. S. Verani, "Standardized myocardial segmentation and nomenclature for tomographic imaging of the heart: a statement for healthcare professionals from the cardiac imaging committee of the council on clinical cardiology of the american heart association," *Circulation*, vol. 105, no. 4, pp. 539–542, 2002.

[88] X. He, E. C. Frey, J. M. Links, K. L. Gilland, W. P. Segars, and B. M. W. Tsui, "A mathematical observer study for the evaluation and optimization of compensation methods for myocardial SPECT using a phantom population that realistically models patient variability," *IEEE Trans Nucl Sci*, vol. 51, no. 1, pp. 218–224, Feb 2004.

[89] A. B. Barclay, R. L. Eisner, and E. DiBella, "Emory PET thorax model database," http://www.emory.edu/CRL/abb/thoraxmodel/contents.html, Tech. Rep., 1995.

[90] A. K. Jain, R. P. W. Duin, and J. Mao, "Statistical pattern recognition: A review," *IEEE Trans Pattern Anal Machine Intell*, vol. 22, no. 1, pp. 4–37, 2000.

[91] K. J. LaCroix, B. M. W. Tsui, E. C. Frey, and R. J. Jaszczak, "Receiver operating characteristic evaluation of iterative reconstruction with attenuation correction in 99mTc-Sestamibi myocardial SPECT images," *J Nucl Med*, vol. 41, pp. 502–513, 2000.

[92] J. C. Gower, "Generalized procrustes analysis," *Psychometrika*, vol. 40, pp. 33–50, 1975.

[93] M. Ljungberg, A. Larsson, and L. Johansson, "A new collimator simulation in SIMIND based on the delta-scattering technique," *IEEE Trans Nucl Sci*, vol. 52, no. 5, pp. 1370–1375, Oct 2005.

[94] J. A. Fessler, "Users guide for ASPIRE 3D image reconstruction software," Comm. and Sign. Proc. Lab., Dept. of EECS, Univ. of Michigan, Ann Arbor, MI, Tech. Rep. 310, Jul 1997.

[95] C. Butakoff and A. F. Frangi, "A framework for weighted fusion of multiple statistical models of shape and appearance," *IEEE Trans Pattern Anal Machine Intell*, vol. 28, no. 11, pp. 1847–1857, Nov 2006.

[96] C. Tobon-Gomez, C. Butakoff, S. Ordas, S. Aguade, and A. F. Frangi, "Comparative study of diversely trained 3D-ASM models for segmentation of gated SPECT data," in *SPIE Medical Imaging: Physiology, function, and structure from medical images*, A. Manduca and X.P. Hu, Ed., vol. 6511, 2007, p. 65112G.

[97] J. D. Gibbons, *Nonparametric Statistical Inference*, 2nd ed. Marcel Dekker, Inc, 1985.

[98] C. Vanhove, P. R. Franken, M. Defrise, A. Momen, H. Everaert, and A. Bossuyt, "Automatic determination of left ventricular ejection fraction from gated blood-pool tomography," *J Nucl Med*, vol. 42, pp. 401–407, 2001.

[99] J. Bland and D. Altman, "Statistical methods for assessing agreement between two methods of clinical measurement," *Lancet*, vol. 8476, pp. 307–10, Feb 1986.

[100] J. Bogaert, "Cardiac function," in *Clinical Cardiac MRI*, J. Bogaert, S. Dymarkowski and A.M. Taylor, Ed., vol. 1. Springer-Verlag New York, Inc, 2005, pp. 99–134.

[101] E. Tadamura, T. Kudoh, M. Motooka, M. Inubushi, T. Okada, S. Kubo, N. Hattori, T. Matsuda, T. Koshiji, K. Nishimura, M. Komeda, and J. Konishi, "Use of technetium-99m sestamibi ECG-gated single-photon emission tomography for the evaluation of left ventricular function following coronary artery bypass graft: comparison with threedimensional magnetic resonance imaging," *Eur J Nucl Meds*, vol. 26, pp. 705–712, 1999.

[102] C. D. L. Bavelaar-Croon, H. W. M. Kayser, E. E. van der Wall, A. de Roos, P. Dibbets-Schneider, E. K. J. Pauwels, G. Germano, and D. E. Atsma, "Left ventricular function: Correlation of quantitative gated SPECT and MR imaging over a wide range of values," *Radiology*, vol. 217, pp. 572–575, 2000.

[103] K. Nakajima, T. Higuchi, J. Taki, M. Kawano, and N. Tonami, "Accuracy of ventricular volume and ejection fraction measured by gated myocardial SPECT: comparison of 4 software programs," *J Nucl Med*, vol. 42, pp. 1571–1578, 2001.

[104] C. S. A. Lipke, H. P. Kuhl, B. Nowak, H. J. Kaiser, P. Reinartz, K. C. Koch, U. Buell, and W. M. Schaefer, "Validation of 4D-MSPECT and QGS for quantification of left ventricular volumes and ejection fraction from gated 99mTc-MIBI SPET: comparison with cardiac magnetic resonance imaging," *Eur J Nucl Med Mol Imaging*, vol. 31, no. 4, pp. 482–490, 2004.

[105] M. Lomsky, J. Richter, L. Johansson, H. El-Ali, K. Astrom, M. Ljungberg, and L. Edenbrandt, "A new automated method for analysis of gated SPECT images based on a three-dimensional heart shaped model," *Clin Physiol Funct Imaging*, vol. 25, no. 4, pp. 234–240, 2005.

[106] W. M. Schaefer, C. S. A. Lipke, D. Standke, H. P. Kuhl, B. Nowak, H. J. Kaiser, K. C. Koch, and U. Buell, "Quantification of left ventricular volumes and ejection fraction from gated 99mTc-MIBI SPECT: MRI validation and comparison of the emory cardiac tool box with QGS and 4D-MSPECT," *J Nucl Med*, vol. 46, pp. 1256–1263, 2005.

[107] Y. W. Wu, E. Tadamura, M. Yamamuro, S. Kanao, S. Okayama, N. Ozasa, M. Toma, T. Kimura, M. Komeda, and K. Togashi, "Estimation of global and regional cardaic function usgin 64-slice computed tomography: A comprasion study with echocardiography, gated-SPECT and cardiovascular magnetic resonance," *Int J Cardiol*, vol. Epub ahead of print, no. 2, Aug 2007.

[108] J. P. A. Ioannidis, T. A. Trikalinos, and P. G. Danias, "Electrocardiogram-gated single-photonemission computed tomography versus cardiacmagnetic resonance imaging for the assessmentof left ventricular volumes and ejection fraction: A meta-analysis," *J Am Coll Cardiol*, vol. 39, no. 12, pp. 2059–2068, Jun 2002.

[109] J. A. Case, S. J. Cullom, T. M. Bateman, C. Bamhart, and M. J. Saunders, "Overestimation of LVEF by gated MIBI myocardial perfusion SPECT in patients with small hearts," *J Am Coll Cardiol*, vol. 31, no. Supplement 1, pp. 43–43, 1998.

[110] A. K. Attili, A. Schuster, E. Nagel, J. H. C. Reiber, and R. J. van der Geest, "Quantification in cardiac mri: advances in image acquisition and processing." *Int J Cardiovasc Imaging*, vol. 26 Suppl 1, pp. 27–40, Feb 2010.

[111] J. Jensen and N. Svendsen, "Calculation of pressure fields from arbitrarily shaped, apodized, and excited ultrasound transducers," *IEEE Trans Ultrason Ferroelectr Freq Control*, vol. 39, no. 2, pp. 262–267, Mar 1992.

[112] B. Aubert-Broche, A. C. Evans, and L. Collins, "A new improved version of the realistic digital brain phantom," *Neuroimage*, vol. 32, no. 1, pp. 138–145, Aug 2006.

[113] D. J. Anderson, J. M. Dendy, and C. B. Paschal, "Simulation study of susceptibility gradients leading to focal myocardial signal loss," *J Magn Reson Imaging*, vol. 28, no. 6, pp. 1402–1408, 2008.

[114] R. Haddad, I. E. Magnin, and P. Clarysse, "A new fully-digital anthropomorphic and dynamic thorax/heart model," *29th Annual International Conference of the IEEE Engineering in Medicine and Biology Society*, pp. 5999–6002, Aug 2007.

[115] P. Ferreira, P. Gatehouse, P. Kellman, C. Bucciarelli-Ducci, and D. Firmin, "Variability of myocardial perfusion dark rim gibbs artifacts due to sub-pixel shifts," *J Cardiovasc Magn Res*, vol. 11, no. 1, p. 17, 2009.

[116] A. I. Veress, W. P. Segars, J. A. Weiss, B. M. W. Tsui, and G. T. Gullberg, "Normal and pathological ncat image and phantom data based on physiologically realistic left ventricle finite-element models." *IEEE Trans Med Imaging*, vol. 25, no. 12, pp. 1604–1616, Dec 2006.

[117] F. Bloch, "Nuclear induction," *Phys Rev*, vol. 70, no. 7-8, pp. 460–474, Oct 1946.

[118] The Visible Human Project ®. National Library of Medicine. [Online]. Available: http://www.nlm.nih.gov/research/visible/visible_human.html

[119] C. J. Salton, M. L. Chuang, C. J. O'Donnell, M. J. Kupka, M. G. Larson, K. V. Kissinger, R. R. Edelman, D. Levy, and W. J. Manning, "Gender differences and normal left ventricular anatomy in an adult population free of hypertension: A cardiovascular magnetic resonance study of the framingham heart study offspring cohort," *J Am Coll Cardiol*, vol. 39, no. 6, pp. 1055–1060, Mar 2002.

[120] L. H. Ling, J. K. Oh, C. Tei, R. L. Click, J. F. Breen, J. B. Seward, and A. J. Tajik, "Pericardial thickness measured with transesophageal echocardiography: feasibility and potential clinical usefulness," *J Am Coll Cardiol*, vol. 29, no. 6, pp. 1317–1323, May 1997.

[121] P. A. Bottomley, T. H. Foster, R. E. Argersinger, and L. M. Pfeifer, "A review of normal tissue hydrogen NMR relaxation times and relaxation mechanisms from 1-100 MHz: dependence on tissue type, nmr frequency, temperature, species, excision, and age," *Med Phys*, vol. 11, no. 4, pp. 425–448, 1984.

[122] D. R. Messroghli, S. Plein, D. M. Higgins, K. Walters, T. R. Jones, J. P. Ridgway, and M. U. Sivananthan, "Human myocardium: single-breath-hold MR T1 mapping with high spatial resolution–reproducibility study," *Radiology*, vol. 238, no. 3, pp. 1004–1012, Mar 2006.

[123] C. M. Wacker, M. Bock, A. W. Hartlep, G. Beck, G. van Kaick, G. Ertl, W. R. Bauer, and L. R. Schad, "Changes in myocardial oxygenation and perfusion under pharmacological stress with dipyridamole: Assessment using T1 and T2* measurements," *Magn Res Med*, vol. 41, pp. 686–695, 1999.

[124] D. Li, Y. Wang, and D. J. Waight, "Blood oxygen saturation assessment in vivo using T2* estimation," *Magn Res Med*, vol. 39, no. 5, pp. 685–690, May 1998.

[125] S. F. Akber, "An association between spin-lattice relaxation time and organ weight in humans," *Med Hypotheses*, vol. 48, no. 2, pp. 189–191, Feb 1997.

[126] A. Stadler, P. M. Jakob, M. Griswold, M. Barth, and A. A. Bankier, "T1 mapping of the entire lung parenchyma: Influence of the respiratory phase in healthy individuals," *J Cardiovasc Magn Res*, vol. 21, no. 6, pp. 759–764, Jun 2005.

[127] T. Y. Huang, Y. J. Liu, A. Stemmer, and B. P. Poncelet, "T2 measurement of the human myocardium using a T2-prepared transient-state TrueFISP sequence," *Magn Res Med*, vol. 57, no. 5, pp. 960–966, May 2007.

[128] G. A. Wright, B. S. Hu, and A. Macovski, "Estimating oxygen saturation of blood in vivo with mr imaging at 1.5 T," *J Magn Reson Imaging*, vol. 1, no. 3, pp. 275–283, 1991.

[129] M. Westwood, L. J. Anderson, D. N. Firmin, P. D. Gatehouse, C. C. Charrier, B. Wonke, and D. J. Pennell, "A single breath-hold multiecho T2* cardiovascular magnetic resonance technique for diagnosis of myocardial iron overload," *J Magn Reson Imaging*, vol. 18, no. 1, pp. 33–39, Jul 2003.

[130] C. M. J. de Bazelaire, G. D. Duhamel, N. M. Rofsky, and D. C. Alsop, "MR imaging relaxation times of abdominal and pelvic tissues measured in vivo at 3.0 T: preliminary results," *Radiology*, vol. 230, no. 3, pp. 652–659, Mar 2004.

[131] G. Brix, L. R. Schad, and W. J. Lorenz, "Evaluation of proton density by magnetic resonance imaging: phantom experiments and analysis of multiple component proton transverse relaxation," *Phys Med Biol*, vol. 35, no. 1, pp. 53–66, Jan 1990.

[132] W. P. Segars, S. Mendonca, G. Sturgeon, and B. M. W. Tsui, "Enhanced 4d heart model based on high resolution dual source gated cardiac ct images," in *IEEE Nuclear Science Symposium Conference Record NSS '07*, vol. 4, Oct. 26 2007–Nov. 3 2007, pp. 2617–2620.

[133] S. Goo, P. Joshi, G. Sands, D. Gerneke, A. Taberner, Q. Dollie, I. LeGrice, and D. Loiselle, "Trabeculae carneae as models of the ventricular walls: implications for the delivery of oxygen." *J Gen Physiol*, vol. 134, no. 4, pp. 339–350, Oct 2009.

[134] M.-L. Ward, A. J. Pope, D. S. Loiselle, and M. B. Cannell, "Reduced contraction strength with increased intracellular [ca2+] in left ventricular trabeculae from failing rat hearts." *J Physiol*, vol. 546, no. Pt 2, pp. 537–550, Jan 2003.

[135] B. R. Wilcox, A. C. Cook, and R. H. Anderson, *Surgical Anatomy of the Heart*, 3rd ed.   Cambridge University Press, 2004, ch. Anatomy of the cardiac chambers, pp. 11–44.

[136] L. G. Nyúl, J. K. Udupa, and X. Zhang, "New variants of a method of mri scale standardization," *IEEE Trans Med Imaging*, vol. 19, no. 2, pp. 143–150, Feb 2000.

[137] R. Brunelli and O. Mich, "Histograms analysis for image retrieval," *Pattern Recognit*, vol. 34, no. 8, pp. 1625–1637, August 2001.

[138] S. Kullback and R. A. Leibler, "On information and sufficiency," *Ann. Math. Statistics*, vol. 22, pp. 79–86, 1951.

[139] T. Heimann and H.-P. Meinzer, "Statistical shape models for 3D medical image segmentation: a review," *Med Image Anal*, vol. 13, no. 4, pp. 543–563, Aug 2009.

[140] A. F. Frangi, W. J. Niessen, and M. A. Viergever, "Three-dimensional modeling for functional analysis of cardiac images: a review." *IEEE Trans Med Imaging*, vol. 20, no. 1, pp. 2–25, Jan 2001.

[141] A. A. Young and A. F. Frangi, "Computational cardiac atlases: from patient to population and back." *Exp Physiol*, vol. 94, no. 5, pp. 578–596, May 2009.

[142] H. Zhang, A. Wahle, R. K. Johnson, T. D. Scholz, and M. Sonka, "4-D cardiac MR image analysis: left and right ventricular morphology and function," *IEEE Trans Med Imaging*, vol. 29, no. 2, pp. 350–364, Feb 2010.

[143] X. Zhuang, K. S. Rhode, R. S. Razavi, D. J. Hawkes, and S. Ourselin, "A registration-based propagation framework for automatic whole heart segmentation of cardiac MRI," *IEEE Trans Med Imaging*, vol. 29, no. 9, pp. 1612–1625, Sep 2010.

[144] J. M. P. Lötjönen, V. M. Järvinen, B. Cheong, E. Wu, S. Kivistö, J. R. Koikkalainen, J. J. O. Mattila, H. M. Kervinen, R. Muthupillai, F. H. Sheehan, and K. Lauerma, "Evaluation of cardiac biventricular segmentation from multiaxis MRI data: a multicenter study," *J Magn Reson Imaging*, vol. 28, no. 3, pp. 626–636, Sep 2008.

[145] P. Radau, Y. Lu, K. Connelly, G. Paul, A. J. Dick, and G. A. Wright, "Evaluation framework for algorithms segmenting short axis cardiac MRI," *The MIDAS Journal -*, vol. MICCAI Workshops -, p. Cardiac MR Left Ventricle Segmentation Challenge, 2009.

[146] Z. Zhang, "Iterative point matching for registration of free-form curves and surfaces," *Int J Comput Vision*, vol. 13, pp. 119–152, 1994.

[147] GIMIAS v1.1.0, "Center for Computational Image and Simulation Technologies in Biomedicine, Universitat Pompeu Fabra," http://www.gimias.org, 2010. [Online]. Available: http://www.gimias.org

[148] T. F. Cootes, C. J. Taylor, and A. Lanitis, "Multi-resolution search with active shape models," in *Proc. 12th Int. Conf. Pattern Recognition*, vol. 1, 1994, pp. 610 –612.

[149] M. Ma, M. van Stralen, J. H. C. Reiber, J. G. Bosch, and B. P. F. Lelieveldt, "Model driven quantification of left ventricular function from sparse single-beat 3D echocardiography," *Med Image Anal*, vol. 14, no. 4, pp. 582–593, Aug 2010.

[150] J. S. Wijnhout, D. Hendriksen, H. C. van Assen, and R. J. van der Geest, "LV challenge LKEB contribution: Fully automated myocardial contour detection," *The MIDAS Journal -*, vol. MICCAI 2009 Workshops -, p. Cardiac MR Left Ventricle Segmentation Challenge.

[151] J. R. Koikkalainen, T. Tölli, K. Lauerma, K. Antila, E. Mattila, M. Lilja, and J. M. P. Lötjönen, "Methods of artificial enlargement of the training set for statistical shape models," *IEEE Trans Med Imaging*, vol. 27, no. 11, pp. 1643–1654, Nov 2008.
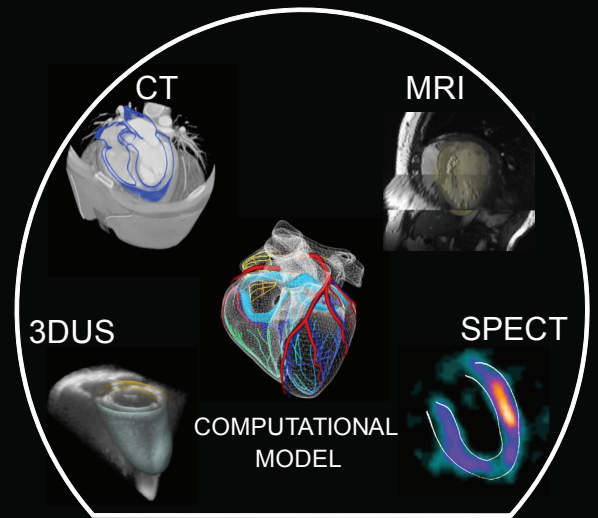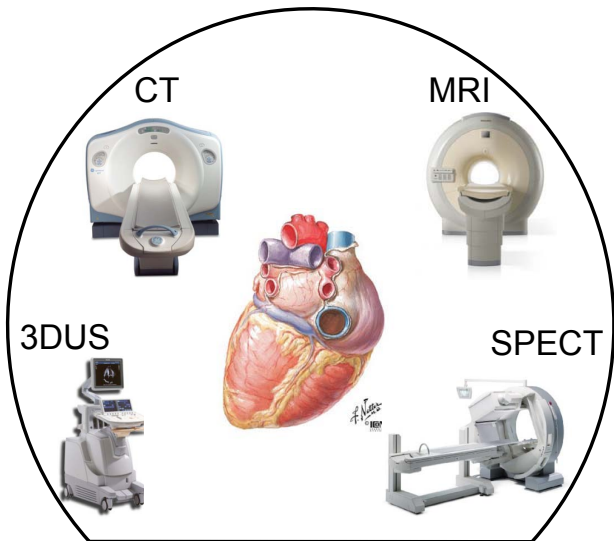
CT MRI
3DUS SPECT

In a clinical environment the multimodal scheme is observed naturally. The clinician in charge will mentally combine all the information to diagnose the patient.

3DUS= Three-dimensional ultrasound; CT= Computed Tomography; MRI= Magnetic Resonance Imaging; SPECT= Single Photon Emission Computed Tomography (p. 12).


CT MRI
3DUS SPECT
COMPUTATIONAL MODEL

Active Shape Models are a robust and accurate approach to quantify cardiac parameters from multimodal image data. They can evaluate the spatio-temporal variabilityof the heart.

3DUS= Three-dimensional ultrasound; CT= Computed Tomography; MRI= Magnetic Resonance Imaging; SPECT= Single Photon Emission Computed Tomography (p. 13).

Shape Model
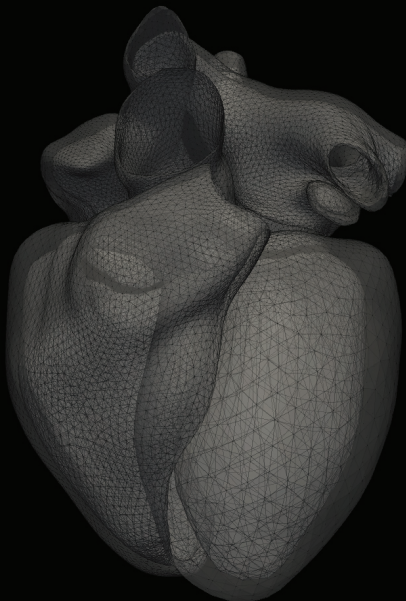
Intensity Model
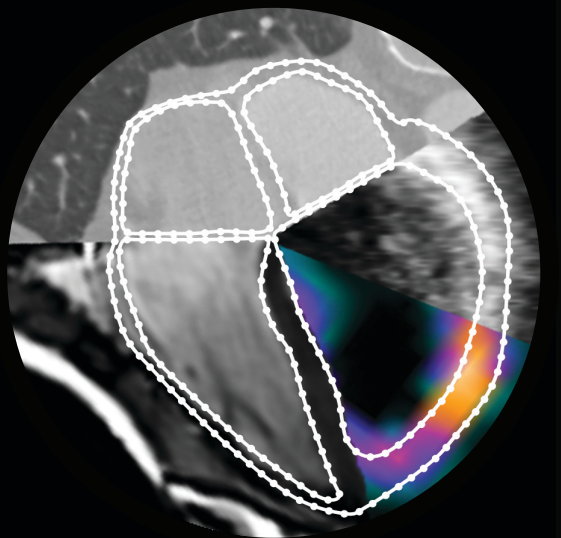
We use a 3D shape model built from CT datasets. The shape information is complemented with intensity information specific to each modality by simulating the physics of acquisition (p. 21).
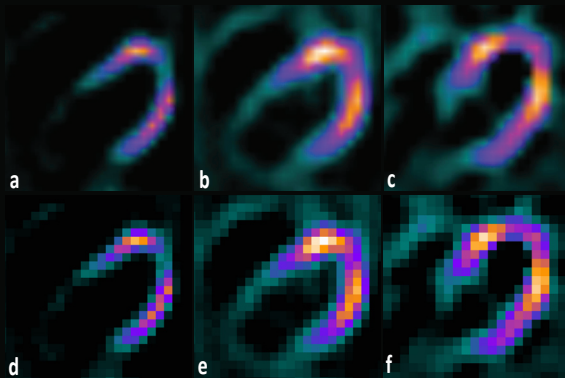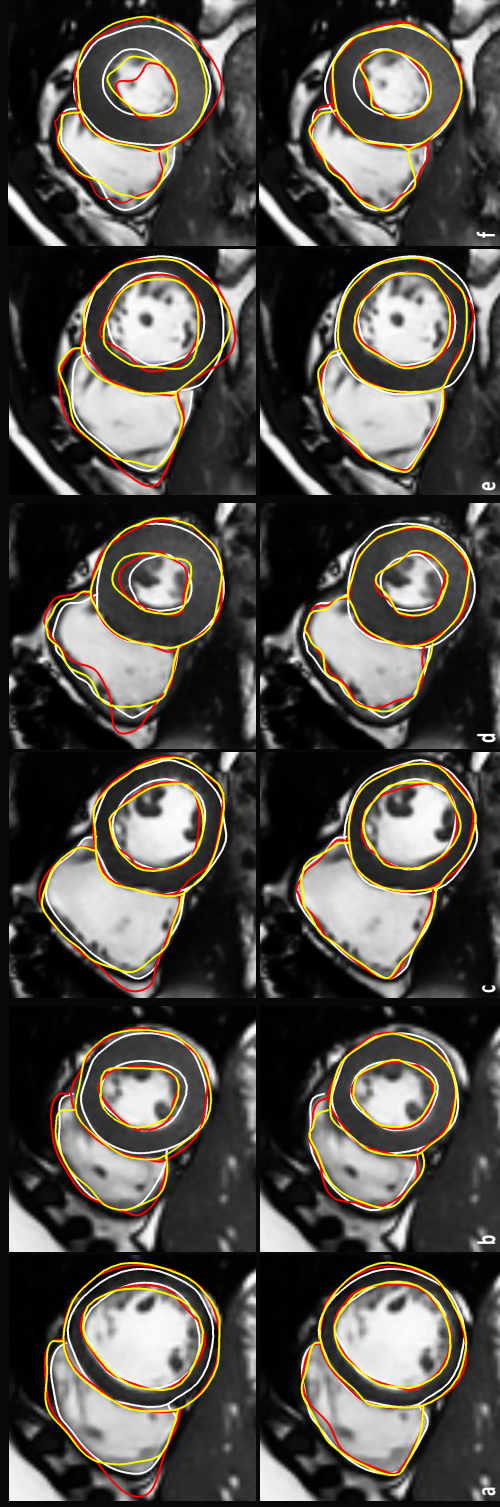
Interpolated (top) and original (bottom) axial views of a virtual (a-b, d-e) and a clinical (c,f) gSPECT study. They were reconstructed by means of OSEM (a,d) and FBP (b-c, e-f). FBP= Filtered Back-projection; OSEM= Ordered-subset Expectation Maximization (p. 28).
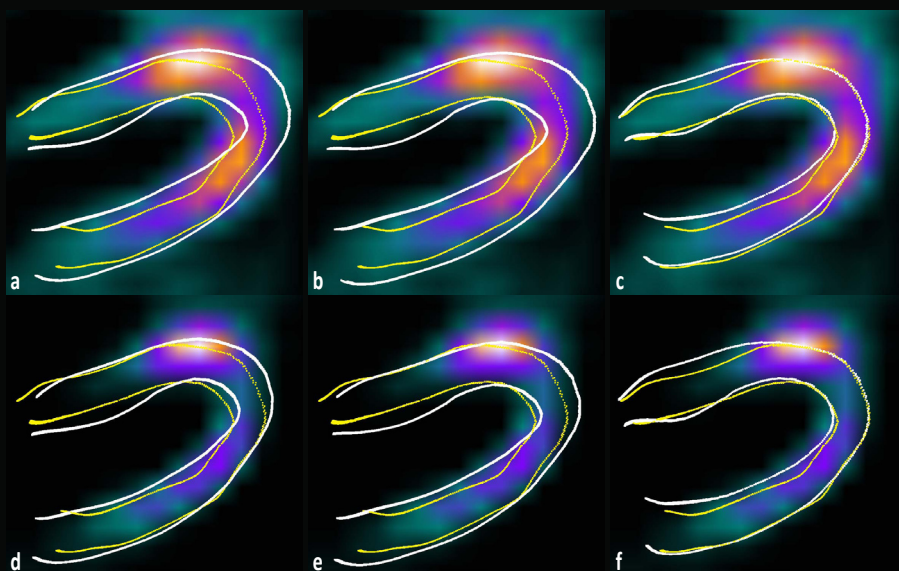

Axial view of a virtual study for FBP (a-c) and OSEM (d-f) reconstructed images. Edges obtained automatically by 3D-ASM with ST (a,d), GR (b,e), FBP (c) and OSEM (f) boundary models are shown in white. True edges are displayed on yellow. ST= step function; GR= maximum gradient; FBP= Filtered Back-projection; OSEM= Ordered-subset Expectation Maximization (p. 34).
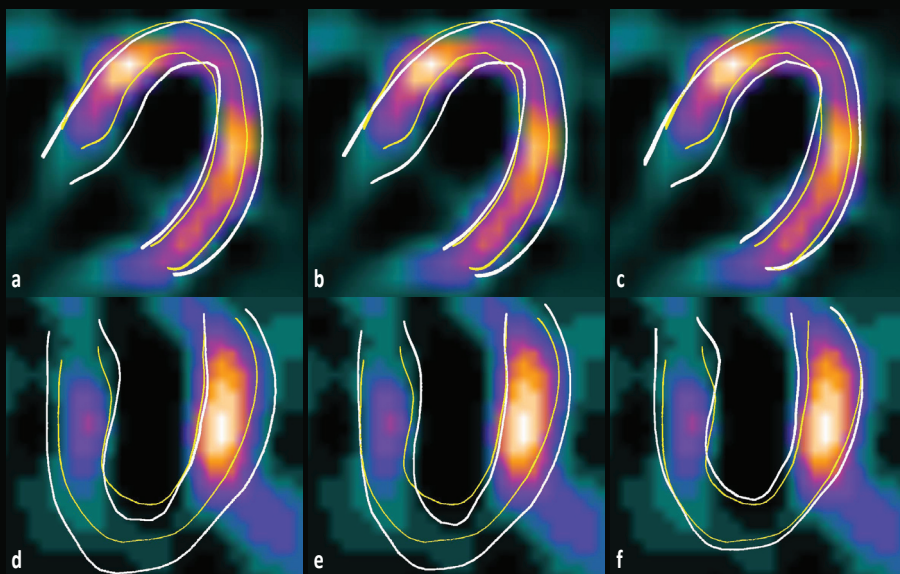

Two clinical cases with severe perfusion defects: case one in axial view (a-c) and case two in long-axis view (d-f). Edges obtained automatically by 3D-ASM with ST (a,d), GR (b,e) and FBP (c,f) boundary models are shown in white (thick). True edges are displayed on yellow (thin). Abbreviations as in figure above (p. 34).

Images from clinical group C1: a normal subject (a-b), a hypertrophic patient(c-d), and an infacted patient (e-f). Edges obtained automatically by 3D-ASM with simulated (top) and real (bottom) intensity models at end diastole (a,c,e) and end systole (b,d,f). Note the influence of reliability information for the simulated models (top), specially for the right ventricle. White= ground-truth surface; Red= matched surface with no reliability; Yellow= matched surface with reliability (p. 73).
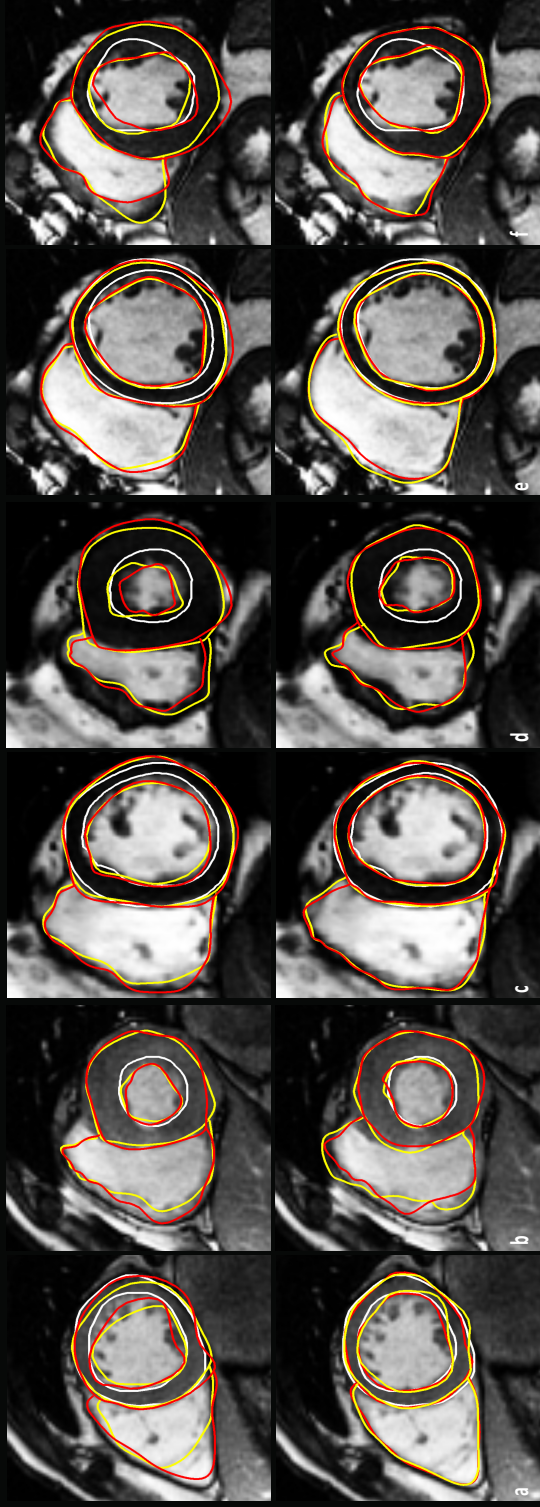
Images from clinical group C2: a normal subject (a-b), a hypertrophic patient(c-d), and a heart failure patient (e-f). Edges obtained automatically by 3D-ASM with simulated (top) and real (bottom) intensity models at end diastole (a,c,e) and end systole (b,d,f). Note the influence of reliability information for the simulated models (top), specially for the left ventricular epicardium. White= ground-truth surface; Red= matched surface with no reliability; Yellow= matched surface with reliability (p. 74).
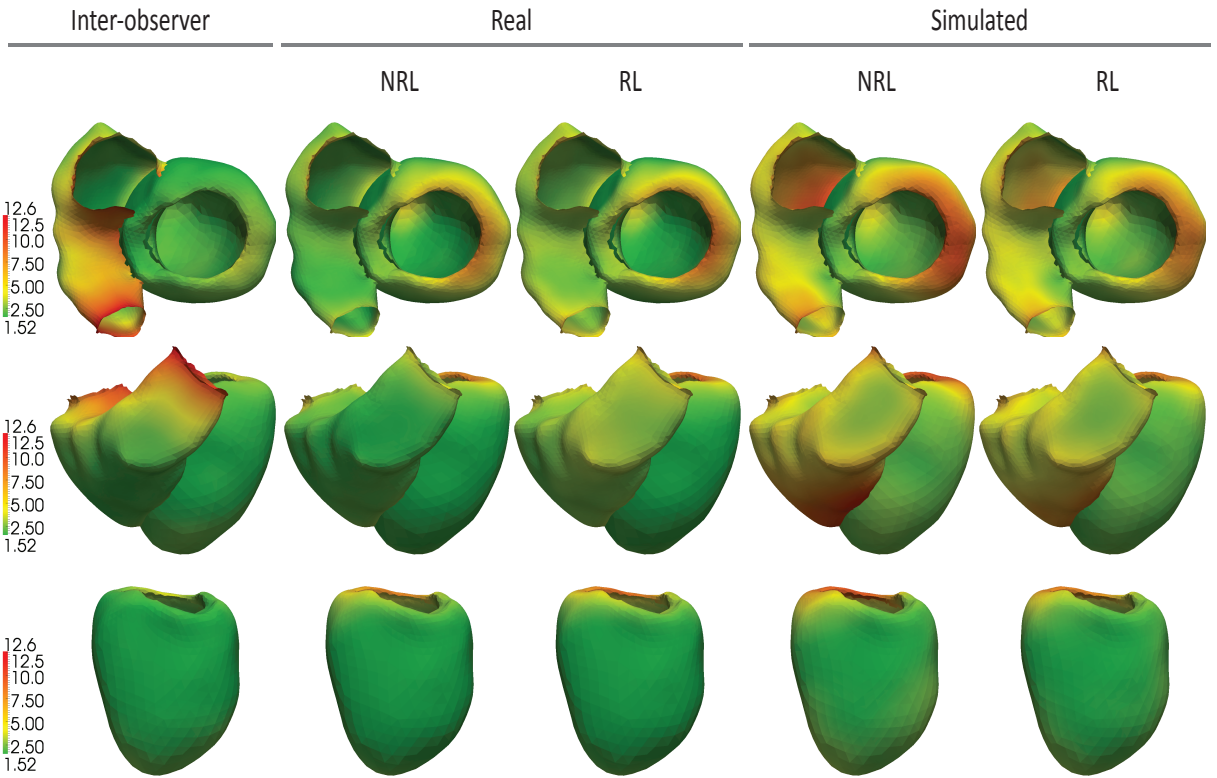
Average segmentation errors for group C1 (end diastole and end systole). Color-map displayed on the mean shape model with data range from inter-observer values in mm (a). Note the reduction of large errors at the LV base and RV free wall for simulated intensity models with reliability information (d-e). Top view (top), front view (mid) and septal view (bottom). NRL= No reliability; RL= reliability (p. 77).
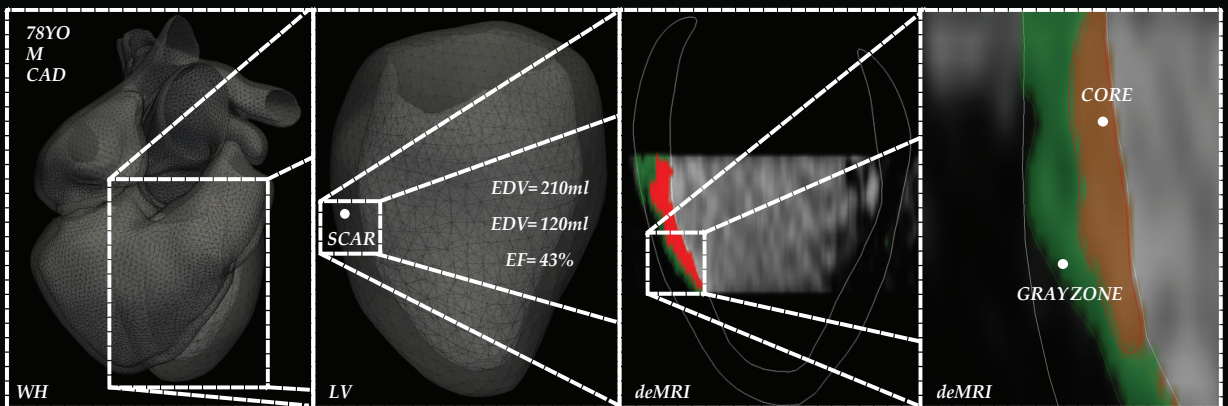

Illustration of a multilevel computational model: the anatomical geometry is complemented with functional information at different levels. WH= Whole heart; LV= Left Ventricle; EDV= End diastolic volume; ESV= End systolic volume; EF= Ejection fraction; deMRI= Delayed enhancement Magnetic Resonance Imaging; Core= Infarct core; Gray Zone= Area peripheral to the core (p. 90).